Diesel Engine Tribology

PhD Thesis

$$(EIv'')'' = q - \rho A \ddot{v}$$

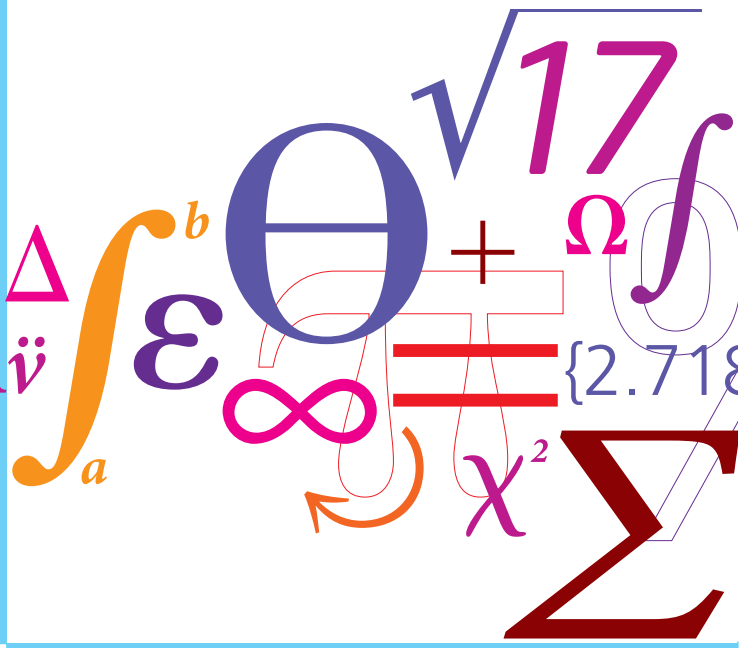

Christian Kim Christiansen
DCAMM Special Report No. S193
December, 2015

DTU Mechanical Engineering
Department of Mechanical Engineering

Diesel Engine Tribology

Christian Kim Christiansen

Kgs. Lyngby 2015
DCAMM Special Report No. S193

Diesel Engine Tribology
December, 2015 (revised March, 2016)

PhD student:
Christian Kim Christiansen

Main supervisor:
Professor Peder Klit
Technical University of Denmark

Co-supervisors:
Professor Jens Honore Walther
Technical University of Denmark

Senior researcher Anders Vølund
MAN Diesel & Turbo SE

© 2015 Christian Kim Christiansen

Technical University of Denmark
Department of Mechanical Engineering
Building 404, DK-2800 Kgs. Lyngby, Denmark
Phone: +45 45 25 25 25, Fax: +45 45 25 19 61
E-mail: info@mek.dtu.dk, URL: www.mek.dtu.dk

ISBN 978-87-7475-439-8
DCAMM Special Report No. S193, ISSN 0903-1685

Abstract

Recent years have seen an increase in the wear rate of engine bearings, subsequently followed by bearing failure, for the large two-stroke diesel engines used for ship propulsion. Here, the engine bearings include main, big end and crosshead bearings, with the bearing type used being the journal bearing, belonging to the class of 'hydrodynamic bearings'. This implies that the load carrying capacity is generated by a relative movement of the involved components, i.e. a velocity-driven operation. For the engine application, the velocity stems from the engine RPM. However, to comply with the latest emission requirements as well as attempting to minimise fuel expenses, the engine speed has been lowered together with an increase in the engine mean pressure which in terms lead to larger bearing loads.

With worsened operating conditions from two sides, the encountered problems are understandable as the design criteria for the bearings are no longer valid, albeit still not desirable. To come up with a solution, the operating conditions of the bearings have to be understood. The main challenge is to supply sufficient with lubricant to avoid metal-metal contact under time-varying combustion load. This project has therefore revolved around the investigation of the tribological performance of the dynamically loaded journal bearing, both theoretically and experimentally.

The theoretical work covers two approaches to the modelling of the bearing; a traditional finite element based solver for Reynolds equation, and a more general finite volume discretisation of the Navier-Stokes equations. In this way the influence from assumptions usually made in regards to supply grooves can be verified.

A test rig has been constructed for replicating engine-like conditions. An uni-directional load can be applied in both static and dynamic modes, while another key feature being that of a transparent polymer bearing enabling the study of film rupture and re-forming.

Paper [P1] describes the development of a suitable finite volume mesh for

dynamic loading, while Paper [P2] contains the perturbation implementation used for the dynamic loading. Resorting to Gümbel boundary conditions, very similar orbits are predicted for a given bearing using the two methods as demonstrated in Paper [P3]. Good agreement is also obtained between the numerical and experimental results.

Finally, some suggestions to improvements of the modelling as well as the experimental set-up, are made.

Keywords Journal bearing · Finite element · Finite volume · Experimental work · Cavitation

Resumé

I de senere år har man oplevet en stigning i raten, hvorved motorlejer slides, efterfulgt af nedbrud, i de store to-takts dieselmotorer der benyttes i skibe. Her menes motorlejer at omfatte hoved-, plejlstangs- og krydshovedlejer, som alle er af typen glideleje, en del af kategorien 'hydrodynamiske lejer'. Dette indebærer, at lejets bæreevne genereres ved en relativ forskydning af de involverede komponenter, m.a.o. en hastighedsdrevet drift. Ved anvendelse i forbrændingsmotorer stammer hastigheden fra motorens omdrejninger. For at opfylde de nyeste emissionsstandarder og samtidig mindske udgifterne til brændstof, er motorernes omdrejningshastighed imidlertid sænket samtidig med at middeltrykket er øget, noget som igen øger belastningen på lejerne.

Med forværrede driftsbetingelser fra to sider, er de opståede problemer forventelige, eftersom at lejernes designkriterier ikke længere er gyldige, men stadig ikke ønskelige. For at kunne fremsætte en løsning på problemet, er det nødvendigt at forstå lejernes driftsbetingelser. Den største udfordring er at kunne levere tilstrækkeligt med smøremiddel, til at undgå metal-metalkontakt under en forbrændingslast der varierer i tiden. Dette projekt har derfor udviklet sig omkring undersøgelse af den tribologiske ydeevne af et dynamisk belastet glideleje, både teoretisk og eksperimentelt.

Det teoretiske arbejde omfatter to tilgange til modellering af lejet; en traditionel finite element-baseret løsning af Reynolds ligning og en mere generel finite volume-diskretisering af Navier-Stokes ligninger. På denne måde kan indflydelsen fra antagelser typisk gjort i forbindelse med forsyningsnoter verificeres. En testrig er konstrueret til at kunne efterligne motor-lignende forhold. En en-akset belastning kan påtrykkes i både statisk og dynamisk form, mens en anden nøgleegenskab er et transparent polymerleje der muliggør visuelle studier af filmbrud og –gendannelse.

Artikel [P1] beskriver udviklingen af et egnet finite volume-net for dynamisk belastning, mens Artikel [P2] indeholder implementeringen af perturbationsmetoden for dynamisk belastning. Med Gümbel randbetingelser er meget ens

baneforløb beregnet for et givent leje, som demonstreret i Artikel [P3]. God overensstemmelse er også opnået i mellem de numeriske og eksperimentelle resultater.

Slutteligt er nogle forslag til forbedringer, af såvel modellering som det eksperimentelle set-up, fremsat.

Nøgleord Glideleje · Finite element · Finite volume · Eksperimentelt arbejde · Kavitation

Preface

First of all my thanks go to my team of supervisors: Peder Klit, Jens Walther and Anders Vølund. Of course, I would like to thank my office mates Jonas Lauridsen, Shravan Janakiraman, Jorge González and Fabián Pierart. I have really appreciated our conversations on a variety of topics. Also very much worth a mentioning, are fellow PhD students Alejandro Cerda, Jon Larsen and Christopher Nellemann for our professional as well as social discussions plus the invaluable discussion of mathematics with Joe Alexandersen and Rasmus Christiansen. They all have a share in the project. The rest of the FAM section also deserves a mentioning for a pleasant atmosphere and good colleagues.

A number of students have also had influence on the project, during their thesis work on the test rig. Per Jensen & Emil Joensen, Jesper Kristoffersen, Jákup Olsen, Anders Jørgensen-Juul & Kristian Kristensen, Gustavo Ruiz, and Anders Vive & Suzan Kurt all contributed to the final set-up. Lastly, but definitely not least, Anders Vive and Niels Steenfeldt have been tremendous in their efforts for improving the test results.

My external stay went to Luleå University of Technology in Northern Sweden, and I will have to thank Professor Roland Larsson and Associate professor Andreas Almqvist for having me there. Also, I am thankful to Jessica & Jens Hardell for their hospitality.

Finally, I should mention my nearest family for bearing with me, when I have been focused on nothing but journal bearings.

Kgs. Lyngby, December 2015

Christian Kim Christiansen

List of papers

The below papers, written during the project, form part of the thesis. The listing is based on submission date.

[P1] **Christian K. Christiansen**, Peder Klit, Jens H. Walther, and Anders Vølund. "Application of finite elements and computational fluid dynamics to predict and improve the filling ratio in journal bearings under dynamic loading". In: *Proceedings of NSCM-27: the 27th Nordic Seminar on Computational Mechanics*. (Stockholm). Ed. by A. Eriksson, A. Kulachenko, M. Mihaescu, and G. Tibert. TRITA-MEK Technical report. ISSN: 0348-467X. 2014, pp. 50–53.

[P2] **C. K. Christiansen**, P. Klit, J. H. Walther, and A. Vølund. "Cavitation Estimates by Orbit Prediction of a Journal Bearing - Finite Element Modelling and Experimental Studies". In: *TRIBOLOGIA - Finnish Journal of Tribology 1* 33.1 (2015), pp. 28–35. ISSN: 0780-2285.

[P3] **Christian Kim Christiansen**, Jens Honore Walther, Peder Klit, and Anders Vølund. "Investigation of journal orbit and flow pattern in a dynamically loaded journal bearing". Intended for publishing in Tribology International. Mar. 2016. Draft.

Contents

Abstract **i**

Resumé **iii**

Preface **v**

List of papers **vii**

Nomenclature **xiii**

1 Introduction **1**
1.1 Project 1
1.1.1 Motivation 1
1.2 Literature study 3
1.2.1 Cavitation 4
1.2.2 Numerical analysis 6
1.2.3 Experimental analysis 6
1.3 Project focus areas 6
1.4 Thesis outline 7

2 The journal bearing **9**
2.1 Bearing geometry 10

3 Reynolds equation **13**
3.1 Derivation 13
3.1.1 Velocity-pressure relation 14
3.1.2 Mass conservation 15
3.1.3 The full Reynolds equation 16
3.1.4 The usual form of Reynolds equation 16
3.2 Non-dimensionalisation 17
3.2.1 External mass flow 19

4 Analytical solutions to Reynolds eq. 21
4.1 General expressions . . . 21
4.1.1 Load carrying capacity . . . 22
4.1.2 Attitude angle . . . 22
4.1.3 Sommerfeld number . . . 22
4.1.4 Losses . . . 23
4.1.5 Oil consumption . . . 24
4.2 Long Bearing Theory . . . 24
4.2.1 Half bearing solution . . . 28
4.3 Narrow Bearing Theory . . . 28
4.4 Locus curves . . . 30

5 Journal orbit calculations 33
5.1 Spring-damper system . . . 33
5.2 The perturbation method . . . 34
5.3 Shaft position iterations . . . 36

6 Finite element implementation 39
6.1 Static version . . . 39
6.1.1 Flowchart . . . 44
6.1.2 Example solutions . . . 44
6.2 Dynamic version . . . 47
6.2.1 Functionals . . . 47
6.2.2 Finite element equations . . . 48
6.2.3 Flowchart . . . 49
6.2.4 Example solutions . . . 51

7 Finite volume implementation 55
7.1 Governing equations . . . 55
7.2 Meshing . . . 56
7.3 Dynamic fluid body interaction formulation . . . 57
7.3.1 Morphing . . . 57
7.3.2 Ramping . . . 58
7.4 Time stepping . . . 58
7.5 Example solution . . . 58

8 Cavitation test rig 61
8.1 Test rig overview . . . 61
8.1.1 Data acquisition . . . 62
8.1.2 Load control . . . 63
8.2 Test rig design . . . 63
8.2.1 Design considerations . . . 63

8.3 Experimental setup 69

9 Numerical results **73**
9.1 Solution set-up 74
9.1.1 Solutions 76

10 Experimental results **89**
10.1 Journal orbit 89
10.1.1 Clearance measurements 89
10.1.2 Static loading 91
10.1.3 Dynamic loading 91
10.2 Cavitation patterns 100

11 Conclusions **105**
11.1 Future work 106

Appendices **107**

A The Sommerfeld substitution **109**
A.1 Expressions for θ and ψ 110
A.2 Integrals 111

B Green-Gauss extensions **113**

C Nodal and element numbering **115**

D Functional derivation **117**
D.1 Functional for $\bar{p}_0$ 118
D.2 Functional for $\bar{p}_1$ 119
D.3 Functional for $\bar{p}_2$ 120
D.4 Functional for $\bar{p}_3$ 121
D.5 Functional for $\bar{p}_4$ 122

E Technical drawings of polymer bearings for CTR **123**

F Locus curve additionals **129**

Publications **131**

1 Application of FE and CFD to journal bearings **133**

2 Cavitation estimates of a JB - FE and experiments **139**

3 Investigation of a dynamically loaded journal bearing **149**

References **171**
General references 171
Papers forming part of the thesis 175

Nomenclature

Variables

μ	Dynamic viscosity	$\mathrm{Pa} \cdot \mathrm{s}$
ν	Angular viscosity (Chapters 3,5,6)	rad/s
ν	Kinematic viscosity (Chapter 2)	m^2/s
ω	Angular velocity	rad/s
ψ	Substitution angle	rad
ρ	Density	kg/m^3
τ	Shear stress	Pa
θ	Angular coordinate, starting from maximum film thickness	rad
θ'	Angular coordinate (global)	rad
ε	Eccentricity ratio	–
φ	Attitude angle	rad
ζ	Non-dimensional coordinate, axial direction	–
C	Clearance (radial)	m
D	Diameter	m
e	Eccentricity	m
F	Load carrying capacity	N
f	Non-dimensional load carrying capacity	–
h	Film thickness	m

L	Length	m
M	Torque	Nm
m	Mass flow per unit width	$\mathrm{kg}/(\mathrm{s}\cdot\mathrm{m})$
m'	Mass flow per unit area	$\mathrm{kg}/(\mathrm{s}\cdot\mathrm{m}^2)$
N	Revolutions	1/s
p	Film pressure	Pa
Q	Oil consumption	m^3/s
q	Volume flow per unit width	m^2/s
R	Radius	m
t	Time	s
U	Velocity x direction	m/s
W	Imposed load (except Chapter 3)	N
W	Velocity z direction (Chapter 3)	m/s
x, y, z	Film coordinates	m

Sub- and superscripts

$()_1$	Lower surface, typically bushing
$()_2$	Upper surface, typically journal
$()_b$	Bushing
$()_j$	Journal
$()_l$	Load
$\bar{()}$	Non-dimensional parameter –
$\hat{()}$	Dimensional scaling parameter
$\mathbf{K}$	Matrix, except load vectors, e.g. $\mathbf{W}$ of Equation (6.27)
$\mathbf{u}$	Vector

$\tilde{()}$	Approximated parameter	
f	Friction	
h	Housing	
j	Journal	
r	Radial component	
t	Tangential component	

Non-dimensional numbers

Re	Reynolds number	–
S	Sommerfeld number	–

Abbreviations

CAD	Crank Angle Degree
CTR	Cavitation Test Rig
FE	Finite Element
FV	Finite Volume

Chapter 1

Introduction

1.1 Project

This PhD project is a part of the EU project HERCULES-C[1] in the years 2012-2014. The HERCULES-C name is an abbreviation for the third phase of a research programme entitled Higher Efficiency, Reduced Emissions, Increased Reliability and Lifetime, Engines for Ships. Division into relevant areas, positions the PhD project in work package 10.3 entitled "Low friction engine bearings".

The work conducted during the studies has been carried out at the Department of Mechanical Engineering - Technical University of Denmark, with the support of MAN Diesel & Turbo SE in Copenhagen, Denmark.

1.1.1 Motivation

As in most combustion engines, journal bearings are also used in the engines manufactured by MAN Diesel, due to their good load carrying capacity relative to the size and cost. The typical applications are those of main bearing and in the two ends of the connecting rod: big end and cross-head bearings, i.e. load transferring components. In other words, those are vital components mounted centrally within the engine, see Figure 1.1. With the central position of those bearings, reliability is a key issue, as the remainder of the ship is built around the engine leading to month-long stays in docks, in case of repairs.

The journal bearing belongs to the class of hydrodynamic bearings, which means its load carrying capacity is generated by relative motion, here that of the journal rotating relative to the surrounding bushing.

[1] `http://www.hercules-c.com/` (grant agreement no. SCP1-GA-2011-284354)

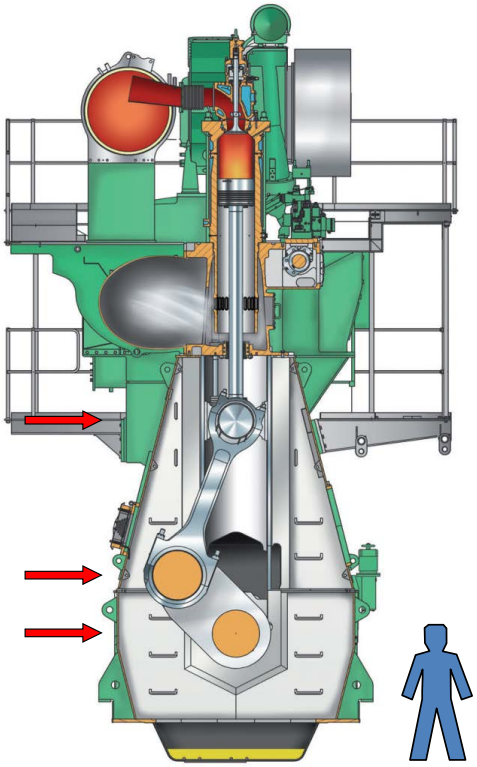

Figure 1.1: Illustration of MAN Diesel & Turbo S50ME-B engine with indication of journal bearing locations. Notice pictogram of human for size reference. Illustration is adapted from [1].

In today's society, the ship owner is faced with two external factors: emission legislations and fuel costs. During the last decades the advent of law packages and standard like MARPOL Annex VI and Tier 1-4 have aimed at limiting the marine pollution. The solution from the engine manufacturers' side have been an increase in engine pressure to increase the efficiency, but also the load on the bearing. With no gearbox between engine and propeller, the obvious answer to the fuel saving question is by lowering the engine RPM.

The engine bearings is now met with factors worsening the operational condition: increased load and lowered relative velocity. Existing bearing designs are naturally not designed for the new operational scenario, so to avoid damages like those of Figure 1.2(a), improved designs are required. With only one engine, engine failure can be fatal, as the propulsion is needed for controlling the vessel.

(a) (b)

Figure 1.2: The small film thickness enables unfolding of the oil film, hence reducing the three dimensional problem to two dimensions. (a) Example of bearing damage, taken from [2]. (b) Worst case scenario for engine failure, taken from [3].

If the worst imaginable happens, Figure 1.2(b) demonstrates the outcome.

The motivation for this project is to improve the understanding of the conditions under which the bearing operates and apply this knowledge in the design of a bearing with reduced friction, but with a similar or increased load carrying capacity. This is trivial for a statically loaded bearing, as supply grooves for lubricants can be optimised for one load condition. For a bearing operating under engine-like condition, i.e. under dynamic loading and a possible variable rotational speed, it is far from trivial.

1.2 Literature study

With Reynolds describing the fundamental principles of hydrodynamic lubrication in his paper of 1886 [4], the area has been well-defined for more than 100 years. Hence, also the amount of publications on the topic is wast, especially with its application in the prominent sectors of transport and energy. Limiting the scope to the combustion related processes, the literature is still available in large numbers.

With background in some of the classical review papers in the field, e.g. Dowson and Taylor, 1979 [5] and Braun and Hannon, 2010 [6], there are three major areas, which are also partly mirrored in the structure of the thesis, to be considered for the journal bearing: Cavitation forming, numerical analysis and experimental analysis.

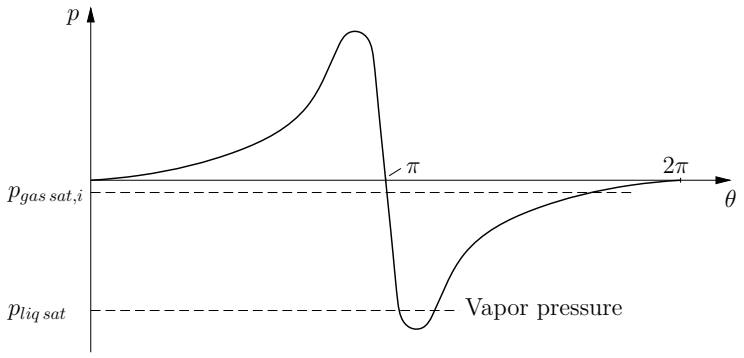

Figure 1.3: Journal bearing pressure distribution incl. threshold values. Inspired from Braun and Hannon [6].

1.2.1 Cavitation

In the above mentioned paper [4] Reynolds defined the equation that was later going to be coined Reynolds equation, see Equation (1.1). Despite limitations to the eccentricity range for which Reynolds could solve the equation, it was evident that the solution is an anti-symmetric pressure profile, see Figure 1.3.

$$\frac{\partial}{\partial x}\left(\frac{h^3}{12\mu}\frac{\partial p}{\partial x}\right)+\frac{\partial}{\partial z}\left(\frac{h^3}{12\mu}\frac{\partial p}{\partial z}\right)=\frac{U_1+U_2}{2}\frac{\partial h}{\partial x}+\frac{\mathrm{d}}{\mathrm{d}t}h \tag{1.1}$$

For larger loads the anti-symmetry will demand first sub-atmospheric pressures and ultimately negative pressures. Both contradict the observation that fluids generally speaking cannot withstand tension. Several people have later investigated this phenomenon, e.g. Floberg, 1973 [7].

The simplest approach put forward, were just to neglect the negative half of the solution and putting $p(\pi \leq \theta \leq 2\pi) = 0$. This has become known as the half-Sommerfeld or Gümbel solution.

From stability and continuity considerations, respectively, Swift and Stieber came to the same considerations in the 1930's, namely that for a statically loaded bearing [8, 9]:

$$\frac{\mathrm{d}p}{\mathrm{d}x}=\frac{\mathrm{d}p}{\mathrm{d}z}=0, \quad p=p_{cav} \tag{1.2}$$

Derived from the principles of conservation, this approach inherits mass conservation, contrary to the Gümbel solution. This is not the case, however, across the lubricant/gas boundaries bound to exist qua the flow separation caused by the sub-atmospheric pressures that were proved experimentally by Floberg in a

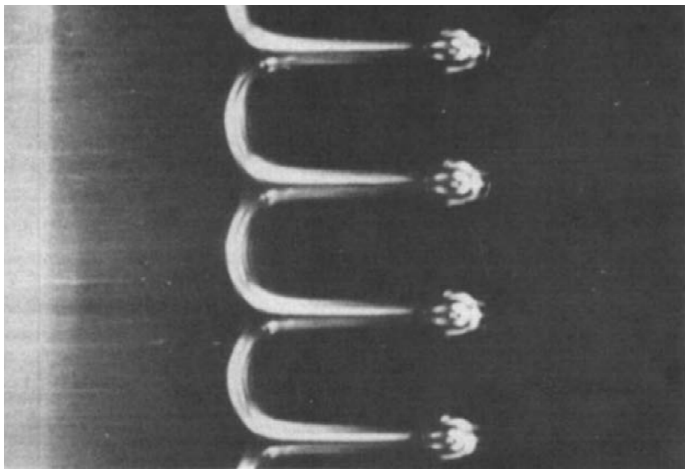

Figure 1.4: Illustration of cavitation striations with lubricant to the left and gas to the right. The journal rotation is from left to right. Illustration is adapted from [5].

number of papers up to 1973. A series of independent contributions respectively done by Jakobsson, Floberg and Olsson during 1957–1974, were made towards what today is known as the JFO cavitation theory [7, 10–12]. To this day, this theory is considered as the most correct way of modelling the cavitation problem involving Reynolds equation.

Examples of the occurrence of the film rupture and subsequent reformation, as described above, are multiple in the literature, with Figure 1.4 representing a typical example of cavitation for a statically loaded journal. Here so-called striations, or tongues, are formed upon the separation of gas and fluid (lubricant).

Lubricants are known to contain considerable volume fractions of air at atmospheric conditions [6, 13], with the latter giving 9% as a number. This amount is the potential for release, if the pressure drops below the saturation pressure of the gas as indicated by the upper dashed line of Figure 1.3.

Consequences of cavitation

The predominant motive for the immense interest in cavitation is reduction in pressure seen in Figure 1.3. Replacing the load carrying lubricant regions with a lubricant/gas mixture severely increases the possibility of bearing damage due to contact between journal and housing, especially during a dynamic load situation. The absent of a stable fluid lubricant region can also inflict bearing instabilities. As Jakobsson and Floberg points out, the reduction is not only

negative, as the gas pockets obviously have lower viscosity leading to reduced friction losses [10].

1.2.2 Numerical analysis

From the above outline, the JFO theory seems to be of all importance to the plausible modelling of the journal bearing. The complexity of the formulation made the JFO theory difficult to program until Elrod and Adams in 1974 suggested a weighting function for describing the cavitated/non-cavitated areas [14]. Quite a number of derived and/or improved schemes have evolved from the original Elrod algorithm today, covering both finite element and finite volume discretisations. The weighting function applied are seen as the Achilles heel of the algorithms, as is typically relates to the bulk modulus and hence be difficult to assess and also be a very large number leading to numerical instabilities.

With the advent of modern computing power, Navier-Stokes equations (NSE) based programs have been of interest. Solving the full set of equations for 3D instead of the 2D assumptions contained in Reynolds equation, obviously include the possibility to model geometries not properly resolved using a 2D approach. Typically commercial codes are employed, with the benefit of having already verified cavitation schemes incorporated. Due to the computer requirements, this branch has only appeared around year 2000 as indicated by [15–17].

1.2.3 Experimental analysis

Studying the literature, it is clear that experimental equipment and their results have been given almost as much attention as the theoretical investigations. The test rigs develop from analogue in the first papers and reflecting the changes in time, such that entering computer age in the 1980's, the test rigs followed suit. This also correlates with the type of experiments. Reynolds carried out the fundamental experiments as part of his work in 1886 [4], whereas the increased, but still analogue, data logging enabled studies of the orbit of a dynamically loaded journal bearing around 1960 by Shawki and Freeman and Carl[18, 19]. Finally, some decades later high-speed camera recordings of the cavitation process were made possible [20].

1.3 Project focus areas

Based on the previous section, numerous works have been published on the fields of numerical and experimental investigation of dynamically loaded journal bearings. Especially the theoretical/numerical cavitation formulation has received a lot of attention (prime example being that of the Elrod algorithm and its multiple derivatives). On the other hand, the full Rayleigh bubble growth

models are readily available in the commercial CFD packages, but the reported use is still very scarce. On the experimental part, the published works are decades old, particularly those on visual monitoring of cavitation.

The contributions of this project will therefore be two-fold. Partly, the application of a modern, commercial CFD package to the cavitation problem and, partly development and implementation of a cavitation test rig enabling validation of the numerical findings as well as studying cavitation formation.

1.4 Thesis outline

The thesis is structured such that Chapter 2 contains the basic of the journal bearing, Chapters 3-5 deals with the theoretical background concerning the formulation of the governing equations and the analytical solutions to those, Chapters 6 and 7 is devoted to the numerical solution methods applied, Chapter 8 describe the experimental set-up and results, being numerical and experimental are given in Chapters 9 and 10. Chapter 11 concludes the thesis, by summarising the findings.

The appended papers cover most of the above areas, such that Paper [P1] documents the experiences from the application of a commercial software package to the journal bearing geometry, Paper [P2] verifies the numerical solution to a classic benchmark case and Paper [P3] compares the code of Paper [P2] with the commercial code of Paper [P1], but applied to the developed, experimental set-up.

Chapter 2

The journal bearing

The journal bearing is the most simple bearing type. As it consists only of a shaft and a housing (or bush) as depicted in Figure 2.1 applications dates back to the earliest structures containing rotating components such as water mills and various wagons. Hence the components are only separated by the lubricant film as indicated with yellow in the figure.

Today the journal bearing is still widely used, mainly due to a high load carrying capacity. Applications ranges from small wagons and carts to turbines and combustion engines. The bearing type is the most prevailing as main bearing in combustion engines, for instance. Advantages are the high load carrying capacity and small requirements to build-in space, whereas the capability of only supporting radial loads are the main disadvantage.

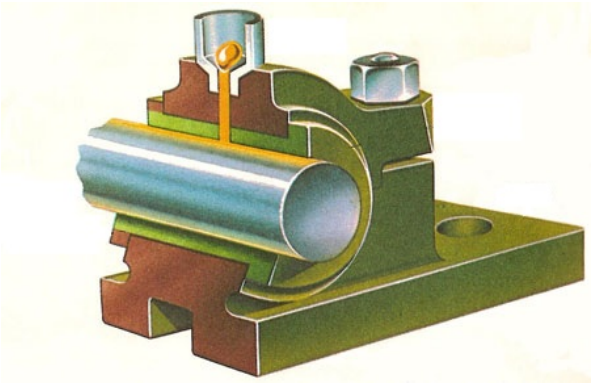

Figure 2.1: Schematic of journal bearing. Adapted from Darling [21].

2.1 Bearing geometry

As described above the bearing is a very simple set-up consisting of the rotating shaft and stationary housing. The bore of the housing is the diameter of the shaft, D, plus two times a radial clearance C. In other words are $C \ll D$, typically $C = 1/1000D$. From Figure 2.2 one obtains the film thickness in the bearing as:

$$h(\theta) = C(1 + \varepsilon \cos\theta) \quad , \quad \varepsilon = e/C \tag{2.1}$$

The scalar ε is termed the eccentricity ratio and can take values of $\varepsilon = [0, 1]$. Generally speaking a heavily loaded bearing will exhibit a large value of ε (~ 0.9) and a lightly loaded bearing yields almost no eccentricity. Thus the film thickness will always be $0 < h(\theta) < 2C$.

From the vertical load applied in Figure 2.2 the corresponding displacement of the shaft center might be expected to have the same (vertical) direction. Due to the hydrodynamic forces, however, the center is shifted an angle φ. This phenomenon will be described in a more throughout manner in Chapter 4.

Summing up, the behaviour of the journal bearing can be described completely by three parameters related to the design of the bearing and three operational parameters. These parameters are listed in Table 2.1. Especially the length /diameter ratio L/D is a widespread characterisation of a journal bearing. For calculations, the fact that the clearance is much smaller than the length and circumference of the bearing, is exploited. Thus the cylindrical coordinate system

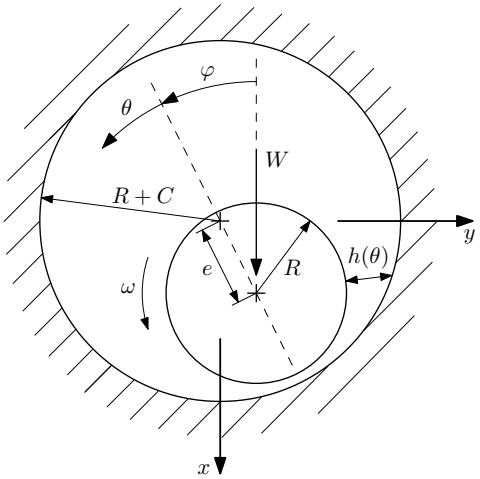

Figure 2.2: Nomenclature of journal bearing. The z axis is pointing out of the plane.

Table 2.1: Dimensional and operational parameters for the journal bearing. Typical values for a 100 mm bearing are listed.

Parameter	Value	Unit
Length, L	80[a]	mm
Diameter, D	100	mm
Clearance, C (radial)	50	µm
Rotational speed, N	1500	RPM
Load, W	10	kN
Dynamic viscosity, μ	0.08	Pa · s

[a] The L/D ratio lies usually in the interval 0.1–3.

of Figure 2.3(a) can be unfolded, resulting in the plane problem of Figure 2.3(b). This is the frame of reference for the next chapters unless otherwise is stated.

Reynolds number

The Reynolds number for journal bearings may be defined as:

$$Re = \frac{LU}{\nu} = \frac{C\omega R\rho}{\mu} \tag{2.2}$$

The first expression is the general form with some characteristic length scale L. Using the clearance as the length scale reveals the laminar nature of the flow. With the data of Table 2.1 and a density $\rho = 850\,\mathrm{kg/m^3}$, $Re \sim 4$.

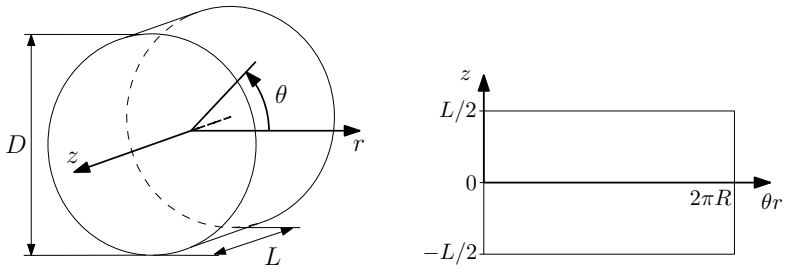

(a) Bearing with coordinate system. (b) Unfolded geometry.

Figure 2.3: The small film thickness enables unfolding of the oil film, hence reducing the three dimensional problem to two dimensions. (a) Orientation of the cylindrical coordinate system exploiting the symmetry. (b) Unfolded bearing geometry.

Chapter 3

Reynolds equation

The today well-known concept of hydrodynamic lubrication was first formulated by Osborne Reynolds in his classic paper of 1886 [4].

3.1 Derivation

Based on a set of assumptions listed below Reynolds equation can be derived from the Navier-Stokes equation, dimensional analysis or as in this case by a more practically oriented way, considering an infinitely small fluid element. This method is commonly used in the literature, e.g. [22–24].

In either case a set of general assumptions has to be applied:

1. Laminar flow, i.e. $Re <\sim 2000$.
2. Newtonian fluid, i.e. $\tau = \mu \partial U / \partial y$ and no slip conditions at the bearing-lubricant interface.
3. Oil film is thin, i.e. $h \ll x, z$, leads to:
   a) Plane geometry (equivalent to plane stress of solid mechanics). In other words are shear stresses and velocity gradients only of importance through the film (y direction).
   b) Constant viscosity through film thickness.
   c) Neglecting body forces e.g. gravity (mass less) or magnetic fields.
   d) Constant pressure through film.
4. Neglecting inertia forces. Assumption 1 guarantees that the viscous forces are much larger than the inertia forces.

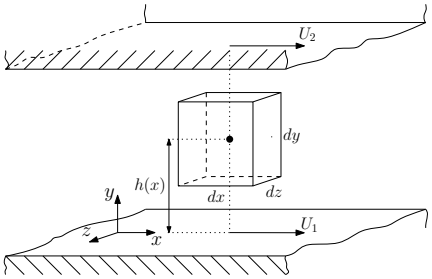

(a) Fluid element with coordinate system.

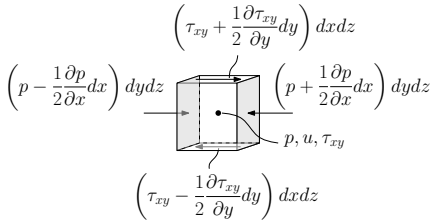

(b) Fluid element with centroid and forces acting in x direction.

Figure 3.1: (a) An infinitesimal fluid element between two surfaces. (b) Free body diagram for 1D case. Adapted from McIvor [23].

3.1.1 Velocity-pressure relation

Consider the infinitesimal fluid element shown in Figure 3.1. The forces in Figure 3.1(b) occur due to assumptions 1, 3a, 3c and 4. With the application of a force equilibrium for the x direction one obtains:

$$\begin{aligned}\sum F_x = &\left(p-\frac{1}{2}\frac{\partial p}{\partial x}dx\right)dydz-\left(p+\frac{1}{2}\frac{\partial p}{\partial x}dx\right)dydz\\ &+\left(\tau_{xy}+\frac{1}{2}\frac{\partial \tau_{xy}}{\partial y}dy\right)dxdz-\left(\tau_{xy}-\frac{1}{2}\frac{\partial \tau_{xy}}{\partial y}dy\right)dxdz=0\end{aligned} \tag{3.1}$$

$$\Downarrow$$

$$\frac{\partial \tau_{xy}}{\partial y}=\frac{\partial p}{\partial x} \tag{3.2}$$

Utilising assumption 2, the proportionality between shear stress and velocity gradient transform Equation (3.2) into a relationship between pressure and velocity:

$$\frac{\partial}{\partial y}\left(\mu\frac{\partial u}{\partial y}\right)=\frac{\partial p}{\partial x} \tag{3.3}$$

Solving for u by integration of Equation (3.3) wrt. y is straight forward:

$$u=\frac{1}{2\mu}\frac{\partial p}{\partial x}y^2+C_1y+C_2 \tag{3.4}$$

The integration constants are readily found from the boundary conditions (see Figure 3.1(a)), $y=0, u=U_1$ and $y=h, u=U_2$, such that:

$$u=\frac{1}{2\mu}\frac{\partial p}{\partial x}\left(y^2-yh\right)+\frac{U_2-U_1}{h}y+U_1 \tag{3.5}$$

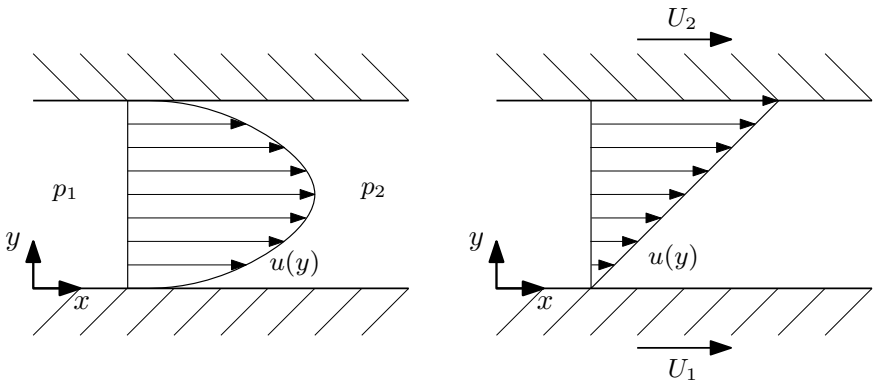

$p_1 > p_2$ (a) Poiseuille term.

$U_1 \neq U_2$ (b) Couette term.

Figure 3.2: (a) The parabolic Poiseuille term driven by a pressure difference. (b) The linear Couette term driven by a velocity difference.

Equations (3.1)-(3.5) do also exist in versions for the z direction:

$$\frac{\partial \tau_{zy}}{\partial y} = \frac{\partial p}{\partial z} \quad \Rightarrow \quad w = \frac{1}{2\mu}\frac{\partial p}{\partial z}\left(y^2 - yh\right) + \frac{W_2 - W_1}{h}y + W_1 \tag{3.6}$$

It can be noted that the velocities u and w both consist of a parabolic Poiseuille term (pressure driven) and a linear Couette term (velocity driven), see Figure 3.2.

3.1.2 Mass conservation

The fluid element of Figure 3.1(a) is part of a column, see Figure 3.3(a) and with the corresponding mass flows per unit width outlined in Figure 3.3(b). The procedure is analogue to the equilibrium of Figure 3.1 and Equation (3.1). As a check it can be seen that the balance of the in- and outgoing flows yields the 2D continuity equation:

$$\frac{\partial m_x}{\partial x} + \frac{\partial m_z}{\partial z} + \frac{\mathrm{d}}{\mathrm{d}t}\rho h = 0 \tag{3.7}$$

Exploiting the definition of mass flow as density times the product of velocity and cross sectional area, one obtains (per unit width):

$$m_x = \rho q_x = \rho \int_0^h u \,\mathrm{d}y \tag{3.8}$$

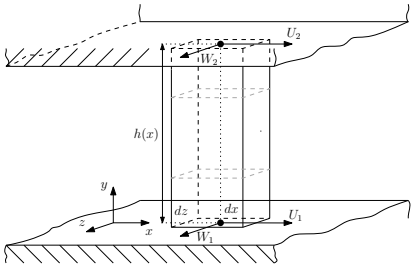

(a) Fluid column with coordinate system.

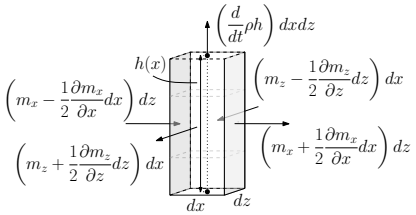

(b) Fluid column with in- and outgoing mass flows.

Figure 3.3: (a) The infinitesimal fluid column containing the fluid element of Figure 3.1. The element is marked with grey dashed lines. (b) Free body diagram including the mass flows into and out of the column. Please note this is per unit width. Adapted from Gohar and Rahnejat [22].

Performing this integration by substitution of the already found velocity profile (Equation (3.5)) under assumptions 3b and 3d leads to:

$$m_x = -\frac{\rho h^3}{12\mu}\frac{\partial p}{\partial x} + \frac{U_1 + U_2}{2}\rho h \tag{3.9}$$

Similar considerations for the z direction gives:

$$m_z = -\frac{\rho h^3}{12\mu}\frac{\partial p}{\partial z} + \frac{W_1 + W_2}{2}\rho h \tag{3.10}$$

3.1.3 The full Reynolds equation

By substitution of Equations (3.9)-(3.10) back into Equation (3.7) and rearranging, the full Reynolds equation is obtained:

$$\frac{\partial}{\partial x}\left(\frac{\rho h^3}{12\mu}\frac{\partial p}{\partial x}\right) + \frac{\partial}{\partial z}\left(\frac{\rho h^3}{12\mu}\frac{\partial p}{\partial z}\right) = \frac{\partial}{\partial x}\left(\frac{U_1 + U_2}{2}\rho h\right) + \frac{\partial}{\partial z}\left(\frac{W_1 + W_2}{2}\rho h\right) + \frac{\mathrm{d}}{\mathrm{d}t}\rho h \tag{3.11}$$

3.1.4 The usual form of Reynolds equation

Within bearing applications, (tangential) velocity occurring from the rotation of the shaft is only taking place in the x direction so $W = 0$. Furthermore

assuming the velocity U is not a function of x and density is constant, i.e. incompressible lubricant, the usual version of Reynolds equation appears:

$$\frac{\partial}{\partial x}\left(\frac{h^3}{12\mu}\frac{\partial p}{\partial x}\right)+\frac{\partial}{\partial z}\left(\frac{h^3}{12\mu}\frac{\partial p}{\partial z}\right)=\frac{U_1+U_2}{2}\frac{\partial h}{\partial x}+\frac{\mathrm{d}}{\mathrm{d}t}h \tag{3.12}$$

Beside the Poiseuille and Couette terms highlighted earlier, the ordinary derivative on the right hand side is called the squeeze term. This term reflects changes in film thickness over time. Changes that might occur due to e.g. the combustion force through a cycle.

Finally, it should be noted that the Reynolds equation belongs to the class of elliptic partial differential equations, [25].

3.2 Non-dimensionalisation

Often it is desirable to use a non-dimensional version of an equation and the field of fluid mechanics is no exception.

To determine the dimensionless variables a relationship is sat up. It is shown in Equation 3.13 for p, but applies to all variables, i.e. h, p, x, z, t.

$$p=\hat{p}\bar{p} \quad , \quad \frac{\partial p}{\partial x}=\frac{\partial(\hat{p}\bar{p})}{\partial(\hat{x}\bar{x})}=\frac{\hat{p}}{\hat{x}}\frac{\partial\bar{p}}{\partial\bar{x}} \tag{3.13}$$

Here p is the physical pressure with the dimension of Pascal. The product consists of a scaling constant $\hat{p}$ also with dimensions of Pascal and a non-dimensional term $\bar{p}$.

Substitution of Equation (3.13) for all variables into Equation (3.12) yields:

$$\frac{1}{\hat{x}}\frac{\partial}{\partial\bar{x}}\left(\frac{(\hat{h}\bar{h})^3}{12\mu}\frac{\hat{p}}{\hat{x}}\frac{\partial\bar{p}}{\partial\bar{x}}\right)+\frac{1}{\hat{z}}\frac{\partial}{\partial\bar{z}}\left(\frac{(\hat{h}\bar{h})^3}{12\mu}\frac{\hat{p}}{\hat{z}}\frac{\partial\bar{p}}{\partial\bar{z}}\right) = \frac{U_1+U_2}{2\hat{x}}\frac{\partial(\hat{h}\bar{h})}{\partial\bar{x}}+\frac{1}{\hat{t}}\frac{\mathrm{d}}{\mathrm{d}\bar{t}}(\hat{h}\bar{h}) \tag{3.14}$$

Being derived in Cartesian coordinates the easiest terms of Equation (3.14) to non-dimensionalise is x and z:

$$\theta=\frac{x}{R} \quad \Leftrightarrow \quad \hat{x}=R, \bar{x}=\theta \tag{3.15}$$

$$\zeta=\frac{z}{R} \quad \Leftrightarrow \quad \hat{z}=R, \bar{z}=\zeta \tag{3.16}$$

The transformation of x follows directly from the transformation between Cartesian and cylindrical coordinates. In a relation similar to circumference and x coordinate, z could be made dimensionless from the length L hence yielding

values of $\zeta = [-\frac{1}{2}, \frac{1}{2}]$. Radius R is chosen, however, to use as few variables as possible.

With the application of θ and ζ, Equation (3.14) is simplified into:

$$\frac{\hat{p}}{6\mu R^2}\left[\frac{\partial}{\partial\theta}\left((\hat{h}\bar{h})^3\,\frac{\partial\bar{p}}{\partial\theta}\right)+\frac{\partial}{\partial\zeta}\left((\hat{h}\bar{h})^3\,\frac{\partial\bar{p}}{\partial\zeta}\right)\right] = \frac{U_1+U_2}{R}\,\frac{\partial(\hat{h}\bar{h})}{\partial\theta}+\frac{2}{\hat{t}}\,\frac{\mathrm{d}}{\mathrm{d}\bar{t}}\,(\hat{h}\bar{h}) \quad (3.17)$$

The factor $(U_1+U_2)/R$ is recognised as the angular velocity ω. Dimensional analysis reveals the velocity term after removing ω only needs non-dimensionalisation of h. In an attempt to obtain values close to unity, the film thickness h is normalised with $\hat{h} = C$. Recalling Equation (2.1) one obtains:

$$\bar{h} = \frac{h}{C} = 1 + \varepsilon\cos\theta \quad (3.18)$$

And thus:

$$\frac{\hat{p}}{6\mu\omega\left(\frac{R}{C}\right)^2}\left[\frac{\partial}{\partial\theta}\left(\bar{h}^3\,\frac{\partial\bar{p}}{\partial\theta}\right)+\frac{\partial}{\partial\zeta}\left(\bar{h}^3\,\frac{\partial\bar{p}}{\partial\zeta}\right)\right] = \frac{\partial\bar{h}}{\partial\theta}+\frac{2}{\omega\hat{t}}\,\frac{\mathrm{d}}{\mathrm{d}\bar{t}}\,\bar{h} \quad (3.19)$$

Equation (3.19) is non-dimensionalised. Letting $\hat{p} = 6\mu\omega\left(R/C\right)^2$ and $\hat{t} = 1/\nu$ yields the final version:

$$\frac{\partial}{\partial\theta}\left(\bar{h}^3\,\frac{\partial\bar{p}}{\partial\theta}\right)+\frac{\partial}{\partial\zeta}\left(\bar{h}^3\,\frac{\partial\bar{p}}{\partial\zeta}\right) = \frac{\partial\bar{h}}{\partial\theta}+\frac{2\nu}{\omega}\,\frac{\mathrm{d}}{\mathrm{d}\bar{t}}\,\bar{h} \quad (3.20)$$

Where:

$$\theta = \frac{x}{R} \quad (3.21)$$

$$\zeta = \frac{z}{R} \quad (3.22)$$

$$\bar{p} = \frac{p}{6\mu\omega\left(\frac{R}{C}\right)^2} \quad (3.23)$$

$$\bar{h} = \frac{h}{C} \quad (3.24)$$

$$\bar{t} = \frac{t}{1/\nu} \quad , \quad \text{often } \nu = \omega \quad (3.25)$$

3.2.1 External mass flow

An extra term can be added to account for the mass flow into the film, e.g. from the pressurised inlet of a hydrostatic bearing.

$$\frac{\partial}{\partial\theta}\left(\bar{h}^3\frac{\partial\bar{p}}{\partial\theta}\right)+\frac{\partial}{\partial\zeta}\left(\bar{h}^3\frac{\partial\bar{p}}{\partial\zeta}\right)=\frac{\partial\bar{h}}{\partial\theta}+\frac{2\nu}{\omega}\frac{\mathrm{d}}{\mathrm{d}\bar{t}}\bar{h}-\frac{2m'}{\rho\omega C} \tag{3.26}$$

Chapter 4

Analytical solutions to Reynolds equation

Generally speaking Reynolds equation is not solvable by analytical means. The only two solutions occur after strong assumptions about the bearing geometry. They are named after the scientists deriving them, i.e. the Sommerfeld solution for an infinitely long bearing (1904) [26] and the Ocvirk solution for a narrow bearing (1952) [27]. The reader should note that the solutions are also referred to as the wide and short bearing theory, respectively.

Being rather nifty some attention will be paid to these solutions in Sections 4.2 and 4.3. First, however, a few expressions of general application will be presented in Section 4.1.

4.1 General expressions

Of general interest for a bearing designer is a few key parameters. The load carrying capacity, Sommerfeld number, losses and oil consumption will be briefly outlined in this section. The content rely to a large extent on the work by Lund [28].

4.1.1 Load carrying capacity

The pressure of the oil film is balancing the imposed load W. Integration over the film yield the force components F_r and F_t, see Figure 4.1. Thus the following equations arise:

$$\left.\begin{matrix} F_r \\ F_t \end{matrix}\right\} = 2\int_0^{L/2}\int_{\theta_1}^{\theta_2} p \left\{\begin{matrix} -\cos\theta \\ \sin\theta \end{matrix}\right\} R\,\mathrm{d}\theta\,\mathrm{d}z \tag{4.1}$$

$$W = \sqrt{F_r^2 + F_t^2} \tag{4.2}$$

A non-dimensional form can be found by usage of the normalisation factor for p in Equation (3.23), see Lund [28]. Here the angular velocity is changed into the rotational frequency N and the area on which the film pressure is working is the effective area of the bearing, $L \times D$.

$$\left.\begin{aligned} f_r &= \frac{F_r}{\mu N D L (R/C)^2} \\ f_t &= \frac{F_t}{\mu N D L (R/C)^2} \end{aligned}\right\} = \frac{6\pi}{L/D}\int_0^{L/D}\int_{\theta_1}^{\theta_2} \bar{p} \left\{\begin{matrix} -\cos\theta \\ \sin\theta \end{matrix}\right\} \mathrm{d}\theta\,\mathrm{d}\zeta \tag{4.3}$$

4.1.2 Attitude angle

Referring to Figure 4.1, the inclination angle between the line of centres and vertical is termed the attitude angle φ. It can be defined from the geometric relationships to be:

$$\tan\varphi = \frac{f_t}{f_r} \tag{4.4}$$

4.1.3 Sommerfeld number

A dimensionless number characterising the bearing is defined as the ratio between the normalisation used in Equation (4.3) and the imposed load. The reader may recall the content of Table 2.1 and see that all the tabulated parameters are presented in one dimensional number called the Sommerfeld number:

$$S = \frac{\mu N D L}{W}\left(\frac{R}{C}\right)^2 = \frac{1}{\sqrt{f_r^2 + f_t^2}} \tag{4.5}$$

Hence it is possible to compare bearings independent of dimensions and operational conditions. In this sense the Sommerfeld number is similar to the Reynolds number, Re, for a given flow domain. Please, note that some authors prefer the inverse definition, i.e. $S = W/\big(\mu N D L (R/C)^2\big)$.

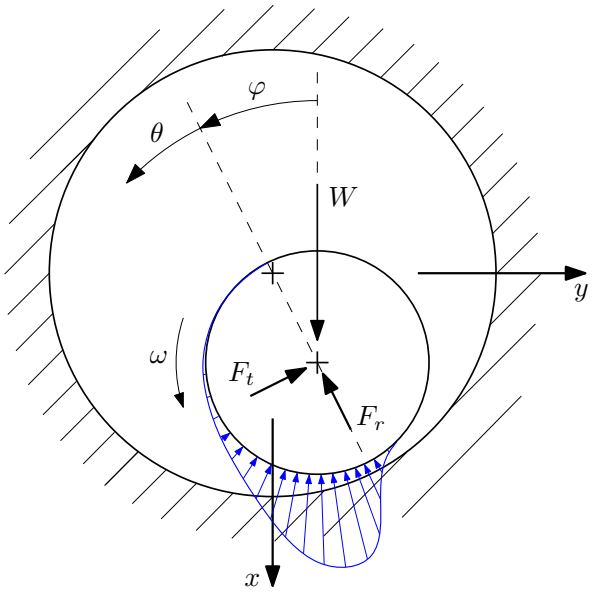

Figure 4.1: Typical pressure distribution for a journal bearing with a vertical load. The force components F_r and F_t equals the pressure integrated over the oil film and thereby balance W.

4.1.4 Losses

The shear stresses acting on the shaft and bearing introduces friction forces. From the assumption of a Newtonian fluid back in Section 3.1 and with no velocity at the housing ($U_1 = 0$) in Equation (3.5), the shear stresses at the housing and the journal, respectively, are:

$$\tau = \mu \frac{\partial u}{\partial y} = \frac{1}{2} \frac{\partial p}{\partial x} (2y - h) + \frac{\mu U_2}{h} \tag{4.6}$$

$$\Downarrow$$

$$\tau_h = -\frac{h}{2} \frac{\partial p}{\partial x} + \frac{\mu U_2}{h}, \tag{4.7}$$

$$\tau_j = \frac{h}{2} \frac{\partial p}{\partial x} + \frac{\mu U_2}{h} \tag{4.8}$$

The indicated sign difference is not violating the requirement for a force equilibrium between the interfaces housing/fluid and fluid/journal. Over one period sign changes in the pressure gradient will cancel out the influence of the sign.

Similarly to the oil film forces, the friction force is found from integration over the bearing surface. Converting directly to the frictional torque, one obtains:

$$R \cdot F_f = 2 \int_0^{L/2} \int_{\theta_1}^{\theta_2} \tau R^2 \, \mathrm{d}\theta \, \mathrm{d}\zeta \tag{4.9}$$

The variables used for the non-dimensioning may seem somewhat arbitrary, but the correct choice can result in some elegant solutions. Lund [28] suggests this way:

$$\bar{M_f} = \frac{1}{S} \frac{R}{C} \frac{F_f}{W} = \frac{\pi}{L/D} \int_0^{L/D} \int_{\theta_1}^{\theta_2} \left(\frac{1}{\bar{h}} + 3\bar{h} \frac{\partial \bar{p}}{\partial \theta} \right) \mathrm{d}\theta \, \mathrm{d}\zeta \tag{4.10}$$

4.1.5 Oil consumption

The volume flow through the bearing are found from the already determined mass flow of Equations (3.9) and (3.10). Being per unit width the integration over the width yields:

$$Q = \frac{2}{\rho} \int_0^{L/2} m_x|_{\theta=\theta_1} \, \mathrm{d}z = \frac{2}{\rho} \int_0^{L/2} m_x|_{\theta=\theta_2} \, \mathrm{d}z + \frac{2}{\rho} \int_{\theta_1}^{\theta_2} m_z|_{z=L/2} \, \mathrm{d}x \tag{4.11}$$

The subscripts of the angle θ indicate start (1) and end of the bearing (2). Depending on the angular arc of interest, $\theta_i = [0, 2\pi]$. For the moment only considering full bearings leads to $\theta_1 = 0$ and $\theta_2 = 2\pi$.

The double equal sign of Equation (4.11) simply indicates that the circumferential flow at the start should equal that of the end plus any axial leak flow. Due to the general design of the journal bearing the leak flow in axial direction is by far the largest.

A dimensionless parallel can be defined as:

$$\begin{aligned} \bar{Q} = \frac{Q}{NDLC} &= \frac{\pi/2}{L/D} \int_0^{L/D} \left[\bar{h} - \bar{h}^3 \frac{\partial \bar{p}}{\partial \theta} \right]_{\theta=\theta_1} \mathrm{d}\zeta \\ &= \frac{\pi/2}{L/D} \left(\int_0^{L/D} \left[\bar{h} - \bar{h}^3 \frac{\partial \bar{p}}{\partial \theta} \right]_{\theta=\theta_2} \mathrm{d}\zeta - \int_{\theta_1}^{\theta_2} \left[\bar{h}^3 \frac{\partial \bar{p}}{\partial \zeta} \right]_{\zeta=L/D} \mathrm{d}\theta \right) \end{aligned} \tag{4.12}$$

4.2 Long Bearing Theory

The long bearing theory has obtained its name after the substitution done by Sommerfeld in 1904 [26] to solve the pressure equation given in Reynolds'

original paper [4]. Reynolds assumed the bearing to be infinitely long, so that the axial gradient could be considered of much less importance than the circumferential gradient, i.e. $L/D \to \infty$ such that $\frac{\partial}{\partial \zeta} \ll \frac{\partial}{\partial \theta}$.

Pressure distribution

For a static analysis the time dependent squeeze contribution $\frac{\mathrm{d}}{\mathrm{d}\bar{t}}$ is equal to zero, why Equation (3.20) for relative pressure as given by Hamrock, Schmid, and Jacobson [Equations (7.50), (10.7) 29] reduces to:

$$\begin{aligned} \frac{\partial}{\partial \theta}\left(\bar{h}^3 \frac{\partial \bar{p}}{\partial \theta}\right) &= \frac{\partial \bar{h}}{\partial \theta} \\ &\Downarrow \\ \frac{\partial \bar{p}}{\partial \theta} &= \frac{1}{\bar{h}^2} - \frac{C_1}{\bar{h}^3} \\ &\Downarrow \\ \bar{p} &= \int_{\theta_1}^{\theta} \left(\frac{1}{\bar{h}^2} - \frac{\bar{h}_m}{\bar{h}^3}\right) \mathrm{d}\theta + \bar{p}_1 \end{aligned} \tag{4.13}$$

Where $\bar{p}_1$ is the non-dimensionalised pressure at θ_1 i.e. at the start of the bearing and $\bar{h}_m$ is the non-dimensional film thickness at maximum/minimum locations and $C_1 = \bar{h}_m$ is found from the condition $\bar{h} = \bar{h}_m$ when $\mathrm{d}\bar{p}/\,\mathrm{d}\theta = 0$.

The integral of Equation (4.13) could only be solved by an approximate method, but Sommerfeld[1] suggested the substitution below to obtain a closed-form solution:

$$\bar{h} = 1 + \varepsilon \cos\theta = \frac{1 - \varepsilon^2}{1 - \varepsilon \cos\psi} \tag{4.14}$$

With this substitution and its relations, which can be seen in Appendix A, the pressure distribution can be found as:

$$\begin{aligned} \bar{p} - \bar{p}_1 = \Bigg(& \frac{1}{(1-\varepsilon^2)^{3/2}} \left(\psi - \varepsilon \sin\psi\right) \\ & - \frac{\bar{h}_m}{(1-\varepsilon^2)^{5/2}} \left[\left(1 + \frac{1}{2}\varepsilon^2\right)\psi - 2\varepsilon \sin\psi + \frac{1}{4}\varepsilon^2 \sin 2\psi\right] \Bigg)_{\psi_1}^{\psi} \end{aligned} \tag{4.15}$$

For a complete bearing $\bar{p}(2\pi) = \bar{p}(0)$, such that with $\psi_1 = 0, \psi = 2\pi$ in Equation (4.15):

$$\bar{h}_m = \frac{1 - \varepsilon^2}{1 + (1/2)\varepsilon^2} \tag{4.16}$$

[1] See Appendix A for a further discussion of this contribution

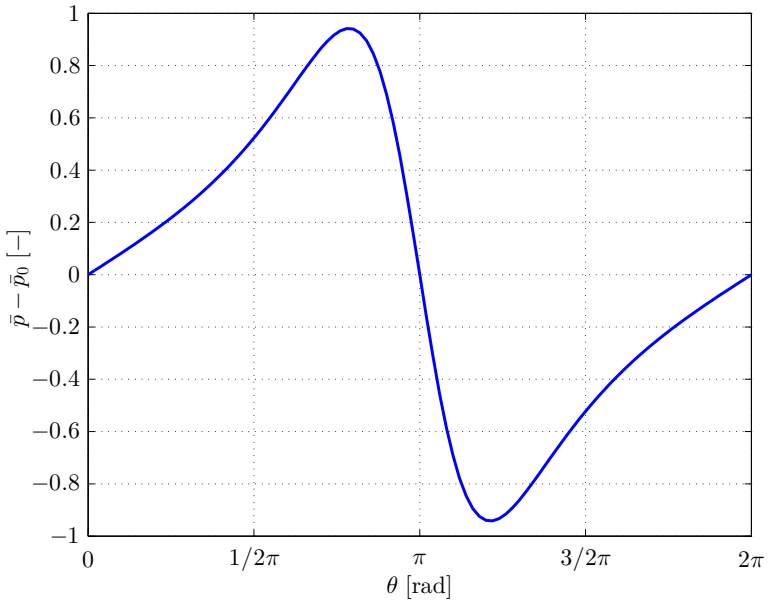

Figure 4.2: The (relative) pressure distribution of the Sommerfeld solution for a wide bearing, Equation (4.18). Notice the antisymmetry yielding $F_r = 0$ due to the cosine term of Equation (4.1). The imposed load W is thus entirely balanced by F_t making the bearing unstable, a situation comparable to that of balancing on the edge of a knife. Referring to Figure 4.1 it can be verified by the line of centres being horizontal as $\varphi = 90°$ and $F_r = 0$.

and thus:

$$\begin{aligned} \bar{p} - \bar{p}_1 &= \left(\frac{\varepsilon \sin\psi}{(2+\varepsilon^2)(1-\varepsilon^2)^{3/2}} (2 - \varepsilon^2 - \varepsilon\cos\psi) \right)_{\psi_1}^{\psi} \\ &= \left(\frac{\varepsilon \sin\theta (2 + \varepsilon\cos\theta)}{(2+\varepsilon^2)(1+\varepsilon\cos\theta)^2} \right)_{\theta_1}^{\theta} \end{aligned} \tag{4.17}$$

Reducing the expression by starting at maximum film thickness, i.e. $\theta_1 = 0$:

$$\bar{p} - \bar{p}_0 = \frac{\varepsilon \sin\theta (2 + \varepsilon\cos\theta)}{(2+\varepsilon^2)(1+\varepsilon\cos\theta)^2} \tag{4.18}$$

The distribution is plotted in Figure 4.2.

Load carrying capacity

Inserting the pressure of Equation (4.18) into (4.3) yields with partial integration:

$$\begin{aligned}\left.\begin{matrix} f_r \\ f_t \end{matrix}\right\} &= 6\pi \int_{\theta_1}^{\theta_2} \bar{p} \left\{\begin{matrix} -\cos\theta \\ \sin\theta \end{matrix}\right\} \mathrm{d}\theta \\ &= 6\pi \left(-\bar{p} \left\{\begin{matrix} \sin\theta \\ \cos\theta \end{matrix}\right\}_{\theta_1}^{\theta_2} + \int_{\theta_1}^{\theta_2} \frac{\partial \bar{p}}{\partial \theta} \left\{\begin{matrix} \sin\theta \\ \cos\theta \end{matrix}\right\} \mathrm{d}\theta \right) \\ &= 6\pi \left(-\bar{p} \left\{\begin{matrix} \sin\theta \\ \cos\theta \end{matrix}\right\}_{\theta_1}^{\theta_2} + \int_{\theta_1}^{\theta_2} \left(\frac{1}{\bar{h}^2} - \frac{\bar{h}_m}{\bar{h}^3} \right) \left\{\begin{matrix} \sin\theta \\ \cos\theta \end{matrix}\right\} \mathrm{d}\theta \right)\end{aligned} \tag{4.19}$$

With the Sommerfeld substitution and $\bar{p}(\theta = \theta_1) = \bar{p}(\theta = \theta_2) = 0$, the expression reduces to:

$$f_r = \left[\frac{6\pi}{\varepsilon \bar{h}^2} \left(\bar{h} - \frac{1}{2} \bar{h}_m \right) \right]_{\theta_1}^{\theta_2} \tag{4.20}$$

$$\begin{aligned} f_t = \frac{6\pi}{(1-\varepsilon^2)^{3/2}} \Bigg[&\sin\psi - \varepsilon\psi - \\ &\frac{\bar{h}_m}{(1-\varepsilon^2)} \left((1+\varepsilon^2)\sin\psi - \frac{3}{2}\varepsilon\psi - \frac{1}{4}\varepsilon \sin 2\psi \right) \Bigg]_{\psi_1}^{\psi_2} \end{aligned} \tag{4.21}$$

Assuming a complete bearing $\theta_2 - \theta_1 = 2\pi$ and with $\bar{h}_m$ from Equation (4.16) the result is the unstable bearing as explained in Figure 4.2:

$$f_r = 0 \tag{4.22}$$

$$f_t = \frac{12\pi^2 \varepsilon}{(2+\varepsilon^2)\sqrt{1-\varepsilon^2}} \tag{4.23}$$

Attitude angle

With the definition of Equation (4.4) the attitude angle will be:

$$\tan\varphi = \frac{f_t}{f_r} = \infty \tag{4.24}$$

Sommerfeld number

From Equation (4.5) the Sommerfeld number is reduced to the inverse of the tangential load component:

$$S = \frac{1}{f_t} = \frac{(2+\varepsilon^2)\sqrt{1-\varepsilon^2}}{12\pi^2\varepsilon} \tag{4.25}$$

4.2.1 Half bearing solution

The unstable bearing depicted in the equations above is in most cases not the correct approximation. Due to the negative film pressures often being larger (absolute value) than the lubricant can withstand because of surface tension, the lubricant will start to cavitate. Hence only ambient pressures being high enough, to ensure minimum pressure is above the threshold of the tension capabilities of the oil will make the above solution realistic.

If the negative pressure is simply neglected, i.e. $p(\pi \leq \theta \leq 2\pi) = 0$, a better approximation arises. This assumption models a partial bearing with an interval of 0 to π rad, i.e. a half bearing. It is therefore known as the half-Sommerfeld or Gümbel solution and yields:

$$f_r = \frac{12\pi\varepsilon^2}{(2+\varepsilon^2)(1-\varepsilon^2)} \tag{4.26}$$

$$f_t = \frac{6\pi^2\varepsilon}{(2+\varepsilon^2)\sqrt{1-\varepsilon^2}} \tag{4.27}$$

$$\tan\varphi = \frac{\pi}{2}\frac{\sqrt{1-\varepsilon^2}}{\varepsilon} \tag{4.28}$$

$$S = \frac{(2+\varepsilon^2)\sqrt{1-\varepsilon^2}}{12\pi^2\varepsilon} \tag{4.29}$$

4.3 Narrow Bearing Theory

The approach of the narrow bearing theory is similar to that of the wide bearing theory. Ocvirk found from the volume flow that the Couette flow was superior to the Poiseuille flow for shorter bearings [27]. Requiring $L/D \to 0$ justified the assumption $\bar{h}^3 \partial\bar{p}/\partial\theta \sim 0$ and Equation (3.20) now becomes:

$$\frac{\partial}{\partial\zeta}\left(\bar{h}^3\frac{\partial\bar{p}}{\partial\zeta}\right) = \frac{\partial\bar{h}}{\partial\theta} \tag{4.30}$$

Pressure distribution

Contrary to Equation (4.13), Equation (4.30) is easily integrated. The conditions of $\partial\bar{p}/\partial\zeta = 0$ at $\zeta = 0$ and $\bar{p} = 0$ at $\zeta = \pm(L/2)/R = \pm L/D$ gives:

$$\bar{p} = \frac{1}{2}\left[\left(\frac{L}{D}\right)^2 - \zeta^2\right]\frac{\varepsilon \sin\theta}{\bar{h}^3} \tag{4.31}$$

It is interesting to note that this solution incorporates the L/D ratio, which is one of the main bearing characterisation parameters as indicated in Section 2.1. Ocvirk mentions reasonable agreement for ratios with an upper limit of $L/D \sim 1$, while $L/D \leq 0.5$ is considered to be acceptable today.

Load carrying capacity

Equation (4.3) can yield the special case of narrow bearing load carrying capacity with insertion of the just found pressure distribution (Equation (4.31)) and applying the Sommerfeld substitution of Section 4.2, namely Equation (4.14) together with the expansions in Equations (A.2)-(A.4). This holds for $0 \leq \theta \leq \pi$

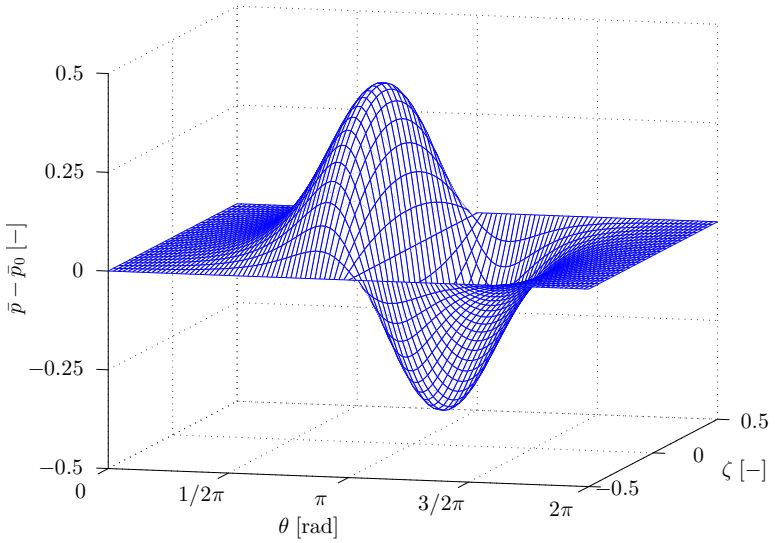

Figure 4.3: Illustration of the three dimensional Ocvirk solution, sinesoidal in the circumferential direction and quadratic in axial direction, respectively.

i.e. the Gümbel or half-Sommerfeld Solution:

$$\left.\begin{matrix} f_r \\ f_t \end{matrix}\right\} = 2\pi\varepsilon\left(\frac{L}{D}\right)^2 \int_0^{\pi} \frac{\sin\theta}{\bar{h}^3} \left\{\begin{matrix} -\cos\theta \\ \sin\theta \end{matrix}\right\} R\,\mathrm{d}\theta = \begin{cases} \pi\left(\dfrac{L}{D}\right)^2 \dfrac{4\varepsilon^2}{(1-\varepsilon^2)^2} \\ \pi^2\left(\dfrac{L}{D}\right)^2 \dfrac{\varepsilon}{(1-\varepsilon^2)^{3/2}} \end{cases} \tag{4.32}$$

Considering the entire bearing so $0 \leq \theta \leq 2\pi$, gives:

$$\left.\begin{matrix} f_r \\ f_t \end{matrix}\right\} = 2\pi\varepsilon\left(\frac{L}{D}\right)^2 \int_0^{2\pi} \frac{\sin\theta}{\bar{h}^3} \left\{\begin{matrix} -\cos\theta \\ \sin\theta \end{matrix}\right\} R\,\mathrm{d}\theta = \begin{cases} 0 \\ \pi^2\left(\dfrac{L}{D}\right)^2 \dfrac{2\varepsilon}{(1-\varepsilon^2)^{3/2}} \end{cases} \tag{4.33}$$

Sommerfeld number and attitude angle

Hence, from Equation (4.4) and (4.5), respectively, the attitude angle and the Sommerfeld number are:

$$\tan\varphi = \frac{\pi\sqrt{1-\varepsilon^2}}{4\varepsilon} \tag{4.34}$$

$$S = \frac{1}{\pi(L/D)^2} \frac{(1-\varepsilon^2)^2}{\varepsilon\sqrt{16\varepsilon^2 + \pi^2(1-\varepsilon^2)}} \tag{4.35}$$

4.4 Locus curves

As mentioned in Section 2.1, the hydrodynamic forces influence in a way such that the shaft is not just lifted vertically towards the center of the housing as the velocity and thus Sommerfeld number increases towards infinity.

Using polar coordinates to mimic the circular geometry of the problem and plotting the attitude angle φ as function of the eccentricity ratio ε leads to the so-called locus curve. Figure 4.4 contains the locus curves for the long and short bearing solutions, respectively. Here it can be seen that the axial gradients of the short solution leads to a higher overall pressure, resulting in less eccentricity for the same attitude angle.

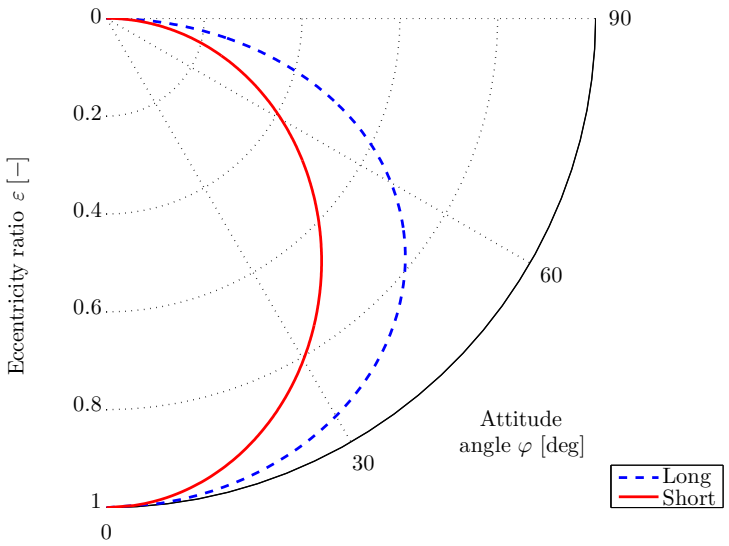

Figure 4.4: Locus curves for the long and short bearing solutions, respectively. The curves occur from Equations (4.28) and (4.34).

Chapter 5

Journal orbit calculations

This chapter outlines the perturbation method used by Lund and Thomsen [30] to establish the journal orbit from the dynamic coefficients of the bearing. The derived perturbation expressions will be used for formulating the corresponding finite element equations in Chapter 6. The solution of those equations will lead to the dynamic coefficients, and ultimately, the journal orbit.

5.1 Spring-damper system

For the dynamic load case, the journal can be considered to be suspended by the oil film. The balance between imposed load and the compressive forces of the oil film is modelled by the spring-damper system shown in Figure 5.1.

The link between the forces just mentioned and the journal movements, is given with the (non-dimensional) stiffness and damping coefficients:

$$\bar{K}_{xx} = \frac{\partial \bar{F}_x}{\partial \bar{x}}\,, \quad \bar{K}_{yx} = \frac{\partial \bar{F}_y}{\partial \bar{x}}\,, \quad \bar{K}_{xy} = \frac{\partial \bar{F}_x}{\partial \bar{y}}\,, \quad \bar{K}_{yy} = \frac{\partial \bar{F}_y}{\partial \bar{y}} \tag{5.1}$$

$$\bar{B}_{xx} = \frac{\partial \bar{F}_x}{\partial \dot{\bar{x}}}\,, \quad \bar{B}_{yx} = \frac{\partial \bar{F}_y}{\partial \dot{\bar{x}}}\,, \quad \bar{B}_{xy} = \frac{\partial \bar{F}_x}{\partial \dot{\bar{y}}}\,, \quad \bar{B}_{yy} = \frac{\partial \bar{F}_y}{\partial \dot{\bar{y}}} \tag{5.2}$$

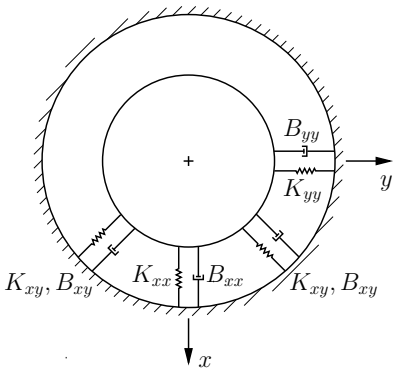

Figure 5.1: Illustration of the spring-damper system representing the oil film forces.

5.2 The perturbation method

Recall the non-dimensional version of Reynolds equation is given as:

$$\frac{\partial}{\partial\theta}\left(\bar{h}^3\,\frac{\partial\bar{p}}{\partial\theta}\right)+\frac{\partial}{\partial\zeta}\left(\bar{h}^3\,\frac{\partial\bar{p}}{\partial\zeta}\right)=\frac{\partial\bar{h}}{\partial\theta}+\frac{2\nu}{\omega}\,\frac{\mathrm{d}\bar{h}}{\mathrm{d}\tau} \tag{5.3}$$

The film thickness can be expressed as below, cf. Figure 5.2:

$$\bar{h}=1+\varepsilon\cos\theta=1+\varepsilon\cos(\theta'-\varphi)=1+\bar{x}\cos\theta'+\bar{y}\sin\theta' \tag{5.4}$$

The global angular coordinate θ' is now introduced as a replacement for the local coordinate θ as used in Chapters 3 and 4. The reasoning behind this, is the easier specification of boundary conditions, as fixed locations, e.g. an inlet, now is fixed, contrary to the local coordinate notation with a fixed location of the film and varying location of the inlet. As seen in Equation (5.4) the definition is just an offset $\theta=\theta'-\varphi$, such that all equations of Chapters 3 and 4 are still valid. Performing an infinitesimal perturbation, and letting the equilibrium position be designated with subscript '0', the journal center position and velocity can be described as:

$$\bar{x}=\bar{x}_0+\Delta\bar{x} \tag{5.5a}$$
$$\bar{y}=\bar{y}_0+\Delta\bar{y} \tag{5.5b}$$
$$\dot{\bar{x}}=\dot{\bar{x}}_0+\Delta\dot{\bar{x}} \tag{5.5c}$$
$$\dot{\bar{y}}=\dot{\bar{y}}_0+\Delta\dot{\bar{y}} \tag{5.5d}$$

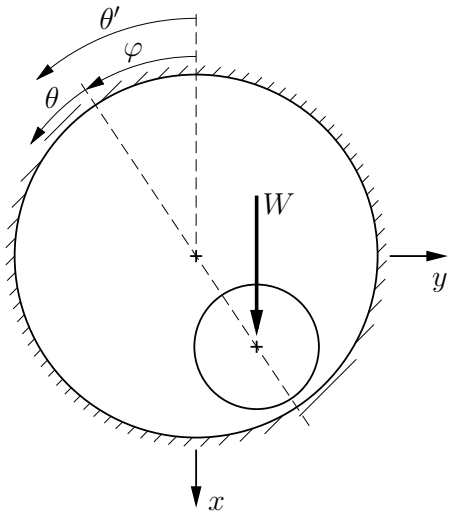

Figure 5.2: Definition of coordinate system and relationship between the global and local angular coordinates θ' and θ, respectively, and the attitude angle φ.

The film thickness can now be rewritten by insertion of Equation (5.5) into Equation (2.1) and rearranging:

$$\bar{h} = \underbrace{1 + \bar{x}_0 \cos\theta' + \bar{y}_0 \sin\theta'}_{\bar{h}_0} + \Delta\bar{x}\cos\theta' + \Delta\bar{y}\sin\theta' \tag{5.6}$$

Hence the time derivative of $\bar{h}$ becomes:

$$\frac{\mathrm{d}\bar{h}}{\mathrm{d}\tau} = \dot{\bar{x}}_0 \cos\theta' + \dot{\bar{y}}_0 \sin\theta' + \Delta\dot{\bar{x}}\cos\theta' + \Delta\dot{\bar{y}}\sin\theta' \tag{5.7}$$

Neglecting higher order terms, the cubic term for the film thickness is:

$$\bar{h}^3 = \bar{h}_0^3 + 3\bar{h}_0^2\Delta\bar{x}\cos\theta' + 3\bar{h}_0^2\Delta\bar{y}\sin\theta' \tag{5.8}$$

Applying the same perturbation principle to the pressure gives:

$$\bar{p} = \bar{p}_0 + \Delta\bar{x}\bar{p}_1 + \Delta\bar{y}\bar{p}_2 + \Delta\dot{\bar{x}}\bar{p}_3 + \Delta\dot{\bar{y}}\bar{p}_4 \tag{5.9}$$

The four expressions $\bar{p}_i, i = 1, \ldots, 4$ are:

$$\bar{p}_1 = \frac{\mathrm{d}\bar{p}}{\mathrm{d}\bar{x}}\,, \quad \bar{p}_2 = \frac{\mathrm{d}\bar{p}}{\mathrm{d}\bar{y}}\,, \quad \bar{p}_3 = \frac{\mathrm{d}\bar{p}}{\mathrm{d}\dot{\bar{x}}}\,, \quad \bar{p}_4 = \frac{\mathrm{d}\bar{p}}{\mathrm{d}\dot{\bar{y}}} \tag{5.10}$$

Inserting Equations (5.7)-(5.9) in Equation (3.12) gives:

$$\begin{aligned}
&\frac{\partial}{\partial\theta}\left[\left(\bar{h}_0^3+3\bar{h}_0^2\Delta\bar{x}\cos\theta'+3\bar{h}_0^2\Delta\bar{y}\sin\theta'\right)\frac{\partial}{\partial\theta}\left(\bar{p}_0+\Delta\bar{x}\bar{p}_1+\Delta\bar{y}\bar{p}_2+\Delta\dot{\bar{x}}\bar{p}_3+\Delta\dot{\bar{y}}\bar{p}_4\right)\right]+\\
&\frac{\partial}{\partial\zeta}\left[\left(\bar{h}_0^3+3\bar{h}_0^2\Delta\bar{x}\cos\theta'+3\bar{h}_0^2\Delta\bar{y}\sin\theta'\right)\frac{\partial}{\partial\zeta}\left(\bar{p}_0+\Delta\bar{x}\bar{p}_1+\Delta\bar{y}\bar{p}_2+\Delta\dot{\bar{x}}\bar{p}_3+\Delta\dot{\bar{y}}\bar{p}_4\right)\right]=\\
&\frac{\partial}{\partial\theta}\left(\bar{h}_0+\Delta\bar{x}\cos\theta'+\Delta\bar{y}\sin\theta'\right)+\frac{2\nu}{\omega}\left(\dot{\bar{x}}_0\cos\theta'+\dot{\bar{y}}_0\sin\theta'+\Delta\dot{\bar{x}}\cos\theta'+\Delta\dot{\bar{y}}\sin\theta'\right)
\end{aligned}\tag{5.11}$$

Equation (5.11) is split up into five equations, one for each of the perturbation terms:

$$\begin{aligned}
\frac{\partial}{\partial\theta}\left(\bar{h}_0^3\frac{\partial\bar{p}_0}{\partial\theta}\right)+\frac{\partial}{\partial\zeta}\left(\bar{h}_0^3\frac{\partial\bar{p}_0}{\partial\zeta}\right)&=\left(-\bar{x}_0\sin\theta'+\bar{y}_0\cos\theta'\right)+\\
&\quad\frac{2\nu}{\omega}\left(\dot{\bar{x}}_0\cos\theta'+\dot{\bar{y}}_0\sin\theta'\right)
\end{aligned}\tag{5.12a}$$

$$\begin{aligned}
\frac{\partial}{\partial\theta}\left(\bar{h}_0^3\frac{\partial\bar{p}_1}{\partial\theta}\right)+\frac{\partial}{\partial\zeta}\left(\bar{h}_0^3\frac{\partial\bar{p}_1}{\partial\zeta}\right)&=-\frac{\partial}{\partial\theta}\left(3\bar{h}_0^2\cos\theta'\frac{\partial\bar{p}_0}{\partial\theta}\right)-\\
&\quad\frac{\partial}{\partial\zeta}\left(3\bar{h}_0^2\cos\theta'\frac{\partial\bar{p}_0}{\partial\zeta}\right)-\sin\theta'
\end{aligned}\tag{5.12b}$$

$$\begin{aligned}
\frac{\partial}{\partial\theta}\left(\bar{h}_0^3\frac{\partial\bar{p}_2}{\partial\theta}\right)+\frac{\partial}{\partial\zeta}\left(\bar{h}_0^3\frac{\partial\bar{p}_2}{\partial\zeta}\right)&=-\frac{\partial}{\partial\theta}\left(3\bar{h}_0^2\sin\theta'\frac{\partial\bar{p}_0}{\partial\theta}\right)-\\
&\quad\frac{\partial}{\partial\zeta}\left(3\bar{h}_0^2\sin\theta'\frac{\partial\bar{p}_0}{\partial\zeta}\right)+\cos\theta'
\end{aligned}\tag{5.12c}$$

$$\frac{\partial}{\partial\theta}\left(\bar{h}_0^3\frac{\partial\bar{p}_3}{\partial\theta}\right)+\frac{\partial}{\partial\zeta}\left(\bar{h}_0^3\frac{\partial\bar{p}_3}{\partial\zeta}\right)=\frac{2\nu}{\omega}\cos\theta'\tag{5.12d}$$

$$\frac{\partial}{\partial\theta}\left(\bar{h}_0^3\frac{\partial\bar{p}_4}{\partial\theta}\right)+\frac{\partial}{\partial\zeta}\left(\bar{h}_0^3\frac{\partial\bar{p}_4}{\partial\zeta}\right)=\frac{2\nu}{\omega}\sin\theta'\tag{5.12e}$$

When solving for $\bar{p}_i, i=1,\ldots,4$ it is seen the five left hand sides are equal, such that only the right hand side varies.

5.3 Shaft position iterations

The solution procedure from [30] is outlined more in detail in Lund's unpublished lecture notes form the 1970's, [28].

From Newton's second law of motion:

$$M\ddot{x} = \bar{W}_x - \bar{F}_x \tag{5.13a}$$
$$M\ddot{y} = \bar{W}_y - \bar{F}_y \tag{5.13b}$$

Here M is the mass of the journal, the double-dot symbolises the second derivative with respect to time, $\bar{W}_i$ is the imposed load components (including inertia) and $\bar{F}_i$ is the load capacity components generated by the film. As the displacements of the journal within the housing are very small, the acceleration-mass product is assumed to be neglectible compared to be combustion forces and hence:

$$\bar{W}_x = \bar{F}_x \tag{5.14a}$$
$$\bar{W}_y = \bar{F}_y \tag{5.14b}$$

In keeping with the spring-damper analogy of Section 5.1 and the hydro*dynamic* Reynolds equation, the load carrying capacity is a function of:

$$F_i = F_i(x, y, \dot{x}, \dot{y}, \Omega), \quad i = x, y, \quad \Omega = \omega_j + \omega_h \tag{5.15}$$

To ensure force balance one needs to know journal velocity. As the Reynolds equation is non-linear this is done iteratively for a certain number of load steps. Let k designate the load step and j the (inner) iteration on velocity.

From the Taylor expansion performed in connection with the perturbation, it can be seen that F is represented by:

$$\bar{F}_x = \bar{F}_x\big(x_k, y_k, (\dot{x}_k)_j, (\dot{y}_k)_j, \Omega_k\big) + \big(\bar{B}_{xx}\big)_j \Delta\dot{x}_j + \big(\bar{B}_{xy}\big)_j \Delta\dot{y}_j \tag{5.16a}$$
$$\bar{F}_y = \bar{F}_y\big(x_k, y_k, (\dot{x}_k)_j, (\dot{y}_k)_j, \Omega_k\big) + \big(\bar{B}_{yx}\big)_j \Delta\dot{x}_j + \big(\bar{B}_{yy}\big)_j \Delta\dot{y}_j \tag{5.16b}$$

The four damping coefficients B_{ij} are given in Equation (5.2) and are approximated with the perturbation outlined above. Similarly to the non-perturbed solution of Reynolds equation given in Section 4.1.1, the film forces and dynamic

coefficients are found from:

$$\left.\begin{matrix}\bar{F}_x \\ \bar{F}_y\end{matrix}\right\} = \frac{6\pi}{L/D}\int_0^{L/D}\int_{\theta_1}^{\theta_2} \bar{p}_0 \left\{\begin{matrix}-\cos\theta' \\ -\sin\theta'\end{matrix}\right\} \mathrm{d}\theta\,\mathrm{d}\zeta \tag{5.17a}$$

$$\left.\begin{matrix}\bar{K}_{xx} \\ \bar{K}_{yx}\end{matrix}\right\} = \frac{6\pi}{L/D}\int_0^{L/D}\int_{\theta_1}^{\theta_2} \bar{p}_1 \left\{\begin{matrix}-\cos\theta' \\ -\sin\theta'\end{matrix}\right\} \mathrm{d}\theta\,\mathrm{d}\zeta \tag{5.17b}$$

$$\left.\begin{matrix}\bar{K}_{xy} \\ \bar{K}_{yy}\end{matrix}\right\} = \frac{6\pi}{L/D}\int_0^{L/D}\int_{\theta_1}^{\theta_2} \bar{p}_2 \left\{\begin{matrix}-\cos\theta' \\ -\sin\theta'\end{matrix}\right\} \mathrm{d}\theta\,\mathrm{d}\zeta \tag{5.17c}$$

$$\left.\begin{matrix}\bar{B}_{xx} \\ \bar{B}_{yx}\end{matrix}\right\} = \frac{6\pi}{L/D}\int_0^{L/D}\int_{\theta_1}^{\theta_2} \bar{p}_3 \left\{\begin{matrix}-\cos\theta' \\ -\sin\theta'\end{matrix}\right\} \mathrm{d}\theta\,\mathrm{d}\zeta \tag{5.17d}$$

$$\left.\begin{matrix}\bar{B}_{xy} \\ \bar{B}_{yy}\end{matrix}\right\} = \frac{6\pi}{L/D}\int_0^{L/D}\int_{\theta_1}^{\theta_2} \bar{p}_4 \left\{\begin{matrix}-\cos\theta' \\ -\sin\theta'\end{matrix}\right\} \mathrm{d}\theta\,\mathrm{d}\zeta \tag{5.17e}$$

Rearranging Equation (5.16) leads to:

$$\begin{bmatrix}\left(\bar{B}_{xx}\right)_j & \left(\bar{B}_{xy}\right)_j \\ \left(\bar{B}_{yx}\right)_j & \left(\bar{B}_{yy}\right)_j\end{bmatrix}\left\{\begin{matrix}\Delta\dot{x}_j \\ \Delta\dot{y}_j\end{matrix}\right\} = \left\{\begin{matrix}\left(\bar{W}_x\right)_k - \bar{F}_x\big(x_k, y_k, (\dot{x}_k)_j, (\dot{y}_k)_j, \Omega_k\big) \\ \left(\bar{W}_y\right)_k - \bar{F}_y\big(x_k, y_k, (\dot{x}_k)_j, (\dot{y}_k)_j, \Omega_k\big)\end{matrix}\right\} \tag{5.18}$$

The incremental change is used to update the velocity by a first order Euler method:

$$(\dot{x}_k)_{j+1} = (\dot{x}_k)_j + \Delta\dot{x}_j \tag{5.19a}$$

$$(\dot{y}_k)_{j+1} = (\dot{y}_k)_j + \Delta\dot{y}_j \tag{5.19b}$$

The convergence of the velocity iterations is assessed by a norm:

$$\frac{\left|\left(\bar{W}_x\right)_k - \bar{F}_x\big(x_k, y_k, (\dot{x}_k)_j, (\dot{y}_k)_j, \Omega_k\big)\right|}{\left|\left(\bar{W}_x\right)_k\right| + \left|\left(\bar{W}_y\right)_k\right|} + \frac{\left|\left(\bar{W}_y\right)_k - \bar{F}_y\big(x_k, y_k, (\dot{x}_k)_j, (\dot{y}_k)_j, \Omega_k\big)\right|}{\left|\left(\bar{W}_x\right)_k\right| + \left|\left(\bar{W}_y\right)_k\right|} <\sim 10^{-5} \tag{5.20}$$

With a converged velocity, the position of the shaft for the next load step can be established, since the time span between two consecutive loads is known:

$$x_{k+1} = x_k + \Delta t\dot{x}_k \tag{5.21a}$$

$$y_{k+1} = y_k + \Delta t\dot{y}_k \tag{5.21b}$$

In this way the journal orbit can be found from time integration of a sequence of load steps. For a cyclic process like that of an internal combustion engine, the orbit may converge after a few cycles.

Chapter 6

Finite element implementation

The equations of Chapters 3-5 are sought approximated, and hence discretised, by the finite element method (FE). First, the basic principles of the finite element method will be demonstrated and applied to the static form of Reynolds equation, see Equation (3.20), forming Section 6.1. Secondly, the equations allowing for the time integration needed to solve dynamic version will be presented in Section 6.2.

The FE formulation is written in MATLAB R2012a, thought of as a standalone suite but also prepared for interfacing with other packages employed at e.g. MAN Diesel & Turbo.

No matter the time formulation considered, it is important to note that the journal bearing problem is an *indirect* or inverse problem as mentioned by Mourelatos [31] and Kumar and Booker [32]. This means that an equilibrium is sought between an external load being specified and a resulting, calculated journal position, instead of the forward process of specifying a position and computing the corresponding load carrying capacity.

6.1 Static version

Recall, from a reduced form of Equation (3.19), the non-dimensional, steady version of Reynolds equation as:

$$\frac{\partial}{\partial \theta'}\left(\bar{h}^3 \frac{\partial \bar{p}}{\partial \theta'}\right) + \frac{\partial}{\partial \zeta}\left(\bar{h}^3 \frac{\partial \bar{p}}{\partial \zeta}\right) = \frac{\partial \bar{h}}{\partial \theta'} \tag{6.1}$$

Notice, the change from local (θ) to global angular coordinate (θ'). Equation (6.1) can be rearranged to the form $f\big(\bar{p}(\theta', \zeta)\big) = 0$:

$$\frac{\partial}{\partial \theta'}\left(\bar{h}^3 \frac{\partial \bar{p}}{\partial \theta'}\right) + \frac{\partial}{\partial \zeta}\left(\bar{h}^3 \frac{\partial \bar{p}}{\partial \zeta}\right) - \frac{\partial \bar{h}}{\partial \theta'} = 0 \tag{6.2}$$

The pressure distribution $\bar{p}$ is discretised by elements. Internally in the element, the pressure distribution is described by weights. An approximation of the actual pressure is thus done by:

$$\tilde{p}(\theta', \zeta) = \sum_{i=1}^{n} N_i(\theta', \zeta)\bar{p}_i \tag{6.3}$$

Here N_i is the weights or so-called shape functions and n is the number of degrees of freedom. For a single element the shape functions can also be listed as the (row) vector quantity:

$$\mathbf{N} = \{N_1, N_2, \cdots, N_n\} \tag{6.4}$$

Using Equation (6.3), the resulting approximation introduces a residual:

$$R = D\tilde{p} - f \qquad \text{in domain } V \tag{6.5}$$

Where D is a derivative operator, $\tilde{p}$ is the sought, approximated solution to the differential equation considered and f is some function (e.g. the right hand side of Equation (6.1)). The residual will have to be bounded to obtain a meaningful solution to the problem in hand. This can be ensured through assigning weights to the individual contributions from the residual, and prescribing the sum of residuals over the domain volume V is equal to zero.

$$\int_V W_i R \,\mathrm{d}V = 0, \qquad \text{for} \qquad i = 1, 2, \ldots, n \tag{6.6}$$

In this work the Galerkin method of weighted residuals is used Cook et al. [33], and W_i is here the shape functions N_i.

The residual definition of Equation (6.5) is equivalent to Equation (6.2), so insertion into Equation (6.6) yields for a single element:

$$\int_{A^e} \mathbf{N}^T \left[\frac{\partial}{\partial \theta'}\left(\bar{h}^3 \frac{\partial \bar{\mathbf{p}}}{\partial \theta'}\right) + \frac{\partial}{\partial \zeta}\left(\bar{h}^3 \frac{\partial \bar{\mathbf{p}}}{\partial \zeta}\right) - \frac{\partial \bar{h}}{\partial \theta'}\right] \mathrm{d}A^e = 0 \tag{6.7}$$

The Green-Gauss theorem states a relationship for the integral of a scalar-vector derivative product:

$$\int_A \beta \frac{\partial \mathbf{f}}{\partial \theta'} \,\mathrm{d}A = \int_S \beta \mathbf{f} n_{\theta'} \,\mathrm{d}S - \int_A \frac{\partial \beta}{\partial \theta'} \mathbf{f} \,\mathrm{d}A \tag{6.8}$$

The application of the Green-Gauss theorem is performed in Appendix B. The surface integral terms are ignored, as they only describe the flow over the edges of the bearing, and do not contribute to the pressure distribution as such.

$$-\int_{A^e}\left(\frac{\partial \mathbf{N}}{\partial \theta'}\right)^T \bar{h}^3 \frac{\partial \bar{\mathbf{p}}}{\partial \theta'}\,\mathrm{d}A^e - \int_{A^e}\left(\frac{\partial \mathbf{N}}{\partial \zeta}\right)^T \bar{h}^3 \frac{\partial \bar{\mathbf{p}}}{\partial \zeta}\,\mathrm{d}A^e + \int_{A^e}\left(\frac{\partial \mathbf{N}}{\partial \theta}\right)^T \bar{h}\,\mathrm{d}A^e = 0 \tag{6.9}$$

Utilising the fact that an approximated function is derived through the shape function, i.e. $\tilde{p}' = \sum_{i=1}^{n} N_i' p_i$, and collecting terms, we get:

$$-\int_{A^e} \bar{h}^3 \left[\left(\frac{\partial \mathbf{N}}{\partial \theta'}\right)^T \left(\frac{\partial \mathbf{N}}{\partial \theta'}\right) - \left(\frac{\partial \mathbf{N}}{\partial \zeta}\right)^T \left(\frac{\partial \mathbf{N}}{\partial \zeta}\right)\right] \mathrm{d}A^e \bar{\mathbf{p}} = -\int_{A^e}\left(\frac{\partial \mathbf{N}}{\partial \theta'}\right)^T \bar{h}\,\mathrm{d}A^e \tag{6.10}$$

The non-linear Reynolds equation is hence transformed to a linear system of equations for a single finite element:

$$\bar{\mathbf{K}}^e \bar{\mathbf{p}}^e = \bar{\mathbf{u}}^e \tag{6.11}$$

Where

$$\bar{\mathbf{K}}^e = -\int_{A^e} \bar{h}^3 \left[\left(\frac{\partial \mathbf{N}}{\partial \theta'}\right)^T \left(\frac{\partial \mathbf{N}}{\partial \theta'}\right) - \left(\frac{\partial \mathbf{N}}{\partial \zeta}\right)^T \left(\frac{\partial \mathbf{N}}{\partial \zeta}\right)\right] \mathrm{d}A^e \tag{6.12a}$$

$$\bar{\mathbf{p}}^e = \{\bar{p}_1, \bar{p}_2, \cdots, \bar{p}_n\}^T \tag{6.12b}$$

$$\bar{\mathbf{u}}^e = -\int_{A^e}\left(\frac{\partial \mathbf{N}}{\partial \theta'}\right)^T \bar{h}\,\mathrm{d}A^e \tag{6.12c}$$

Numerical integration

To maintain a general code, the integration over the elements are performed numerically, although analytical solutions exists for very simple elements.

Using isoparametric, or natural, coordinates the coordinate system changes from a physical to a mathematical, see Figure 6.1. In other words, there is a change from arbitrary coordinates to a smooth and nice set: $(x, y) \Leftrightarrow (\xi, \eta) \in [-1, 1]$. The Jacobian matrix gives the relationship between the two coordinate systems:

$$J = \begin{bmatrix} \dfrac{\partial x}{\partial \xi} & \dfrac{\partial y}{\partial \xi} \\ \dfrac{\partial x}{\partial \eta} & \dfrac{\partial y}{\partial \eta} \end{bmatrix}, \qquad \mathrm{d}A = \mathrm{d}x\,\mathrm{d}y = |\det J|\,\mathrm{d}\xi\,\mathrm{d}\eta \tag{6.13}$$

With the Gauss-Legendre formula, an integral I can be evaluated as:

$$I = \int_{-1}^{1}\int_{-1}^{1} p(\xi, \eta)\,\mathrm{d}\xi\,\mathrm{d}\eta = \sum_{k=1}^{n}\sum_{l=1}^{n} a_k a_l p(\xi_k, \eta_l) \tag{6.14}$$

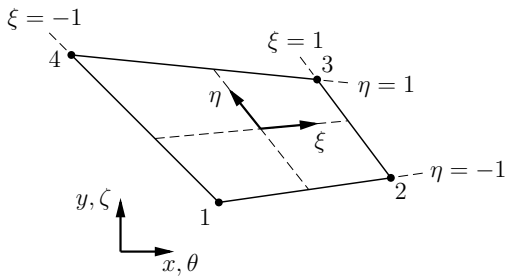

Figure 6.1: Physical, cartesian coordinates and mathematical, isoparametric coordinates. Inspired from [33].

Here a_k, a_l are weights of the kth and l^{th} Gauss point (geometric location of weight), respectively. Generally speaking, it can be shown, that integration is exact for an order $2n-1$ order polynomial using n Gauss points.

Element choice

For the lubrication problem, a simple element as the linear, triangular CST (Constant-Strain Triangle) element. The constant strain refers to the derivative, such that it is able to predict exact behaviour for strain in solid mechanics. In other words it possesses C^0 continuity. A higher-order element could have been used, but have not been found necessary due to the increased complexity involved. Also, details such as grooves will require a fine mesh to resolve the pressure profile, making the linear element sufficient. Finally, the triangular geometry will be easily adaptable to geometries including e.g. circular features as holes.

With the isoparametric formulation the shape functions become very simple, as shown in Equation (6.15) and Figure 6.2.

$$N_1 = 1 - \xi - \eta, \qquad N_2 = \xi, \qquad N_3 = \eta \tag{6.15}$$

For the triangular element (CST), the isoparametric coordinate system is defined as in Figure 6.2 with $\xi, \eta \in [0, 1]$, one single Gauss point in the centroid $(\xi, \eta) = (\frac{1}{3}, \frac{1}{3})$ and the area is only half the Jacobian:

$$A_{tri} = \frac{1}{2} |\det J| \tag{6.16}$$

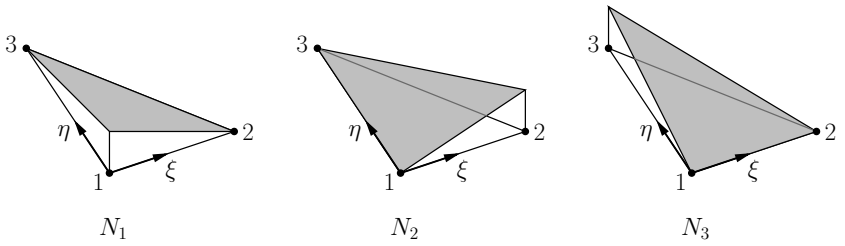

Figure 6.2: Illustration of the three shape functions of Equation (6.15). The linear interpolation within the element is evident.

Final formulation

Updating Equation (6.12) with the numerical integration procedure, the implemented version appears:

$$\bar{\mathbf{K}}^e = -\bar{h}_{cen}^3 \left[\left(\frac{\partial \mathbf{N}}{\partial \theta'} \right)^T \left(\frac{\partial \mathbf{N}}{\partial \theta'} \right) - \left(\frac{\partial \mathbf{N}}{\partial \zeta} \right)^T \left(\frac{\partial \mathbf{N}}{\partial \zeta} \right) \right] \frac{1}{2} |\det J| \tag{6.17a}$$

$$\bar{\mathbf{p}}^e = \{\bar{p}_1, \bar{p}_2, \cdots, \bar{p}_n\}^T \tag{6.17b}$$

$$\bar{\mathbf{u}}^e = -\left(\frac{\partial \mathbf{N}}{\partial \theta'} \right)^T \bar{h}_{cen} \frac{1}{2} |\det J| \tag{6.17c}$$

Here $\bar{h}_{cen}$ indicates the film height evaluated at the centroid of the triangle (the single Gauss point).

Nodal and element numbering

Appendix C contains a short overview of nodal and element numbering. The numbering of the elements is shown in Figure C.1 and is chosen to minimise the bandwidth of the stiffness matrix as demonstrated in Figure C.2. From the figure it is also clear that the matrix is sparse and banded. It should be noted, that no boundary conditions or periodicity are imposed on this particular example.

Boundary conditions

The boundary conditions applied are all Dirichlet boundary conditions, i.e. the direct value is specified: $\bar{p}(\theta, \zeta) = \gamma$, where γ is some value. For this thesis $\gamma = 0$ at boundaries and $\gamma = \bar{p}_{in}$ at inlets. Implementation is done with the '1-0 method'. With the present definition of the angular coordinate θ' starting at maximum film thickness, the implicit periodicity shown for the solutions in

Chapter 4 is ruined. To ensure circumferential periodicity, Lagrange Multipliers are used [34, Ch. 9]. These are used to avoid a singular stiffness matrix.

6.1.1 Flowchart

Please note that the direct problem, i.e. when specifying position and solving for the load carrying capacity, is also covered by Figure 6.3 when omitting the outer loop including the eccentricity update.

6.1.2 Example solutions

Rate of convergence

For demonstrating the rate of convergence, Equation (4.13) is chosen for the direct problem (and with solution given by Equation (4.18)). The 1D solution is obtained by not specifying any boundary conditions for the circumferential boundary nodes, utilising the benefit of the elliptic equation's built-in symmetry. Throughout the thesis, the RMS error is used as a measure of the error:

$$\epsilon_{RMS} = \sqrt{\frac{1}{N}\sum_{i=1}^{N}(\tilde{p} - \bar{p})^2} \tag{6.18}$$

With N being the number of samples, $\sim$ denotes the approximated value and the bar is the exact (non-dimensional) value. The result is shown Figure 6.4. Even though the CST element is first order, Equation (6.19), as explained in [35, p. 21], predicts quadratic convergence for linear shape functions as those of Equation (6.15):

$$\max_{0\leq\theta'\leq 2\pi} |\tilde{p}(\theta') - \bar{p}(\theta')| \leq Ch^2 \tag{6.19}$$

Where C is some constant.

Pressure field and inclusion of boundary conditions

Figure 6.5 shows the pressure distribution of the FE model for the CTR test bearing under a vertical load of 500 N and rotating at 450 RPM. The numbers have been chosen to highlight the pressure boundary at the inlet.

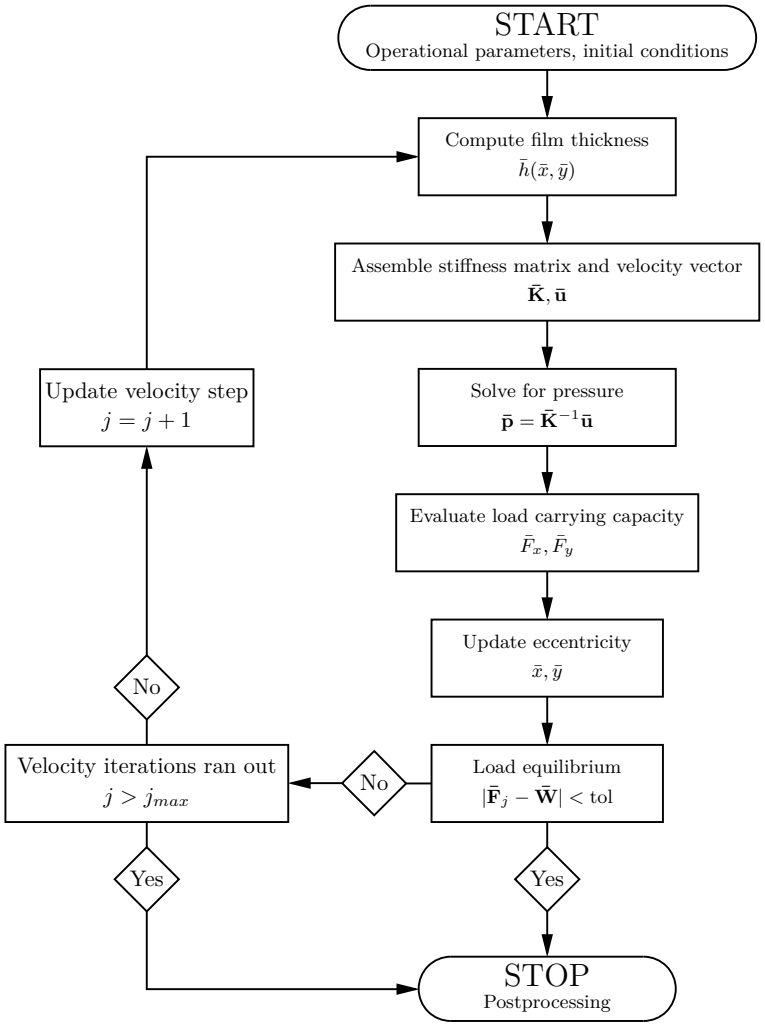

Figure 6.3: Flowchart for the static, indirect problem. The direct problem is solved by passing through the loop directly (keeping $j = 1$).

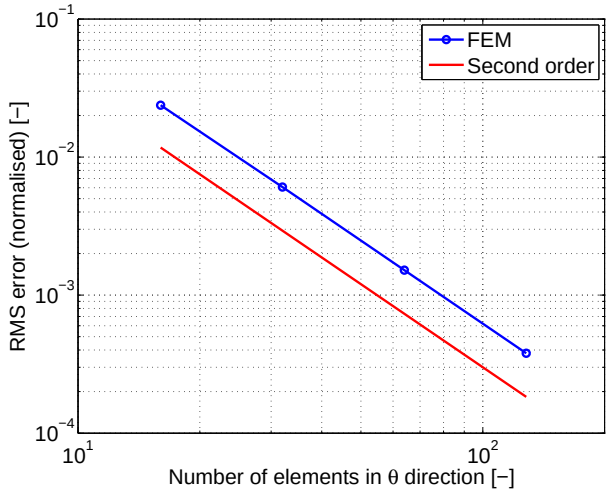

Figure 6.4: Convergence rate of the implemented CST element. The RMS error is normalised with the analytical maximum pressure.

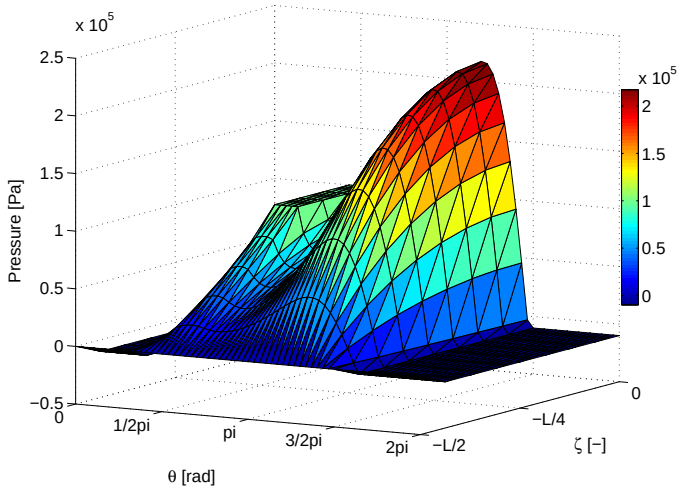

Figure 6.5: Pressure distribution of CTR test bearing under a static, vertical load of 500 N, rotating at 450 RPM. The influence from the inlet is clearly seen.

6.2 Dynamic version

The squeeze term, $\mathrm{d}\bar{h}/\mathrm{d}\bar{t}$, of Equation (3.20) is discretised with the variational approach, see also [36]. Application of the dynamic version of Reynolds equation to the well-known Ruston and Hornsby 6VEB-X Mk III engine data set [37], founded the backbone of Paper [P2].

6.2.1 Functionals

To formulate a finite element equivalent of the perturbed pressure, Equation (5.12), a functional has to be derived for each of the pressure terms, $\bar{p}_i, i = 0, 1, \ldots, 4$.

An expression F is a functional to the considered function g, if insertion of F into the Euler-Lagrange equation yields g. The Euler-Lagrange equation for a single function in two variables is [38]:

$$\frac{\partial F}{\partial g} - \frac{\partial}{\partial x_1}\left(\frac{\partial F}{\partial {}^{\partial g}/_{\partial x_1}}\right) - \frac{\partial}{\partial x_2}\left(\frac{\partial F}{\partial {}^{\partial g}/_{\partial x_2}}\right) = 0 \tag{6.20}$$

Appendix D contains the derivation of the functionals which are:

$$F_0 = -\left(-\frac{\bar{h}_0^3}{2}\left[\left(\frac{\partial \bar{p}_0}{\partial \theta'}\right)^2 + \left(\frac{\partial \bar{p}_0}{\partial \zeta}\right)^2\right] + \bar{h}_0 \frac{\partial \bar{p}_0}{\partial \theta'} + \frac{2\nu}{\omega}\left(\dot{\bar{x}}_0 \sin\theta' - \dot{\bar{y}}_0 \cos\theta'\right)\frac{\partial \bar{p}_0}{\partial \theta'}\right) \tag{6.21a}$$

$$F_1 = -\left(-\frac{\bar{h}_0^3}{2}\left[\left(\frac{\partial \bar{p}_1}{\partial \theta'}\right)^2 + \left(\frac{\partial \bar{p}_1}{\partial \zeta}\right)^2\right] - 3\bar{h}_0^2 \cos\theta'\left(\frac{\partial \bar{p}_1}{\partial \theta'}\frac{\partial \bar{p}_0}{\partial \theta'} + \frac{\partial \bar{p}_1}{\partial \zeta}\frac{\partial \bar{p}_0}{\partial \zeta}\right) + \cos\theta' \frac{\partial \bar{p}_1}{\partial \theta'}\right) \tag{6.21b}$$

$$F_2 = -\left(-\frac{\bar{h}_0^3}{2}\left[\left(\frac{\partial \bar{p}_2}{\partial \theta'}\right)^2 + \left(\frac{\partial \bar{p}_2}{\partial \zeta}\right)^2\right] - 3\bar{h}_0^2 \sin\theta'\left(\frac{\partial \bar{p}_2}{\partial \theta'}\frac{\partial \bar{p}_0}{\partial \theta'} + \frac{\partial \bar{p}_2}{\partial \zeta}\frac{\partial \bar{p}_0}{\partial \zeta}\right) + \sin\theta' \frac{\partial \bar{p}_2}{\partial \theta'}\right) \tag{6.21c}$$

$$F_3 = -\left(-\frac{\bar{h}_0^3}{2}\left[\left(\frac{\partial \bar{p}_3}{\partial \theta'}\right)^2 + \left(\frac{\partial \bar{p}_3}{\partial \zeta}\right)^2\right] + \frac{2\nu}{\omega}\sin\theta' \frac{\partial \bar{p}_3}{\partial \theta'}\right) \tag{6.21d}$$

$$F_4 = -\left(-\frac{\bar{h}_0^3}{2}\left[\left(\frac{\partial \bar{p}_4}{\partial \theta'}\right)^2 + \left(\frac{\partial \bar{p}_4}{\partial \zeta}\right)^2\right] - \frac{2\nu}{\omega}\cos\theta' \frac{\partial \bar{p}_4}{\partial \theta'}\right) \tag{6.21e}$$

6.2.2 Finite element equations

The functionals of Section 6.2.1 should be true for the entire domain Ω:

$$I(\bar{p}_i) = \int_\Omega F_i(\theta, \zeta, \bar{p}_i, {}^{\partial \bar{p}_i}/_{\partial \theta'}, {}^{\partial \bar{p}_i}/_{\partial \zeta})\, \mathrm{d}\Omega, \quad i = 0, 1, \ldots, 4 \tag{6.22}$$

Variational analysis gives that equilibrium, and hence a stable solution, only exists if, [33]:

$$\frac{\partial I(\bar{p}_i)}{\partial \bar{p}_i} = 0, \quad i = 0, 1, \ldots, 4 \tag{6.23}$$

Recall that the distribution of all unknowns within an element are expressed via a polynomial distribution (shape functions) N_j and nodal unknowns n:

$$\bar{p}_{i_{elem}} = \sum_{j=1}^{n} N_j(\theta', \zeta) \bar{p}_{ij} \tag{6.24}$$

Equation (6.23) has to hold for nodal values as well:

$$\frac{\partial I(\bar{p}_i)}{\partial \bar{p}_{ij}} = 0, \quad i = 0, 1, \ldots, 4 \text{ and } j = 1, 2, \ldots, n \tag{6.25}$$

Inserting Equation (6.22) into Equation (6.23) and taking the nodal contributions into account by $\mathbf{N} = [N_1, N_2, \ldots, N_n]$ the finite element equations become (for a single element):

$$\frac{\partial I(\bar{p}_i)}{\partial \bar{p}_i} = -\int_A \left(-\bar{h}_0^3 \left[\left(\frac{\partial \mathbf{N}}{\partial \theta'} \right)^T \left(\frac{\partial \mathbf{N}}{\partial \theta'} \right) + \left(\frac{\partial \mathbf{N}}{\partial \zeta} \right)^T \left(\frac{\partial \mathbf{N}}{\partial \zeta} \right) \right] \mathbf{p}_i + \right.$$
$$\left. \begin{Bmatrix} \left[\bar{h}_0 + \dfrac{2\nu}{\omega} \left(\dot{\bar{x}}_0 \sin\theta' - \dot{\bar{y}}_0 \cos\theta' \right) \right] \dfrac{\partial \mathbf{N}}{\partial \theta'}^T \\ -3\bar{h}_0^2 \cos\theta' \left[\left(\dfrac{\partial \mathbf{N}}{\partial \theta'} \right)^T \left(\dfrac{\partial \mathbf{N}}{\partial \theta'} \right) + \left(\dfrac{\partial \mathbf{N}}{\partial \zeta} \right)^T \left(\dfrac{\partial \mathbf{N}}{\partial \zeta} \right) \right] \mathbf{p}_0 + \cos\theta' \dfrac{\partial \mathbf{N}}{\partial \theta'}^T \\ -3\bar{h}_0^2 \sin\theta' \left[\left(\dfrac{\partial \mathbf{N}}{\partial \theta'} \right)^T \left(\dfrac{\partial \mathbf{N}}{\partial \theta'} \right) + \left(\dfrac{\partial \mathbf{N}}{\partial \zeta} \right)^T \left(\dfrac{\partial \mathbf{N}}{\partial \zeta} \right) \right] \mathbf{p}_0 + \sin\theta' \dfrac{\partial \mathbf{N}}{\partial \theta'}^T \\ \dfrac{2\nu}{\omega} \sin\theta' \dfrac{\partial \mathbf{N}}{\partial \theta'}^T \\ -\dfrac{2\nu}{\omega} \cos\theta' \dfrac{\partial \mathbf{N}}{\partial \theta'}^T \end{Bmatrix} \right) \mathrm{d}A = 0$$
$$, i = 0, 1, \ldots, 4 \tag{6.26}$$

One may notice that the matrix on the left hand side indeed is the same for all five perturbation terms, as stated in connection with Equation (5.12). Also, for a static case ($\dot{\bar{x}}_0 = \dot{\bar{y}}_0 = \bar{p}_i = 0, i = 1, 2, \ldots, 4$), it is seen that Equation (6.26) simplifies to Equation (6.12). The discretisation is completed by redoing Equations (6.13)-(6.16).

6.2.3 Flowchart

Figure 6.6 contains the flowchart for the dynamic solutions. As claimed above, the similarities of the different perturbation pressures are clear also in the programming of their solution. It is indicated by the similar work-flow for the equilibrium pressure $\bar{p}_0$ and the perturbed pressures $\bar{p}_3, \bar{p}_4$.

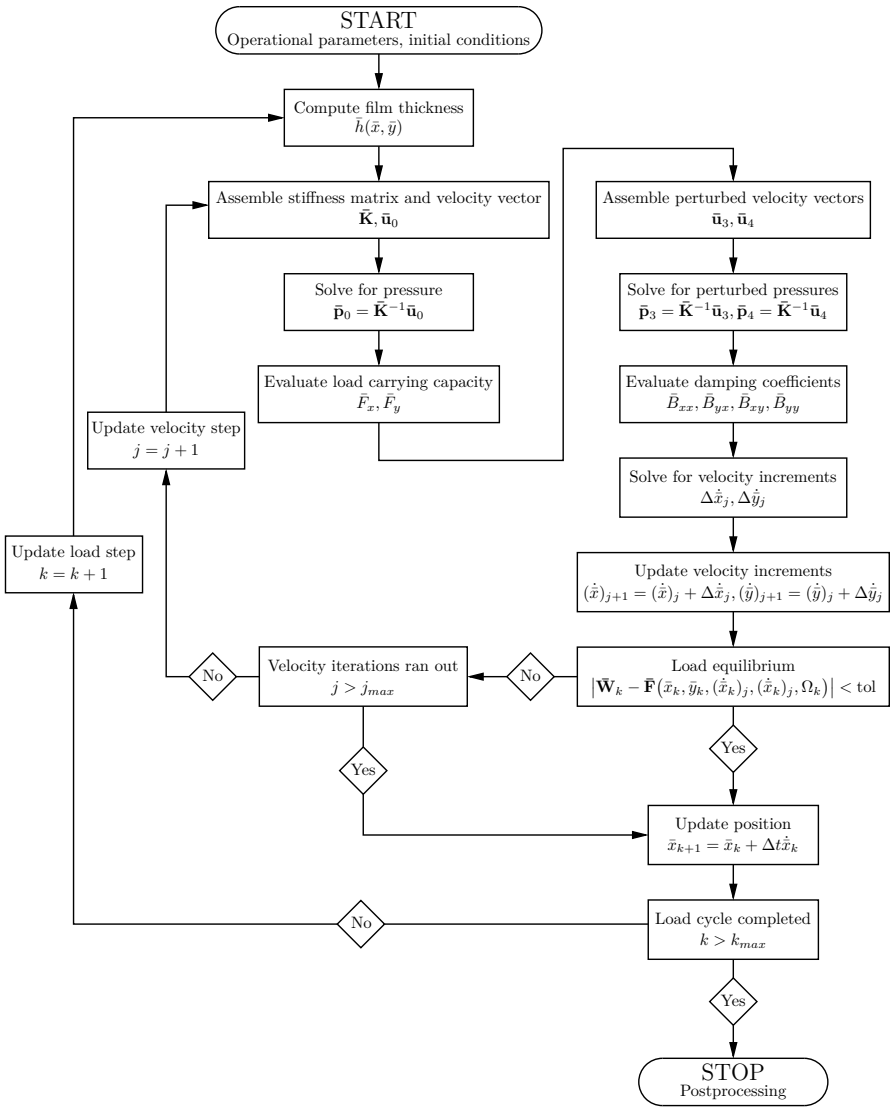

Figure 6.6: Flowchart for the dynamic, indirect problem. Note, that similar to the static case, the direct problem can be seen in the left column. However, it is often not relevant for combustion engines, as displacements are specified through the load (series) and not directly. The similarity between the different right hand sides and corresponding solution procedure is seen by comparing the two columns.

6.2.4 Example solutions

Rotating, constant load

A neat and simple, but effective validation is found in McIvor [23]. For the smooth bearing, i.e. with no grooves or inlets, a load of fixed magnitude will yield the same position, relative to the load orientation, no matter the global orientation of the load. This means that a rotating load of constant magnitude will lead to a circular orbit.

Recall, the right hand side of Equation (3.12) containing the relative velocity of the two bearing surfaces: $(U_1 + U_2)/2$ with $U = \omega R$. For at statically loaded bearing we would expect $\omega_j = \omega, \omega_b = \omega_l = 0$ where the indices j,b and l are journal, bushing and load, respectively. Switching the frame of reference from (the global) bushing reference frame to the journal reference frame, we now have $\omega_j = 0, \omega_b = \omega_l = -\omega$. The relative velocity magnitude has not changed, and hence, the eccentricity will be that of a statically loaded bearing with $\omega_j = \omega$ (while pressure distribution and attitude angle are shifted 180° due to the sign change of the relative velocity).

$$\bar{\mathbf{W}} = \begin{Bmatrix} \bar{W}_x \\ \bar{W}_y \end{Bmatrix} = \begin{Bmatrix} \cos(\omega t) \\ \sin(\omega t) \end{Bmatrix} \bar{W}_0 \tag{6.27}$$

Equation (6.27) with an amplitude of $W_0 = 1000\,\mathrm{N}$ leads to the orbit of Figure 6.7. The convergence to a circular orbit is clear, further indicated by the equidistant positioning of the blue triangles indicating rotational increments of 90°. The slight rotation of the four points relative to the xy axes is due to the hydrodynamic effect, the problem being basically static. The simplicity of the problem makes it good for studying the behaviour, as evaluated parameters will approach either constant values (global properties), e.g. cavitated volume, or alternate with the load (local parameters) like volume flow at $\theta' = 0$. Figure 6.8 is included to demonstrate the relations between the direct damping terms $\bar{B}_{xx}, \bar{B}_{yy}$ and the cross-coupling terms $\bar{B}_{xy}, \bar{B}_{yx}$. First of all, the symmetry of the operator $\bar{B}_{ij} = \bar{B}_{ji} = {}^{\partial \bar{F}_j}/_{\partial \dot{\bar{x}}_i}$. Secondly, the expected shift of $\bar{B}_{yy}$ and $\bar{B}_{xy}$ relative to $\bar{B}_{xx}$ at $-90°$ and $-45°$, respectively. Finally, the rotational shift described in connection with Figure 6.7 can also be noticed by the coefficients having their max/min/zero values shifted the same amount of 9° away from a multiple of 90°.

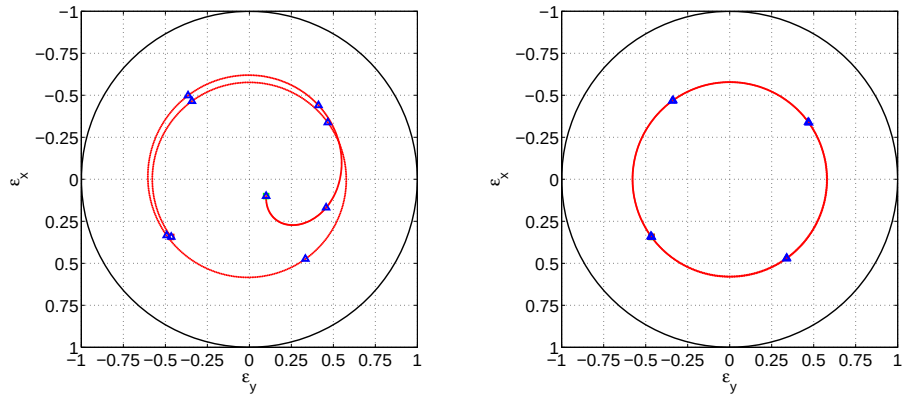

Figure 6.7: Circular orbit for the case of a rotating load. (a) First load cycle. (b) Second load cycle. Blue triangles mark increments of 90° of load rotation or crank angle position.

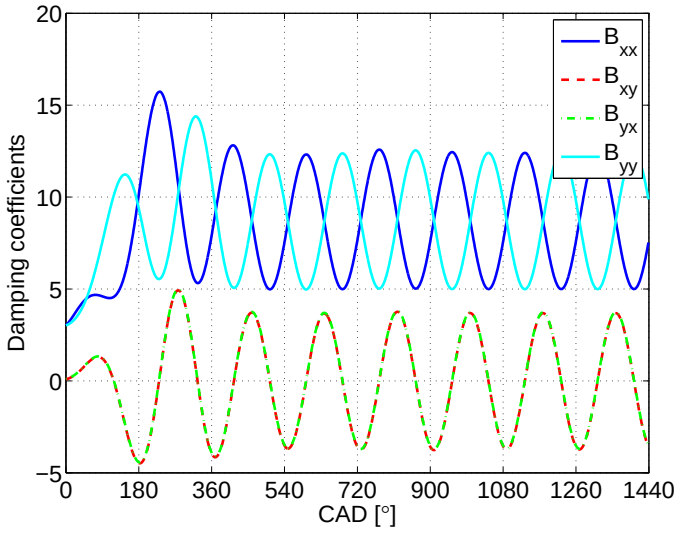

Figure 6.8: Damping coefficients as function of the crank angle position.

Ruston and Hornsby 6VEB-X Mk III engine

As mentioned in the opening lines of this section, the Ruston and Hornsby 6VEB-X Mk III engine has become a benchmark case for code solving the dynamic lubrication problem. Therefore it has been used to test the general dynamic implementation, despite the uni-directional loading capability of the CTR rig, contrary to the bi-directional loading occurring in the Ruston and Hornsby engine, see Figure 6.9. Figure 6.10 contains the comparison of the journal orbit for the Ruston and Hornsby engine data set as given in Campbell et al. [37] and by the present code, see also Paper [P2].

Good agreement is obtained between the two solutions, taking into consideration the different assumptions applied. The direction changes from the three load spikes at the beginning and end of the load cycle, are evident. Being a four-stroke engine, the crank angle degree (CAD) is 720° at the end of the combustion cycle. Labelling the CAD in intervals of 90°, 8 fix points are obtained who also show good agreement.

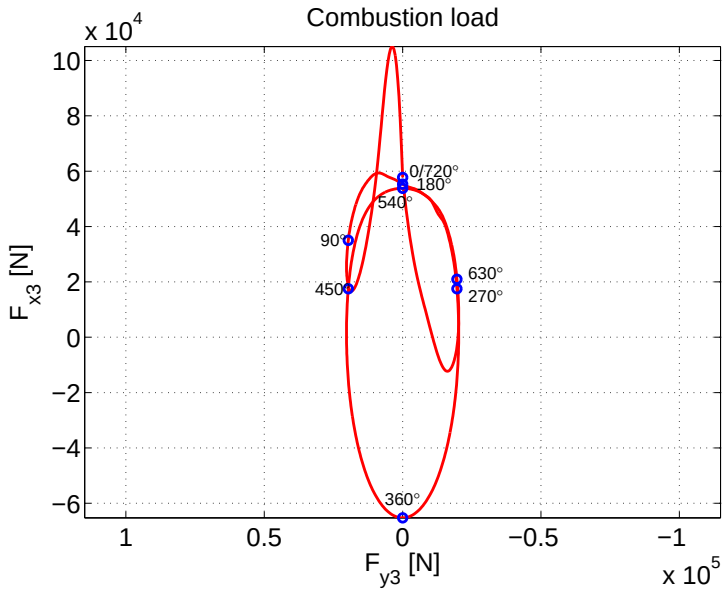

Figure 6.9: Combustion load given in the local coordinate system attached to the connecting rod, see also Figure 2 in Paper [P2].

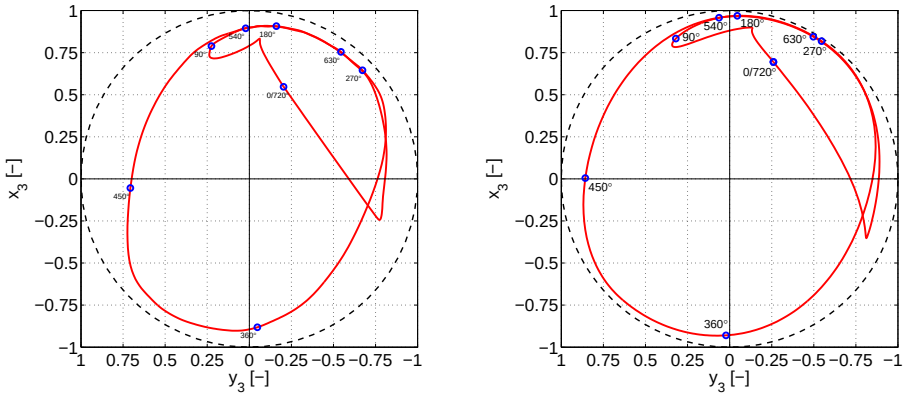

(a) (b)

Figure 6.10: Comparison between (a) The solution of [37] based on the graphical method and the short bearing solution, and (b) The finite element solution of this work.

Chapter 7

Finite volume implementation

This chapter covers the application of a commercial code to solve the lubrication problem. Instead of relying solely on the usual approach of simplifying the Navier-Stokes equations (3D) into the Reynolds equation (2D), solution of the full Navier-Stokes equations have been carried out as part of the project.

One of the most compelling arguments is the desire to investigate the influence from grooves, inlets and other geometrical features that are not correctly modelled with the Reynolds equation.

The finite volume (FV) based commercial software package CD-adapco STAR-CCM+ version 10.02 has been used. Due to the increased amount of grid points compared to the 2D approach, the simulations have been run on 8-64 CPUs on a cluster.

Publication-wise, Paper [P3] uses the same methodology for the FV computations as given here.

7.1 Governing equations

As mentioned above, the commercial code is based on the overall set of equations for a fluid dynamics problem. The Navier-Stokes and continuity equations form the governing relations for a fluid. Assuming no body forces, they take the form:

$$\rho\left(\frac{\partial \mathbf{u}}{\partial t} + \mathbf{u}\cdot\nabla\mathbf{u}\right) = -\nabla p + \nabla\cdot\mathbf{T} \tag{7.1}$$

$$\frac{\partial \rho}{\partial t} + \nabla\cdot(\rho\mathbf{u}) = 0 \tag{7.2}$$

Where ρ is density, $\mathbf{u}$ is the velocity vector, p is pressure, $\mathbf{T}$ is the deviatoric stress tensor ($\mathbf{T} = \nabla\cdot(\mu(\nabla\mathbf{u} + (\nabla\mathbf{u})^T)) + \nabla(-2/3\mu\nabla\cdot\mathbf{u})$ with μ being the dynamic viscosity).

The discretisation of STAR-CCM+ allows for first and second order discretisation for both spatial discretisation (convection term $\mathbf{u} \cdot \nabla \mathbf{u}$) and temporal discretisation (grid fluxes). Both options have been tried out in various combinations, but the first order methods are used as they have performed most stable in terms of sensibility to numerical noise.

7.2 Meshing

The mesh generation has been done with the built-in mesh generator. Here the flexible, unstructured polygon based mesh is chosen with the optional 'thin mesher', allowing for a structured mesh in regions deemed thin. This transition from unstructured to partly structured mesh is shown in Figure 7.1. Along walls, so-called prism layers constituted from thin cells, are used to capture the gradients occurring from the no-slip boundary conditions. Using the default structure of the mesh generator, all parameters are functions of a given base size, enabling easy changes to the set-up. The experiences from the meshing process were the background for Paper [P1].

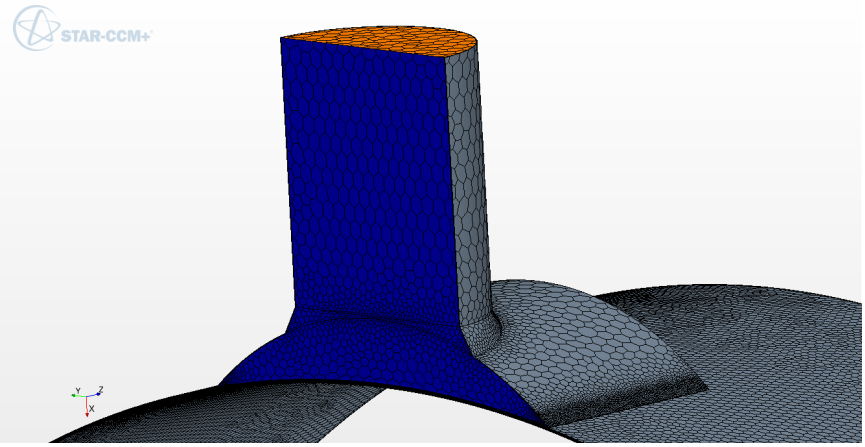

Figure 7.1: Example on meshing. Polyhedral are used throughout the model in an unstructured fashion, besides the thin film region, where the radial direction is structured.

7.3 Dynamic fluid body interaction formulation

To deal with force equilibrium problems in STAR-CCM+ the dynamic fluid body interaction (DFBI) solver has to be applied. It is capable of solving for all 6 degrees of freedom (3 translational and 3 rotational) in an Cartesian coordinate system. The below is a short overview of the equations mentioned in the programme documentation [39, pp. 5323–5334].

The formulation is naturally centred around Newton's second law of motion. The linear (translational) motion is governed by:

$$M \frac{\mathrm{d}\mathbf{v}}{\mathrm{d}t} = \mathbf{F} \tag{7.3}$$

With M being mass, $\mathbf{v}$ is the velocity vector, t is time and $\mathbf{F}$ is the force vector. Equation (7.3) is specified in the global coordinate system. For the rotation, the local coordinate system with origin in the center of mass of the body:

$$\mathbf{M} \frac{\mathrm{d}\boldsymbol{\omega}}{\mathrm{d}t} + \boldsymbol{\omega} \times \mathbf{M}\boldsymbol{\omega} = \mathbf{n} \tag{7.4}$$

Here $\mathbf{M}$ is the tensor storing the moments of inertia, $\boldsymbol{\omega}$ is the vector of angular velocities and $\mathbf{n}$ is the vector of resulting moments. With some manipulation, a relationship between body position given by the coordinate vector $\mathbf{q}$ and the motion laws above is established as:

$$\left(\mathbf{J}^T \bar{\mathbf{M}}\right) \ddot{\mathbf{q}} + \mathbf{J}^T \bar{\mathbf{N}} = \mathbf{J}^T \mathbf{F}^{i,g} \tag{7.5}$$

with $\mathbf{J}$ being the Jacobian matrix, $\bar{\mathbf{M}}$ is constructed from the tensor of inertia moments in the global coordinate system and the Jacobian matrix, $\bar{\mathbf{N}}$ contains expressions for the local contributions and $\mathbf{F}^{i,g}$ is a collection imposed forces and moments, occurring from the fluid flow and those externally imposed.

Equation (7.5) contains the number of degrees of freedom, i.e. 6 minus potential constraints. For the journal bearing, only the translations in the plane, normal to the axial direction of the journal, remain (x, y). The rotational degree of freedom around the z axis is not to be catered for, as the rotational motion is prescribed as a boundary condition.

7.3.1 Morphing

In order to avoid distortions in the generated mesh, when performing the displacements prescribed by the DFBI solver, a built-in morphing algorithm continuously update the grid point positions. Various parameters for minimum cell quality and size are defined to ensure abandoning of the simulation, if those are reached.

7.3.2 Ramping

To improve the stability of the DFBI scheme, a ramping function is used to linearly increase the weight of the imposed forces and moments from 0 to 1. Before the ramping starts, a release time is defined. Until this time is reached, the solution is static (in terms of force and moment equilibria!), such that a flow field has time to be developed. The ramp duration is recommended to be in the order of 10 times the release time.

7.4 Time stepping

Aiming for numerical stability a desired Courant number CFL $= U\Delta t/\Delta x$ is specified as CFL $= 1$. This is further stabilised by limiting the allowable time step to the interval $t \in [1 \times 10^{-6}\,\mathrm{s}, 5 \times 10^{-5}\,\mathrm{s}]$ together with an averaging between the calculated (new) step and the current one, $t_{new} = \alpha t_{old} + (1-\alpha)t_{new}$. The time range is chosen to limit the Courant number to CFL ≈ 1 for the grid sizes and expected velocities during the simulation, and the averaging weight used is $\alpha = 0.5$.

The time step during the DFBI ramp is further limited by ramping up the CFL value from 0.5 to 1. This was done to remove some oscillations in the calculated load, when the DFBI solver 'sees' more and more of the imposed load, but still do not have enough weight from the ramp to balance the it.

7.5 Example solution

Similar to the FE verification, Equations (4.13) and (4.18) is used to verify the application of the Navier-Stokes equations. Due to the various criteria for the built-in mesh generator to ensure a high quality mesh, a large number of cells are distributed in the circumferential and axial directions (say 1000), together with a limited number in the radial direction (say 2-20). This motivated a small investigation of three ways to refine the mesh: varying the base size which also works on the prism layers[1]; varying base size, but fixing the prism layers at a level corresponding to the variable case of 7.5×10^{-4} m base size[2]; and fixing base size, but varying the number of cells in radial direction (thin mesher layers)[3].

Good, overall agreement with the analytical solution is obtained for all three cases, but the convergence rates behaves very differently. The error is

[1] Base size: (5 to 15) $\times 10^{-4}$ m in steps of 2.5×10^{-4} m, prism layer thickness 0.3% base size, 10 thin mesher layers

[2] Base size: (5 to 15) $\times 10^{-4}$ m in steps of 2.5×10^{-4} m, prism layer thickness 2.5×10^{-6} m, 10 thin mesher layers

[3] Base size: 15×10^{-4} m, no prism layers, $4, 6, \ldots, 16$ thin mesher layers

practically constant for what is effectively axial and circumferential refinement. On the other hand, the 3D nature of the equations is clearly visible, meaning that despite the 2D nature of Reynolds equation, a certain amount of resolution is still needed for the FV code. This convergence is consistent with Schmidt, Stücke, and Nobis [40], who in connection with their work, being both theoretical and experimental, find that 14-20 layers are needed.

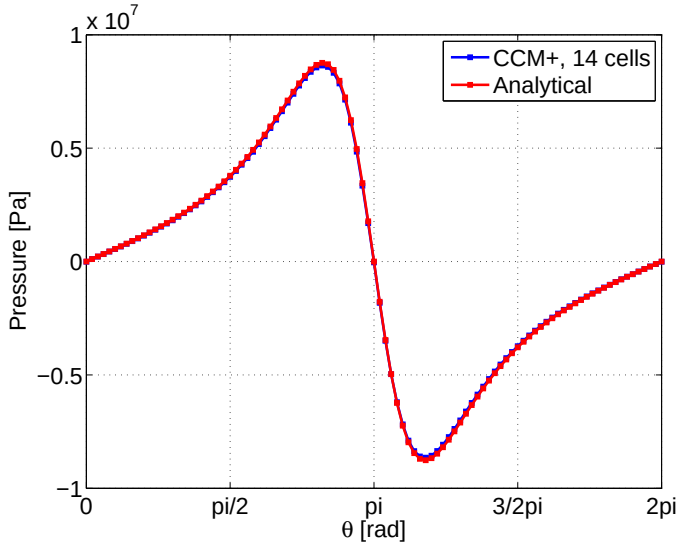

(a)

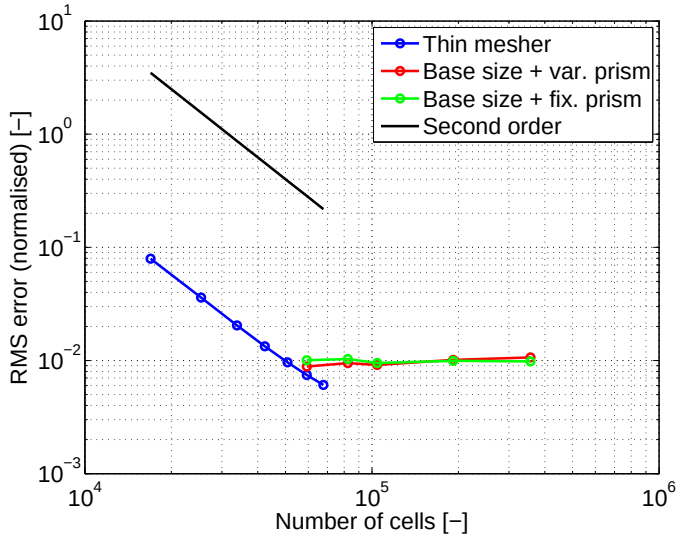

(b)

Figure 7.2: Solution of the long bearing assumption. (a) FV solution with 14 thin mesher layers. (b) Convergence rate of the three cases. The RMS error is normalised with the analytical maximum pressure.

Chapter 8

Cavitation test rig

The experimental part of this project is founded in the setup named the cavitation test rig (CTR). Contrary to other test rigs from various authors, e.g. Shawki and Freeman [18], Carl [19], the purpose here is two-fold. Whereas the mentioned works are made on test rigs designed for monitoring journal orbit and pressure profiles, this particular rig also aims at visualising film rupture and reformation, besides orbit measurements.

8.1 Test rig overview

In Figure 8.1 the test rig is shown with indication of the main elements. The test rig journal bearing consists of two main component groups. Firstly, the test bearing (5) mounted in the bearing stays (6). Secondly, the journal (7) is supported with a set of spherical roller bearings (3) and driven by an AC motor (8) with speed monitoring through a tachometer (2). The support bearings are mounted on a hinged table plane (1) to allow for the correct movement of the journal within the test bearing. Loading of the bearing is done through a hydraulic set-up (10) and monitored by a load cell (9) and the corresponding displacements are measured with two sets of proximity probes (4).

For the main component, the test bearing, dimensions are chosen as $D = 100\,\text{mm}$, $L = 50\,\text{mm}$ and $C = 100 \times 10^{-3}\,\text{mm}$. With the chosen dimensions $L/D = 1/2$, making the short bearing solution an acceptable approximation. The clearance C is chosen two times the rule of thumb given in Chapter 2, for improving the wedge effect and hence promote cavitation. The overall dimensions and material thickness are chosen for optimising the stiffness, such that the dominating displacement will be that of the journal.

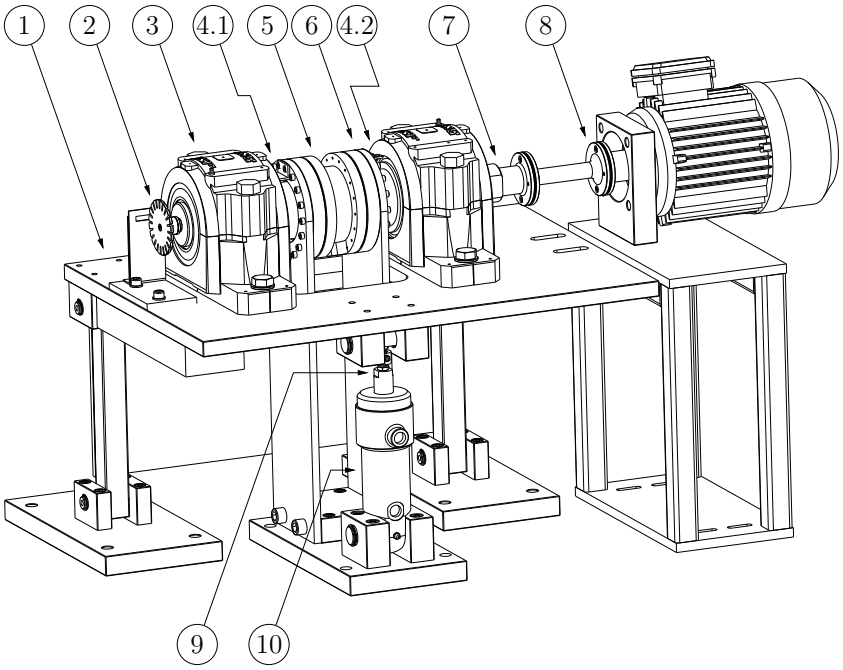

Figure 8.1: The cavitation test rig (CTR). Key components: 1) mounting table, 2) tachometer, 3) support bearing, 4) two sets of proximity probes, 5) test bearing, 6) bearing stay, 7) shaft (journal), 8) membrane clutch and AC motor, 9) load cell, and 10) hydraulic cylinder.

The electric motor is a 3-phase AC motor at 3 kW ran via a frequency converter enabling operation between 300 RPM and 3000 RPM.

Besides the tachometer; a pressure sensor and thermocouple in the inlet to the bearing, plus thermocouples at the two boundaries of the bearing monitor the respective parameters, see Figure 8.2. Two thermocouples at the bearing outlet drains are chosen, as any misalignment may be indicated in non-uniform temperatures.

8.1.1 Data acquisition

The data acquisition (DAQ) is done through LabVIEW and load imposition is done with the sister program Measurement & Automation Explorer (MAX). A LabVIEW program forms the user interface of the test rig, plotting real time values of the sensors:

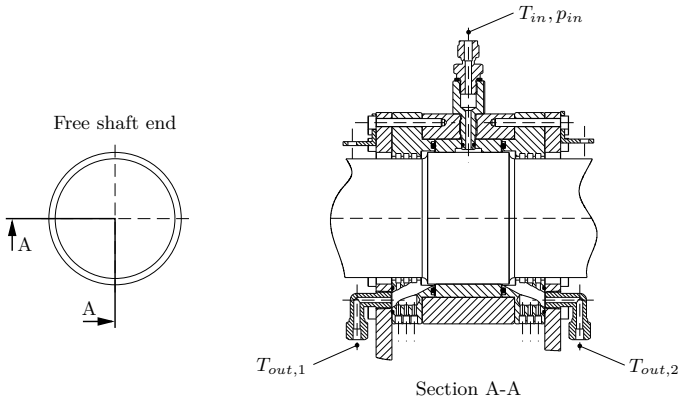

Figure 8.2: Illustration of the oil in- and outlets, lying in two different planes. Measurement points for temperature and pressure is also specified.

- Two sets of proximity probes
- Load cell
- Three temperature sensors, see Figure 8.2
- Two pressure transducers (bearing inlet and supply pressure for hydraulics)
- Tachometer

The above quantities are logged with a frequency of 2 kHz for on-screen display, but most importantly, written to a CSV file for post-processing.

8.1.2 Load control

Two load types can be applied to the test bearing: a constant load and sinusoidal load, with positive and negative magnitudes for both types. The adjustment is done by a servo valve, controlling the flow going above and below the piston of the hydraulic cylinder.

8.2 Test rig design

8.2.1 Design considerations

In the following paragraphs, a number of features of the CTR are highlighted.

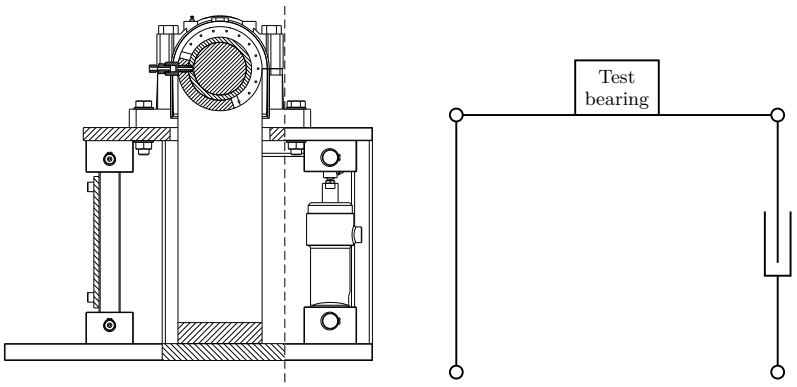

(a) Bearing located within test rig. (b) Mechanism layout.

Figure 8.3: Illustration of bearing mounted in test rig. (a) Orientation of the cylindrical coordinate system exploiting the symmetry. (b) Resulting mechanical model.

Degrees of freedom

To allow the journal to move freely within the test bearing sleeve, 2 degrees of freedom (DOF) are needed. This can be verified from [41, p. 271]:

$$n^{(\mathrm{DOF})} = n^{(\mathrm{bodies})} \times 3 - \sum_{\mathrm{joints}} n^{(\mathrm{constraints,\ 2D})} \tag{8.1}$$

From Figure 8.3 it is seen that the rig is constituted from 4 revolute joints and 1 translational joint. Equation (8.1) yields:

$$\begin{aligned} n^{(\mathrm{DOF})} &= 4 \times 3 - (\overbrace{4 \times 2}^{\text{rev. } (x,y)} + \overbrace{1 \times 2}^{\text{trans. } (x,z)}) \\ &= \underline{\underline{2\,\mathrm{DOF}}} \text{ (1 rotational + 1 translational)} \end{aligned} \tag{8.2}$$

Transparent bearing

To visualise the cavitation forming the test bearing is made from a polymer, contrary to a normal bearing material, such as steel with a top layer of a softer substance like white metal. To support the weaker polymer and supply protection against excessive deformation from the hydrodynamic film forces, the test bearing is caged in a steel sleeve, as seen from Figures 8.1 and 8.2.

Figure 8.4: Acrylic test bearing. Shown is the circumferential groove, mounted in the test rig is the point groove design, but otherwise they are similar. Technical drawings are shown in Appendix E.

For the CTR, the bearing material used is the acrylic PMMA, widely known as PLEXIGLAS®. Being a polymer and hence basically oil-based, there was a suspicion that the test bearing would swell over time, as the material is known to react with organic solvents and other chemicals. Submerging a block of PMMA with dimensions $51.35\,\mathrm{mm} \times 31.60\,\mathrm{mm} \times 24.13\,\mathrm{mm}$ in a bath of SAE-30 for 5 months, showed no increase in any of the dimensions down to 1/100 mm on any of the three sides. The coefficient of thermal expansion is $\alpha_{PMMA} = 126 \times 10^{-6}\,\mathrm{K}^{-1}$ and hence ten times that of steel ($\alpha_{steel} = 12 \times 10^{-6}\,\mathrm{K}^{-1}$) [42, pp. A17–A19]. The surrounding steel sleeve will expand outwards when heated, but only one tenth of the polymer expansion. This will led to a constraint on the polymer, expanding inwards with the remaining nine tenth. A temperature increase of the test bearing-steel sleeve pair will thus lead to a net decrease of bearing diameter. With the inclusion of the journal, the decrease may be even more significant. However, the thermal conductivity of steel versus that of PMMA, may justify the perception of the journal as a heat sink ($\kappa_{PMMA} = 0.21\,\mathrm{W/(m\,K)}$ vs. $\kappa_{steel} = 51.9\,\mathrm{W/(m\,K)}$) [42, pp. A21–A23].

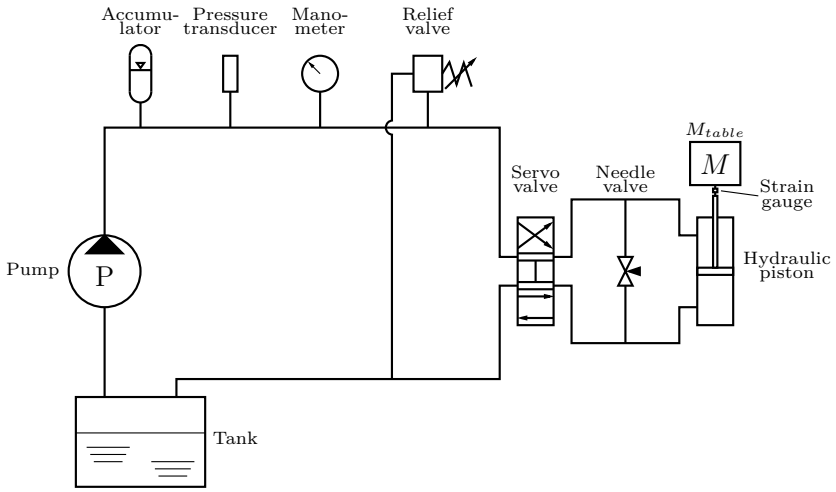

Figure 8.5: Loading arrangement including hydraulic power-pack and supply system.

Using a new tolerance specification ($\varnothing 100\text{B}7 = \varnothing 100^{255}_{220}$), the actual clearance is taken as the mean, $C = 118.75 \times 10^{-3}$ mm.

Loading system

Several principles were available for the loading arrangement. One could think of spring, hydraulic, and magnetic loading, just to mention a few. Whereas the older papers (Shawki and Freeman, 1955 [18], Carl, 1963 [19]) both rely on a spring-based system loaded with eccentric cams and Jacobson and Hamrock, 1983 [20] used a slightly different eccentric device, a hydraulic system has been favoured here. The purely mechanical system is capable of generating the load over a wide range of frequencies, due to being driven by an electric motor. On the other hand, it is limited by the mutual relationships of the dimensions for the various links in the system, requiring adjustment for every new load case. Those disadvantages are avoided by utilising a more flexible set-up, like the servo-controlled hydraulic cylinder applied to the CTR. Also, a hydraulic cylinder is capable of delivering loading at a frequency and magnitude that can resemble those of a combustion engine. Very high frequencies may be an issue for the supply system, but tweaking the set-up to cope with high/low flow cases will improve such issues. The supply system consists of a hydraulic power-pack, an accumulator, a safety valve, a servo valve and a bypass valve and is seen in Figure 8.5.

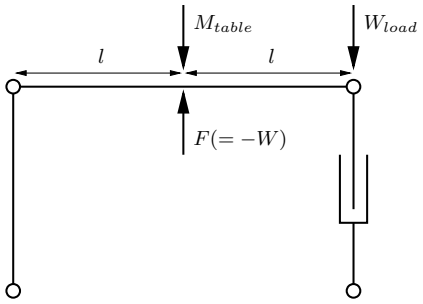

Figure 8.6: Load balance of CTR.

The servo valve is a proportional valve, such that their exists a linear relationship between the control current and the load measured at the load cell. It is a standard component and hence following the industry standard of I being in the interval 4 mA-20 mA. This means that 12 mA is the 'zero' and currents above and below will yields negative (upwards) and positive (downwards) loads, respectively.

The design of the rig means that the test bearing is preloaded with the mass of the mounting table, M_{table}, see also Figures 8.3(a) and 8.6. The mounting table mass is given in Equation (8.4). Exploiting the symmetry of the design, it is easily found that the magnitude registered by the load cell, W_{load}, is one-half that of the bearing load carrying capacity (plus the preload!), such that:

$$F = -W = 2W_{load} + M_{table} \tag{8.3}$$

$$M_{table} = M_{Mount.\,table} + M_{Journal} + M_{Counterweight} + M_{Supp.\,bearings} = 174.7\,\text{kg} \approx \underline{\underline{1714\,\text{N}}} \tag{8.4}$$

Proximity probes

The displacement of the journal is monitored with two sets of proximity probes, a set on each side of the test bearing. The positioning is seen in Figure 8.7. Like the temperature monitoring, a perfectly aligned journal would give identical measurements. To cancel out any contributions from bearing play the probes are mounted on the bearing stays. The probes are of the inductive type (Eddy currents) to be immune to contamination from e.g. oil leakage, where a thin film would influence infrared probes.

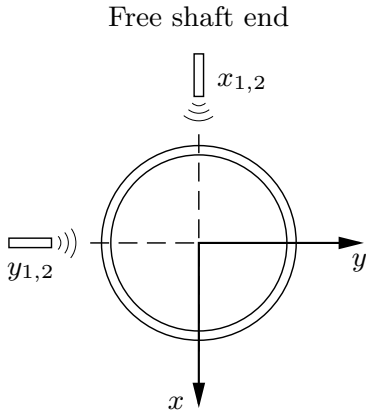

Figure 8.7: Positioning of the proximity probes.

Table 8.1: Properties for SAE-30 lubricant.

Parameter	Value	Unit
Density, ρ	885	$\mathrm{kg/m^3}$
Dynamic viscosity, μ	0.071[a]	Pa s
Saturation pressure, p_{sat}	90 000[b]	Pa
Speed of sound, v_s	1300	m/s

[a] At 40 °C.
[b] Estimated.

Lubricant

In line with the combustion engine related use, a standard lubricant has been chosen. The choice has been in favour of the SAE-30, being rather cheap and readily available. The standard operating temperature for the CTR has been estimated to 40 °C, so the dynamic viscosity is $0.071\,\mathrm{Pa \cdot s}$ [29, p. 98]. A complete list of properties is given in Table 8.1.

Sommerfeld number

With the dimensions of the CTR used in Equation (4.5), a typical Sommerfeld number for the CTR will be:

$$\begin{aligned} S_{\text{CTR}} &= \frac{\mu N D L}{W}\left(\frac{R}{C}\right)^2 \\ &= \frac{0.071\,\text{Pa}\cdot\text{s}\times 10\,\text{s}^{-1}\times 0.1\,\text{m}\times 0.05\,\text{m}}{1500\,\text{N}}\left(\frac{0.05\,\text{m}}{100\times 10^{-6}\,\text{m}}\right)^2 \\ &= \underline{\underline{0.592}} \end{aligned} \tag{8.5}$$

8.3 Experimental setup

To compliment the above description, the laboratory set-up of the CTR is presented in Figures 8.8 and 8.9 on the following pages.

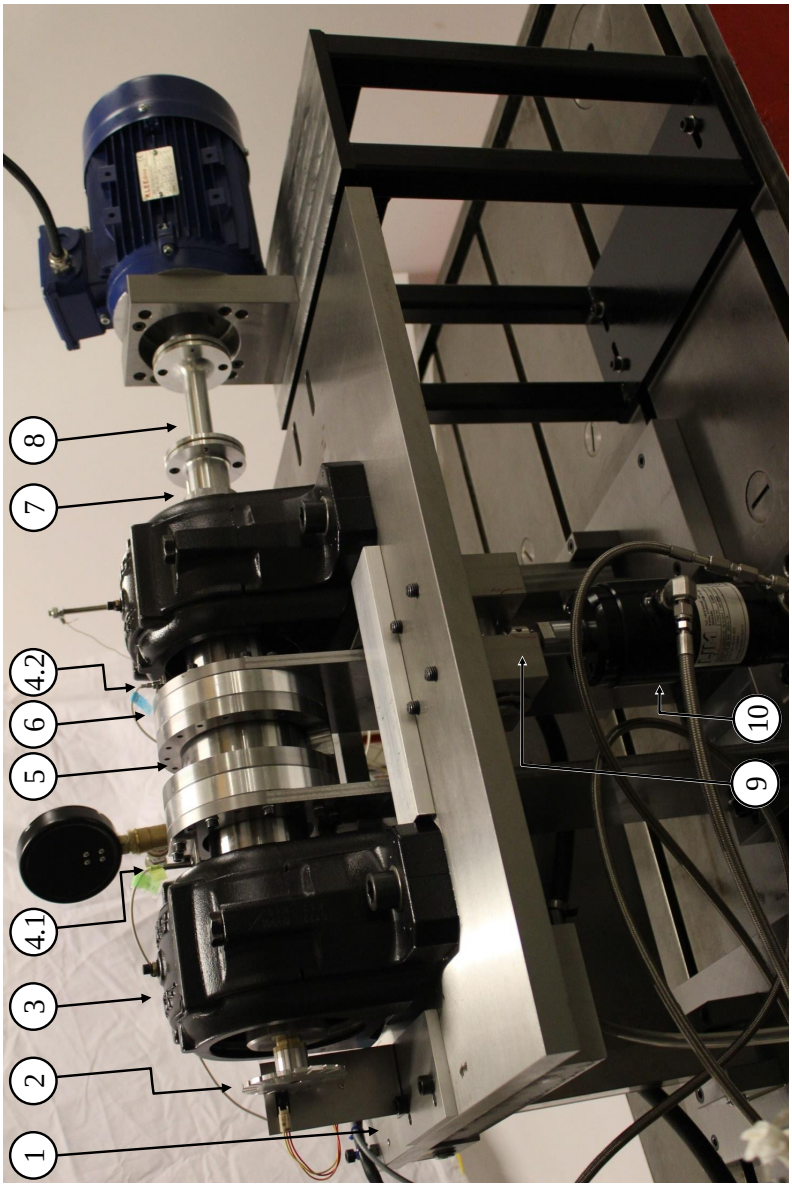

Figure 8.8: Cavitation test rig in laboratory, compare to Figure 8.1. Key components: 1) mounting table, 2) tachometer, 3) support bearing, 4) two sets of proximity probes, 5) test bearing, 6) bearing stay, 7) shaft (journal), 8) membrane clutch and AC motor, 9) load cell, and 10) hydraulic cylinder.

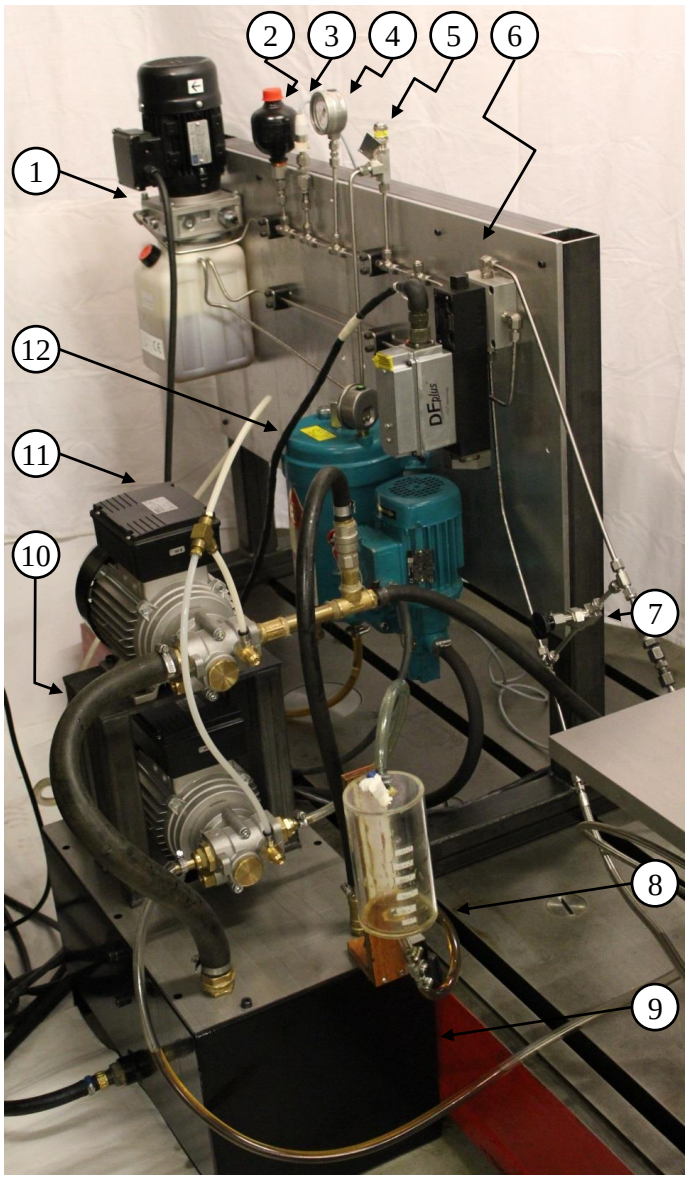

Figure 8.9: Power-pack for hydraulic loading along with lubricant supply system. The power-pack (items 1–7) can be compared to Figure 8.5. Key components: 1) hydraulic supply pump, 2) accumulator, 3) pressure transducer, 4) manometer, 5) relief valve, 6) servo valve, 7) needle valve, 8) lubricant flow meter, 9) lubricant tank, 10) lubricant suction pump, 11) lubricant supply pump, and 12) lubricant filtering unit.

Chapter 9

Numerical results

The two numerical methods (FE and FV) have been applied to the CTR test bearing. A case study has been performed on the two groove designs: point groove (Case 1) and circumferential groove (Case 2), see Figure 9.1 or the technical drawings of Appendix E. Besides the convergence study performed in Chapter 7, Case 1 is divided into three subsets (Case 1.1-3) to perform a convergence study. The results of this case study is also motivating Paper [P3].

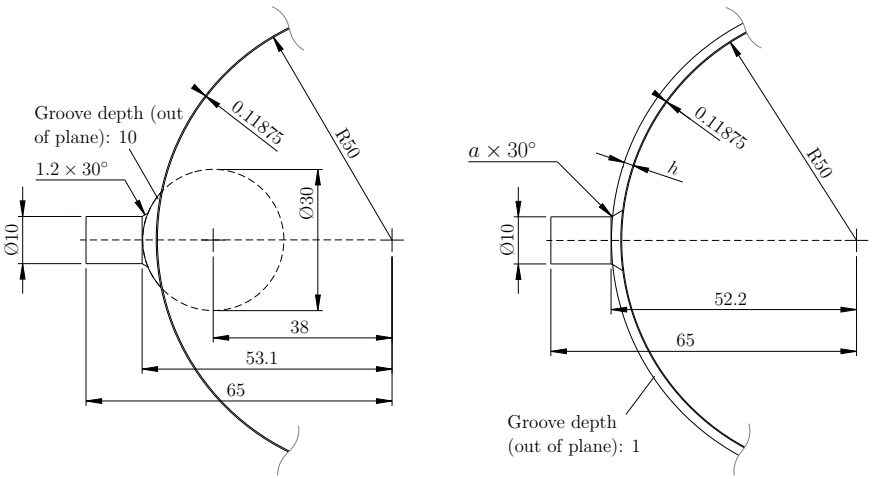

Figure 9.1: The two bearing geometries: (a) Specification of point groove (Case 1). (b) Specification of circumferential groove with the variable groove height (Case 2).

One of the advantages of solving the full Navier-Stokes equations, namely the modelling of geometries outside the assumptions applied for Reynolds equation, is exploited. The manufactured bearing has a groove cross section of $W \times H = 2\,\text{mm} \times 2\,\text{mm}$. To investigate the influence on the groove height, especially when it approaches the magnitude of the film thickness, the simulations have been ran for three set-ups of H ($H = \{2, 0.5, 0.1\}\,\text{mm}$), named Case 2.1-3.

Directly comparable is the prediction of orbit and frictional losses, but for further processing the two methods split as seen below.

9.1 Solution set-up

The test bearing is modelled as shown in Figure 9.2. Imposed on the bearing is the dynamic loading given by Equation (9.1) and the physical time of the simulation is 0.4 s allowing for two periods of the fluctuating load, see also Figure 9.3. The bearing is considered to be infinitely stiff. On purpose the bearing is positioned at a small eccentricity ($\varepsilon_x = \varepsilon_y = 0.1$) to illustrate the implementation of force balance, by introducing a discrepancy between initial position and initial, imposed load. Table 9.1 contains a summery of the relevant parameters applied.

$$W_x(t) = \frac{1}{2}\left[\sin\left(10\pi \cdot t - \frac{\pi}{2}\right) + 1\right] \cdot 3 \times 10^3\,\text{N} \tag{9.1}$$

The convergence is investigated where the FE part is meshed with 8×30, 16×60 and 24×90 elements, respectively. Following the experiences from Chapter 7, the amount of thin mesher layers (in radial direction) are 6, 10 and 14, respectively, and a base size of $15 \times 10^{-4}\,\text{m}$ for the FV part.

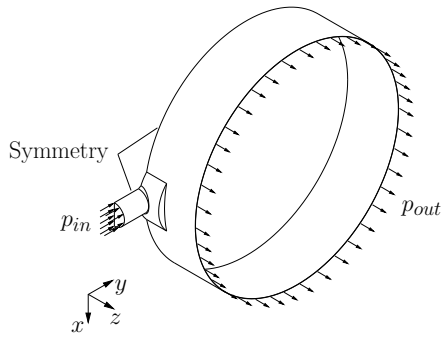

Figure 9.2: Specification of boundary conditions, here shown for the Case 1, but apply to Case 2 as well. Pressure magnitudes are listed in Table 9.1.

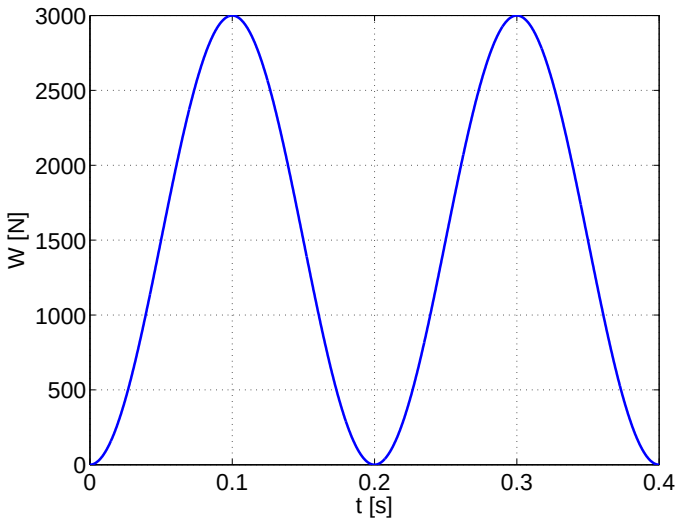

Figure 9.3: The imposed load of Equation (9.1). With the chosen 600 RPM, the time span corresponds to four journal revolutions or 1440 CAD.

Table 9.1: Dimensional and operational parameters for the journal bearing applied in the FV code (and FE code where applicable). For lubricant parameters, cf. Table 8.1.

Parameter	Symbol	Value	Unit
Length	L	50	mm
Diameter	D	100	mm
Clearance (radial)	C	118.75	µm
Mass moment of inertia	I_{zz}	2×10^{-3}	$\mathrm{kg\,m^2}$
Rotational speed	ω	600	RPM
Load (vertical)	W_x	$W_x(t)$[a]	N
Inlet pressure	p_{in}	2×10^5	Pa
Outlet pressure	p_{out}	1×10^5	Pa

[a] See Equation (9.1).

9.1.1 Solutions

The solutions are obtained in very different time ranges. Whereas the FE solution for the one and a half load cycle shown below is computed on a normal office computer in the order of 30 minutes on 1 CPU, the FV solutions have a total CPU time of 30 121 hours.

Pressure distribution

The pressure distribution of the four groove designs are shown in Figure 9.4 after one and a half load cycle ($t = 0.3\,\mathrm{s}$). Despite the differences in groove design, the pressure distributions are very similar. Most interesting is the fact that due to the load having its maximum value at this point, even the tallest of the circumferential grooves are experiencing high pressure and thus contributing to the load carrying capacity unlike the initial expectations.

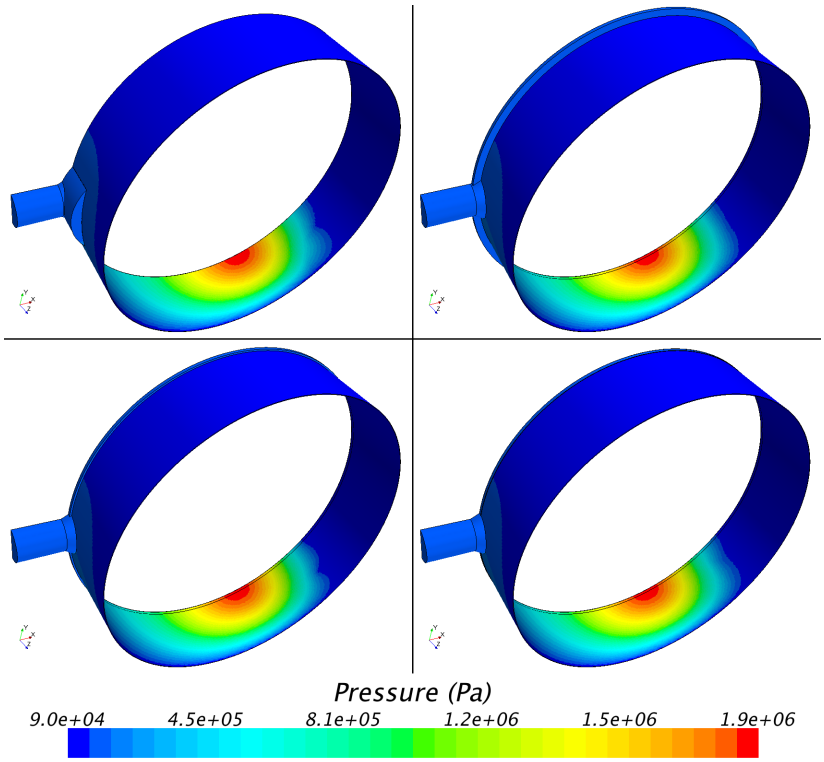

Figure 9.4: Pressure distribution of the four different groove designs; top row is Case 1.3 and Case 2.1 and bottom row is Case 2.2 and Case 2.3. Time $t = 0.3\,\mathrm{s}$ (maximum value of imposed load).

Journal orbit

The journal orbits for Case 1 and Case 2 are shown in Figures 9.5 and 9.6, repsectively. In terms of convergence studies, Figure 9.5 shows very subtle differences between the medium and fine mesh solutions represented by the red (medium) and green (fine) lines, whereas the coarse mesh represented in blue is slightly off. Also, the two discretisation methods predict very similar orbits, both in terms of magnitude and orbit shape.

Based on the convergence of the orbit prediction, the medium case of 10 radial layers are used for the varying groove height of Case 2 in the FV discretisation. With the modelling of groove extent by assuming a uniform, practically hydrostatic, pressure boundary condition in the FE discretisation, the three values of groove height are not 'seen' by the FE discretisation. The

consequences of the simplified approach to model the groove is clearly seen in Figure 9.6(a). The general shape of the orbit is the same, but the position and magnitude of the orbit has moved relative to the initial position $\varepsilon_x = \varepsilon_y = 0.1$. As those results are very different from the previous findings, an axial refinement has been introduced to make sure only nodes being coincident with the groove position are included in the pressure boundary. However, it is clear from Figure 9.6(a) that the effect of the refinement is very little.

With the same overall settings to the mesh, the variable groove height orbit is predicted in Figure 9.6(b). The orbit is very much identical to the mesh-wise corresponding Case 1.2 in Figure 9.5(b). Both this behaviour as well as the general pressure distributions of Figure 9.4 indicates that the grooves possess some load carrying capacity, irrespective of their height. For both cases, the initial discrepancy described previously results in an upwards movement of the journal, until load equilibrium is met.

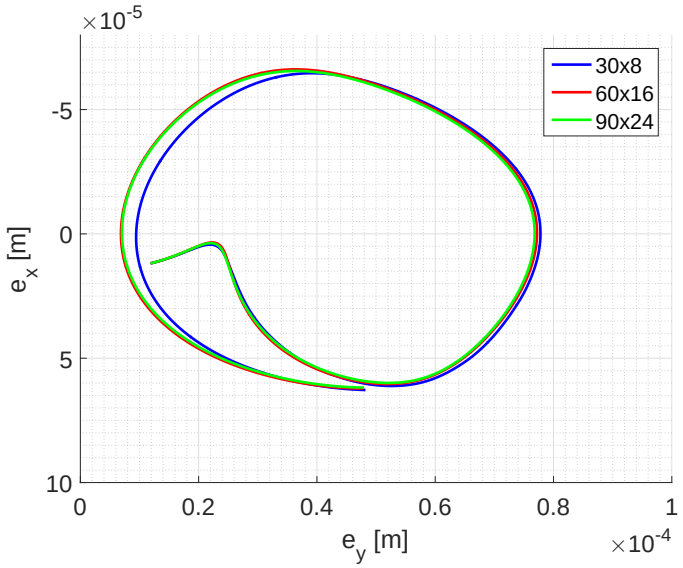

(a)

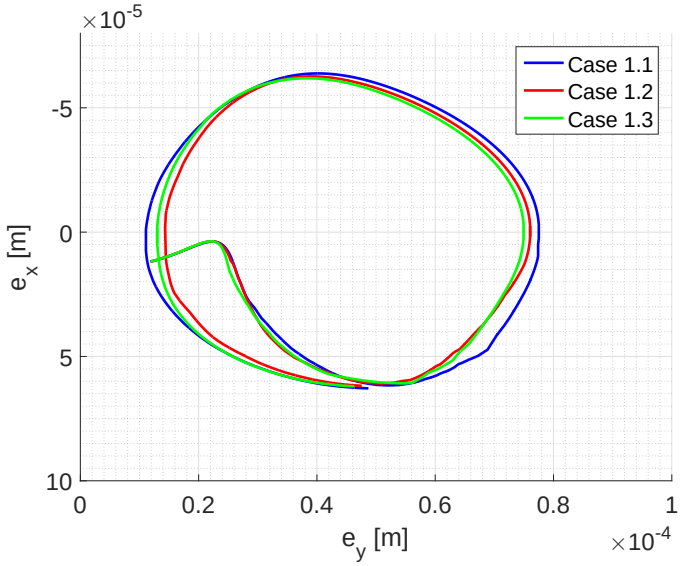

(b)

Figure 9.5: Journal orbit of point groove: (a) FE solution. (b) FV solution.

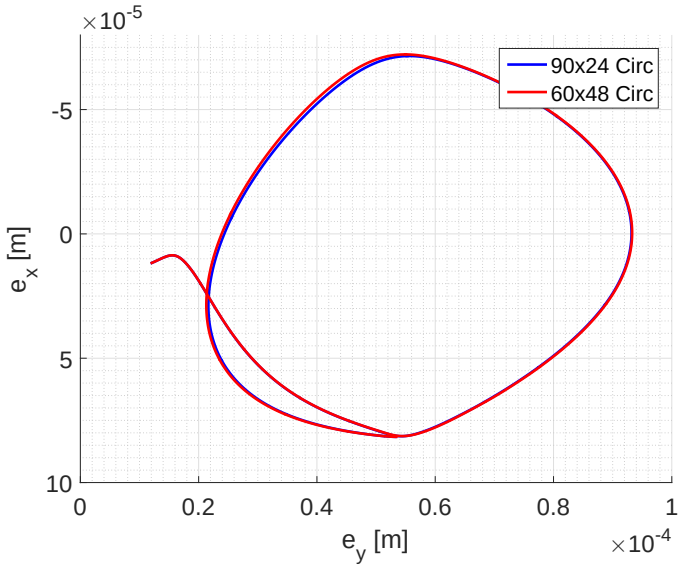

(a)

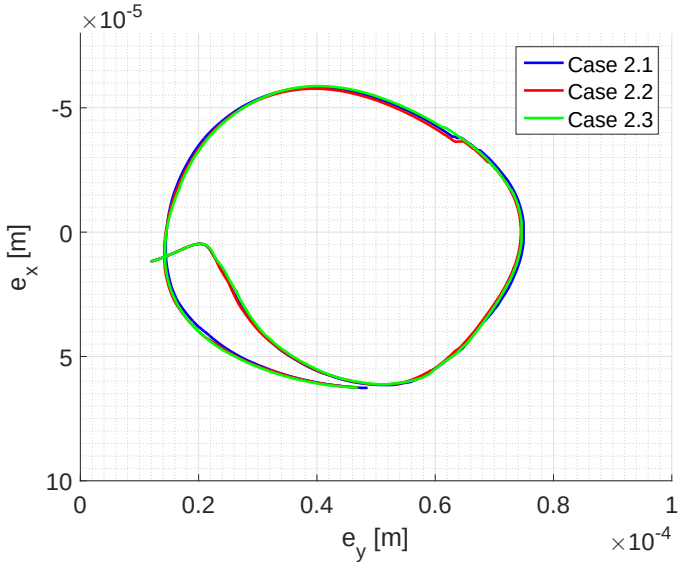

(b)

Figure 9.6: Journal orbit of circumferential groove: (a) FE solution. (b) FV solution.

Friction loss

To quantify the suitability of the proposed bearing designs, friction loss is an obvious parameter. For the overall friction loss per revolution, the average frictional moment is used. Here being approximated with the trapezoidal rule:

$$\bar{M_f} = \frac{1}{\Delta t}\int_{t_1}^{t_2} M_f(t)\,\mathrm{d}t \simeq \frac{1}{\Delta t}\sum_{i=1}^{N-1}\frac{M_f(i)+M_f(i+1)}{2}\big(t(i+1)-t(i)\big) \quad (9.2)$$

Where $\Delta t = t_2 - t_1$ and N is number of samples. This is performed using the MATLAB command `trapz`. Being readily available in the FV code, Equation (4.10) yields the FE values. Contrary to the bar notation of Equation (4.10) the left hand side of Equation (9.2) obviously refers to the averaged value of the dimensional frictional moment.

With the similar appearance of the various pressure distributions and journal orbits, only small deviations in the frictional moments are expected. Recall that Equation (4.10) relies on the film thichness $\bar{h}$ and pressure gradient $\partial\bar{p}/\partial\theta$. Hence, only a characteristic set of data are plotted in Figure 9.7. The trend of the four cases are similar, but it is clear the deviation is caused in the first half of the intervals with increasing load and reaching its maximum very close to the midpoint of the interval. With the load curve being a sinusoidal function, this relates to areas with accelerating load increase (positive time derivative) cf. Figure 9.3. Similarily, the second half of the interval with a decelerating load increment minimises the discrepancy and brings it to a low level for the entire interval of decreasing load. During the next load increase, the pattern repeats. Equation (9.2) yields for the first one and a half load cycle; Case 1: $\bar{M}_{f,FE} = -1.811\,\mathrm{Nm}$ and $\bar{M}_{f,FV} = -1.706\,\mathrm{Nm}$ and Case 2: $\bar{M}_{f,FE} = -2.187\,\mathrm{Nm}$, $\bar{M}_{f,2.1} = -1.713\,\mathrm{Nm}$, $\bar{M}_{f,2.2} = -1.706\,\mathrm{Nm}$, $\bar{M}_{f,2.3} = -1.708\,\mathrm{Nm}$.

Though similarities are to be expected from the orbits and pressure distributions, some conclusions can be drawn. Assuming the full 3D solution represented by the FV scheme to be the most correct approximation, the friction loss is overestimated by 6% for Case 1 and 28% for Case 2 by the FE discretisation. With reference to the above results, the fine grid has resolved the problem sufficiently, such that the difference is more related to the choice of 2D (Reynolds equation) versus 3D (Navier-Stokes equations). Within Case 2 with the varying groove height, there is practically no difference ($< 0.5\%$) of the three heights. Interestingly, the point groove generates virtually the same friction loss.

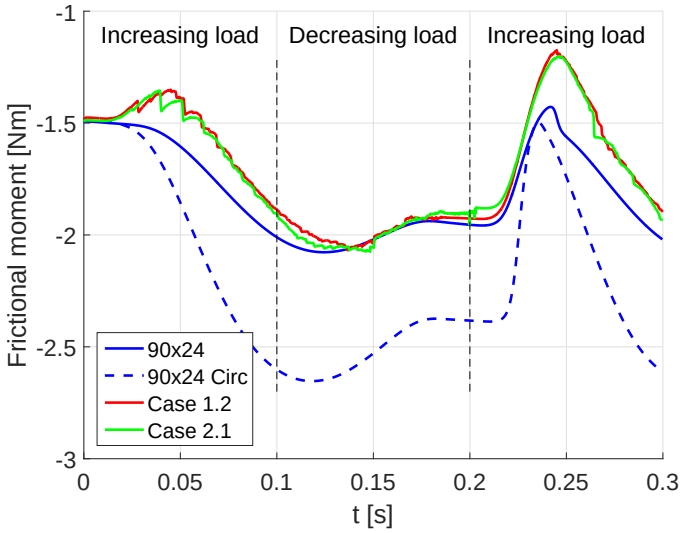

Figure 9.7: Frictional moment for the FE and FV discretisations.

Mass flow

With the assumptions of the half-Sommerfeld solution mass conservation cannot be expected. This is verified by comparing the in- and outlets in Figures 9.8 and 9.9(a), respectively. Being only mildly compressible, compression is not likely, such that mass balance over the in- and outlet should be obtained at all times. This is also the case for the first hundreds of a second until the imposed load has increased to a value where the squeeze effect and pressure modification become dominant.

In Figure 9.8 it is interesting to note the very similar behaviour from the three circumferential grooves of Case 2, but also that they are approximately 60% of the point groove of Case 1. This invites to a further investigation. On page 85 a paragraph is designated to any differences in the flow field, taking advantage of the increased level of detail for the FE simulation.

For the axial and circumferential flow, a comparison between the FE and FV codes are possible. In Figure 9.9(a) acceptable agreement exists between the FE and FV codes. The trends of the two discretisation schemes are equal. The situation appears to be similar for the circumferential flow (Figure 9.9(b)), but this includes a spurious FV solution. To create the shown plot, the FV solutions (red and green line) have been multiplied with a factor of 10^3. From Figure 9.4 it is clear that at the top of the bearing (negative x direction in Figure 9.2) the pressure gradient is very small, if not equal to zero. Hence, the

flow is a pure Couette flow which is velocity driven. This makes it very easy to estimate the mass flow rate as $\dot{M} = {}^1\!/_2 UA\rho \approx 8.3 \times 10^{-3}\,\mathrm{kg/s}$, see also second term of Equation (3.9). For this estimate the clearance C is used, yielding an average flow rate, but still in good agreement with the FE solution. With a physically justified flow matching the FE solution, it is appropriate to assume the FV solution based on extrapolated values onto a cross sectional plane is erroneous.

Please note, the plots in Figures 9.9(a) and 9.8 have been limited, cutting off the violent spikes (3-5 times the adjacent values) occurring very close to $t = 0.2\,\mathrm{s}$ for Case 2. Recall from Figure 9.3 that $W_x(t = 0.2\,\mathrm{s}) = 0$, such that the fluctuations are believed to be stability problems.

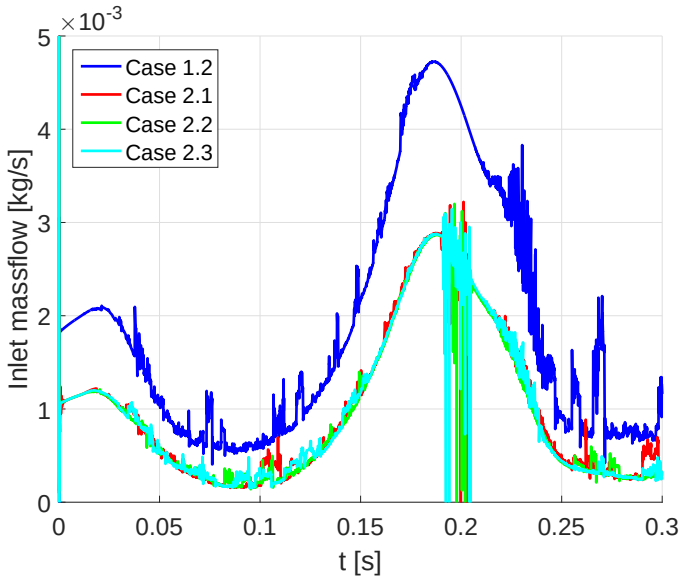

Figure 9.8: Mass flow at the inlet for the FV case.

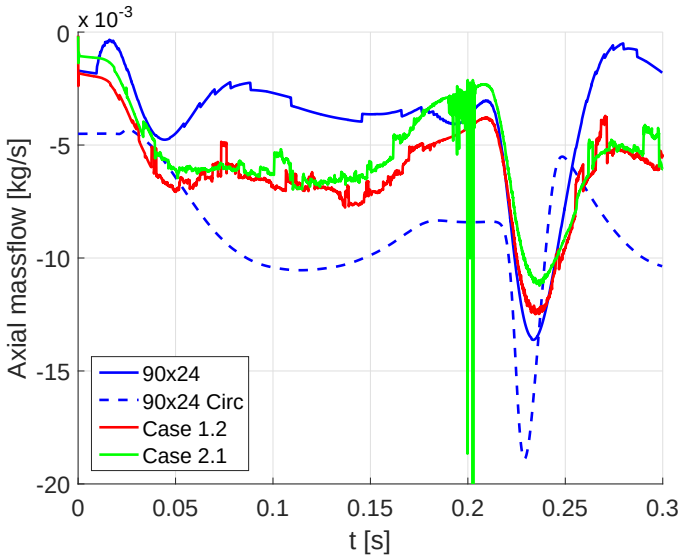

(a)

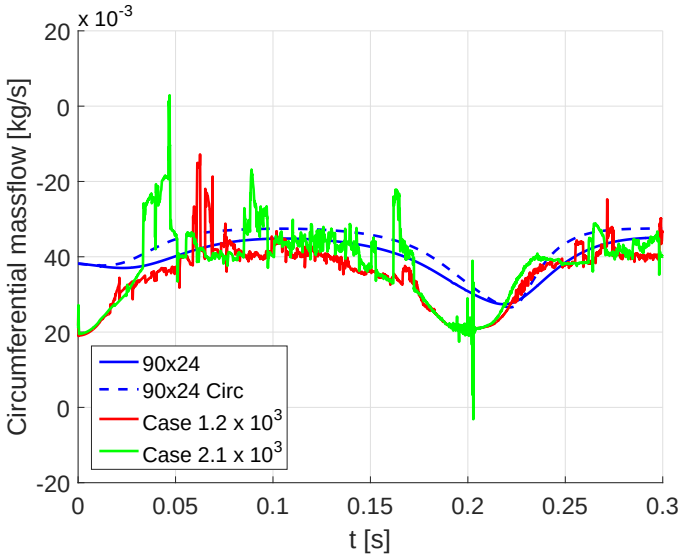

(b)

Figure 9.9: Mass flow for: (a) Outlet (leakage). (b) Circumferential direction.

Cavitated volume

A cavitation map, relating the crank angle, cavitation extent and possibly load orientation, is a good help in visualising the cavitation problem. Such maps are also shown in the review paper of Martin, 1983 [43] as wells as in Paper [P2]. The map shown in Figure 9.10 is made from the FE solution on the fine mesh of 90×24 elements. In this case the load orientation is trivial, but the variation of the cavitated area, both in terms of extent and angular position is interesting. The low load areas around 0/720 CAD leads to a low level of cavitation, whereas the maximum load at 360 CAD results in a cavitation extent of almost 180°. The squeeze term $\mathrm{d}\bar{h}/\,\mathrm{d}\bar{t}$ distorts the map such that the cavitation extent is not symmetric in time; this is, around 360 CAD.

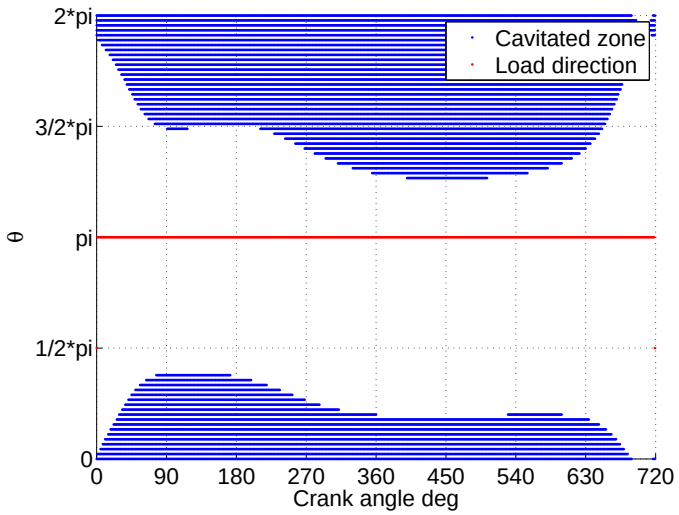

Figure 9.10: Cavitation map for the FE solution with the fine mesh of 90×24 elements. The second load cycle is chosen to portrait a converged solution.

Flow field

To account for the differences in inlet mass flow between Case 1 and 2, as seen in Figure 9.8, the flow field is investigated. Recall that Case 1 at all times features approximately 50% larger mass flow.

Figure 9.11 illustrates the velocity fields of the two cases in the symmetry plane. Contrary to an ordinary vector plot, the so-called line integral convolution technique is used here. This allows for a simple representation of the velocity

field at the expense of flow directions. For this set-up this has not been found to be an issue, but supporting vector plots have been made.

Analysing Case 1 in Figure 9.11(a) it is clearly seen that one major vortex is formed at the top of the groove, just after the inlet pipe. Its clockwise rotation helps the inlet flow mixing with that of the rotational flow attached to the journal. This is also seen from the thin film section where the journal surface velocity driving the system is extending into the groove.

On the other hand, Case 2 in Figure 9.11(b) reveals three vortices located at the left, center and right parts of the groove. The extent of the journal velocity into the groove is also less distinct, with areas of very slow moving lubricant. From the flow field, the discrepancy in mass flow at the inlet seems very plausible.

Summary

Numerical solutions have been applied to find the orbit of a dynamically loaded journal bearing. Solution have been found using both a FE and a FV code, enabling a comparison of the two. Utilising a 2D approach (Reynolds equation) the FE code is much faster than the FV code. However, agreement is only good for the very simple case, just like details regarding the flow is omitted.

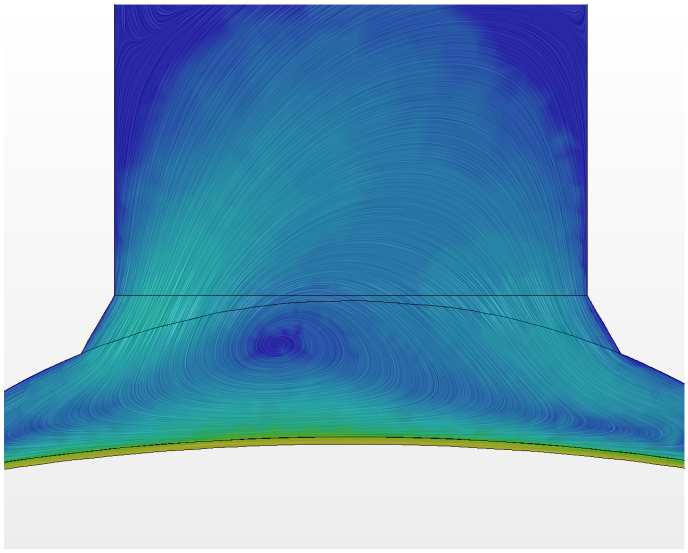

(a)

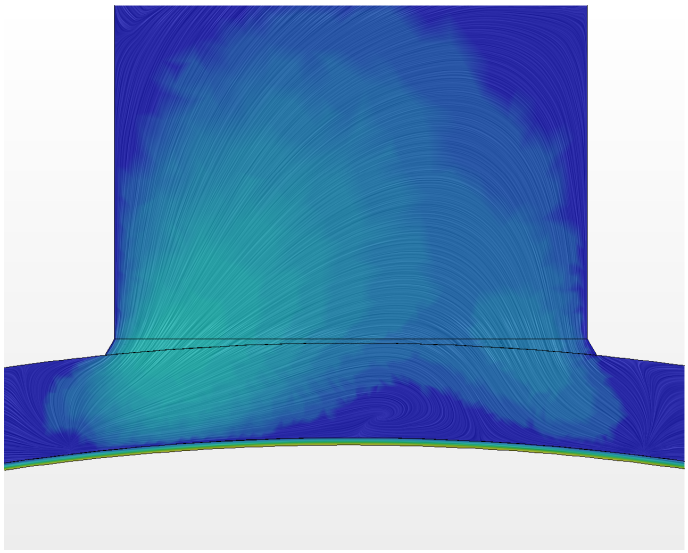

(b)

Figure 9.11: Velocity field in the symmetry plane at $t = 0.075\,\mathrm{s}$ for the two bearing geometries: (a) Point groove (Case 1). (b) Circumferential groove (Case 2.1). Main journal rotation is CCW. Colour represents velocity magnitude with blue $= 0\,\mathrm{m/s}$ and khaki $= 3.14\,\mathrm{m/s}$.

Chapter 10

Experimental results

As demonstrated in Section 1.2, several works have been published over the years, when it comes to experimental investigation of the journal bearing's performance. With the two-fold purpose of the CTR, the experimental results are split up in two sections: journal orbit measurements and cavitation patterns.

10.1 Journal orbit

10.1.1 Clearance measurements

The diametral clearance is estimated by imposing a specific load downwards, measure the position and repeating the process for an upward load. From the idea that the journal will sink to the bottom of the bearing due to is preload, M_{table}, a load of $\pm M_{table} = \pm 1714\,\mathrm{N}$ is used in the study of thermal dependence.

Thermal dependence

With the test bearing being made from a polymer, the dependence from temperature have to be examined. A test is conducted by applying a constant current to the servo valve, operate the rig for a given interval of time, stop the rig and perform measurements as described above. The temperature is logged while the rig is running to avoid air locks influencing the measurements.

Figure 10.1 shows the development of temperature and clearance as a function of time. Here, a clear relationship between the operational duration and both clearance and temperature is evident. A radial contraction of 15 µm from 17 °C is not matching the assumptions of Section 8.2.1 very well, as they predict a clearance reduction of around 70 µm. The sole largest source to the discrepancy is believed to be the temperature dependence of the modulus of elasticity for PMMA, as the melting temperature is $T_{melt} = 105\,^{\circ}\mathrm{C}$ [42,

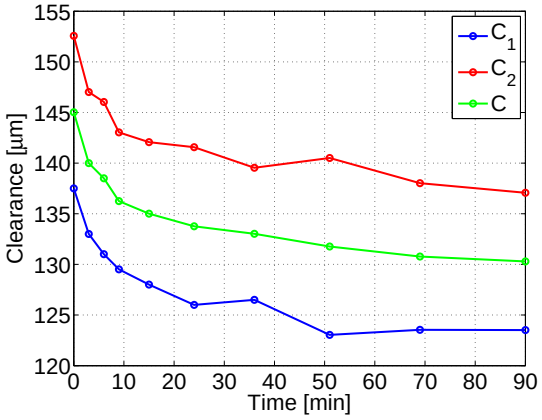

(a)

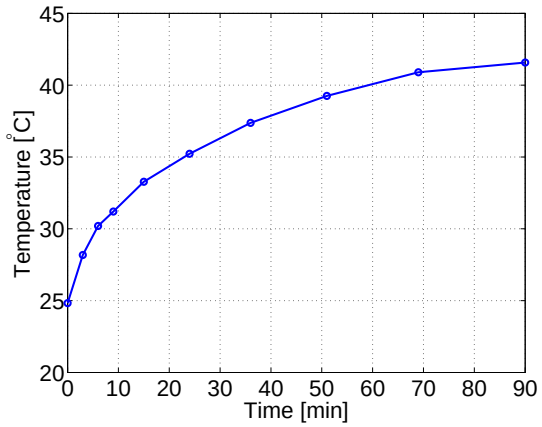

(b)

Figure 10.1: Influence from running time on (a) clearance, and (b) temperature. Between measurements, the servo valve is receiving 11.85 mA which corresponds to approx. 2000 N on the bearing with the journal rotating at 450 RPM.

pp. A41]. The observed radial clearance of $C = 130\,\mu\text{m}$ from Figure 10.1 is used throughout this chapter.

10.1.2 Static loading

In the case of static loading, the orbit is trivial as it will be a single point. However, if the load is varied incrementally, from $W = 0$ to some load $W = W_{max}$ under a steady rotational speed of the journal, (a part of) the locus curve of the bearing is found. Figure 10.2 shows the locus curve of the CTR and a comparison with the FE model computed from the logged values of bearing load. The logged positions lie on a circle-like path as expected, but the coordinates are shifted outwards, and for the largest loads, also downwards. The latter can be explained from the magnitude being 5000 N, introducing elastic deformation of the soft test bearing. For very low loads it is seen how the inlet dominates the pressure field and lifts the journal, according to the FE model, see also Figure 6.5. A reason for not seeing the lift in the experimental results can be back-flow of the lubricant, something that has been witnessed during operation of the rig.

The shift in the y direction might be due to calibration difficulties in that direction. With the unidirectional loading, top and bottom positions are easily found, but those two points possess no difference in y coordinate, of course. Hence, with no hydrodynamic force to assist in moving the journal away from the vertical center plane, significant displacements are difficult to create.

10.1.3 Dynamic loading

With only unidirectional loading, a typical benchmark like the response to the Hornsby engine's combustion cycle, used in Section 6.2.4, is not possible. Instead, a range of load patterns presented by Shawki and Freeman, 1955 [18] and Carl, 1963 [19] is used.

Consider a journal bearing rotating at an angular velocity of ω. Let it be exposed to a sinusoidal load as specified in Equation (10.1), see also Figure 10.3.

$$P = P_0 + P_1 \sin(\omega_1 t) \tag{10.1}$$

The following definitions are now made to characterise the loading:

$$\sigma = \frac{\omega_1}{\omega} \tag{10.2a}$$

$$\tau = \frac{P_1}{P_0} \tag{10.2b}$$

The dynamics of the loading is governed by σ. A value of $\sigma = 0$ indicates a static load, $\sigma < 1$ is a loading frequency lower than the rotational frequency of the journal, values of $\sigma > 1$, i.e. a loading frequency larger than rotational frequency, are unlikely.

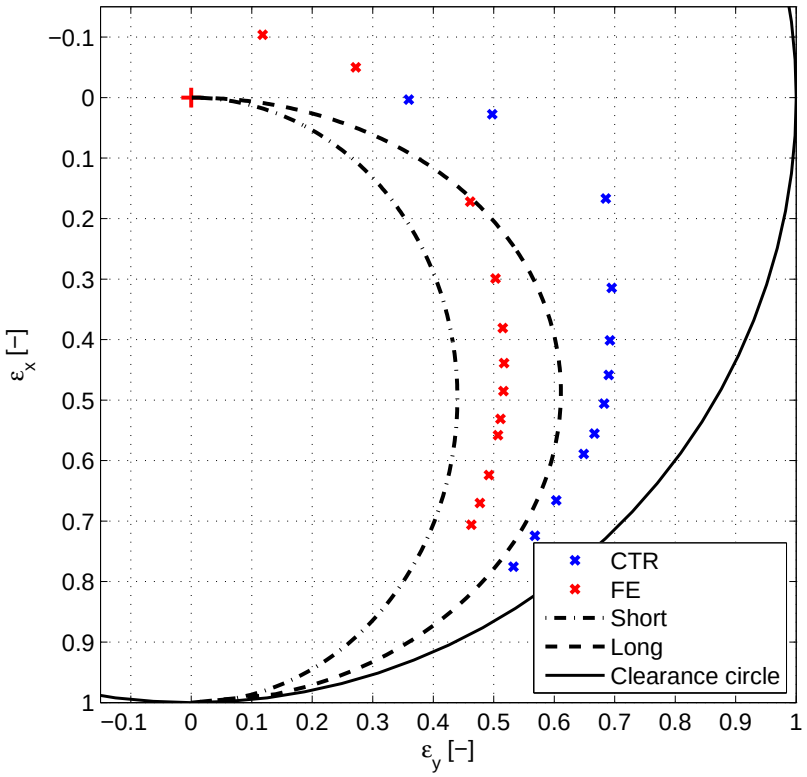

Figure 10.2: Locus curve of the CTR.

The load type is described by τ, with the extremes $\tau = 0$ indicating only static loading and $\tau = \infty$ leading to an alternating load. Finally, $\tau = 1$ changes the alternating load into a fluctuating one. Intermediate cases, like the dashed-dotted ($\tau = 1.33$) and dotted ($\tau = 0.6$) lines of Figure 10.3 will in the limit behave like the true cases ($\tau \to \infty$) and ($\tau \to 0$).

Shawki and Freeman [18] also use the non-dimensional quantity Δ relating the operational parameters of the bearing. The attentive reader will recognise Δ as the inverse Sommerfeld number of Equation (4.5).

$$\Delta = \frac{P\delta^2}{\lambda N} = \frac{\frac{W}{LD}\left(\frac{C}{R}\right)^2}{\mu N} = S^{-1} \tag{10.3}$$

Representative (several values are used) values from [18] and [19] are $S_{\text{Shawki}} = 0.345$

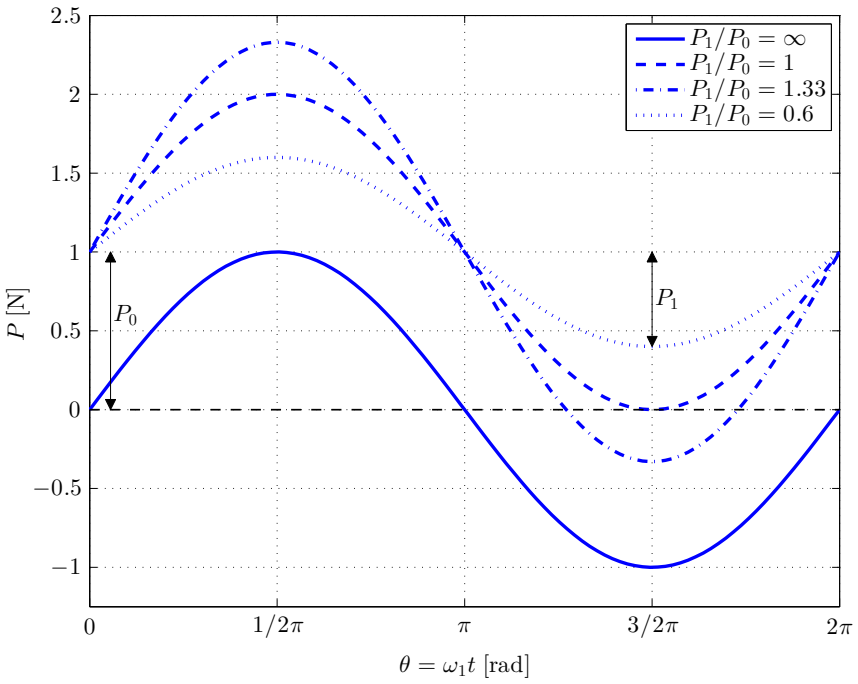

Figure 10.3: The sinusoidal load of the form $P = P_0 + P_1 \sin(\omega_1 t)$, here portrayed for purely alternating load (solid line) and fluctuating load (dashed line). Intermediate cases are shown for alternating load (dashed-dotted line) and fluctuating load (dotted line). The static case of $P_1 = P_1/P_0 = 0$ is omitted.

and $S_{\text{Carl}} = 0.039$, respectively. Hence, the results are obtained on setups relatively similar to the CTR, with Equation (8.5) yielding $S_{\text{CTR}} = 0.592$.

With the difference in loading mechanisms, it has not been possible to replicate the exact results of [18, 19]. Clear trends and similarities are found, however.

Case example

To draw comparisons with the results of [18, 19], a total of 11 cases have been ran. The cases and their characteristics are tabulated in Table 10.1. Case 10 been chosen to illustrate the logged data and explain the data processing used. The journal is rotating at 600 RPM while a load is imposed with the frequency of 2 Hz. Figures 10.4 and 10.5 contains the bearing load W (converted from load cell data with Equation (8.3)) and the displacements x, y, respectively.

Table 10.1: Overview of experimental cases.

Case #	$\tau = P_1/P_0$	$\sigma = \omega_1/\omega$	Type[a]
1	$\frac{1163}{528} \simeq 2.20$	$\frac{1}{10} = \frac{4}{40} \simeq 0.1$	Alternating (↓)
2	$\frac{434}{692} \simeq 0.63$	$\frac{2}{10} = \frac{48}{40} \simeq 0.2$	Fluctuating (↓)
3	$-\frac{869}{1638} \simeq -0.53$	$\frac{3}{2/3 \cdot 10} = \frac{18}{40} \simeq 0.45$	Fluctuating (↑)
4	$-\frac{945}{1782} \simeq -0.53$	$\frac{3/2}{2/3 \cdot 10} = \frac{9}{40} \simeq 0.23$	Fluctuating (↑)
5	$-\frac{707}{299} \simeq -2.37$	$\frac{2}{2/3 \cdot 10} = \frac{12}{40} \simeq 0.3$	Alt. (Fluct.) (↑)
6	$-\frac{620}{353} \simeq -1.75$	$\frac{2}{5} = \frac{16}{40} \simeq 0.4$	Alt. (Fluct.) (↑)
7	$-\frac{713}{302} \simeq -2.36$	$\frac{2}{2/3 \cdot 10} = \frac{12}{40} \simeq 0.3$	Alt. (Fluct.) (↑)
8	$\frac{757}{201} \simeq 3.76$	$\frac{2}{2/3 \cdot 10} = \frac{12}{40} \simeq 0.3$	Alt. (Fluct.) (↓)
9	$\frac{559}{853} \simeq 0.66$	$\frac{2}{2/3 \cdot 10} = \frac{12}{40} \simeq 0.3$	Fluctuating (↓)
10	$\frac{728}{1025} \simeq 0.71$	$\frac{2}{10} = \frac{8}{40} \simeq 0.2$	Fluctuating (↓)
11	$\frac{1367}{1489} \simeq 0.92$	$\frac{1}{10} = \frac{4}{40} \simeq 0.1$	Fluctuating (↓)

[a] Arrows indicate main load direction.

The measurements are made at a rate of 2 kHz ($\approx 2°$ CAD/sample). To avoid noise contributions, a simple smoothing is applied by averaging in increments of 20 samples. For the displacement, the two smoothed data sets are further averaged to give the journal orbit in the bearing center plane.

In Figure 10.4 the load imposed on the bearing is shown. The load plot reveals two things. First, it is easy to see the load type is fluctuating with $P1/P_0 \approx 1$, and second, the load is not completely symmetrical. The asymmetry is caused by the servo valve and related hardware. Remember, that the test bearing is preloaded with the table set-up (M_{table}), such that the fluctuating load is created by applying the inverse load. It means that the square shape at high loads is actually no load from the hydraulic cylinder, requiring the servo valve to be 'by-passed'. The difficulties of increasing the load on the hydraulic cylinder from zero to a small load, results in the poor response until a sufficient force is required, enabling the servo valve to leave the 'by-pass' position. This lag is mainly due to the design and tolerance of the valve porting, as the valve operates within a small percentage of its range (4 mA-20 mA) for the zero load. Well out of the zero load area, a smooth upper part is highlighting this issue.

Comparing Figure 10.5 with Figure 10.4 the damping of the system is evident. Consistently, a delay in the displacement response compared to the load input is seen. Figure 10.6 shows the orbit measured by the two sets of probes as well as the mean of the two. Comparing the two probes sets, a small misalignment is seen, with readings for Set 1 generally being shifted down and to the right. Set 1 also shows a $\pm 45°$ orientation, contrary to the $0°/90°$ orientation of Set 2.

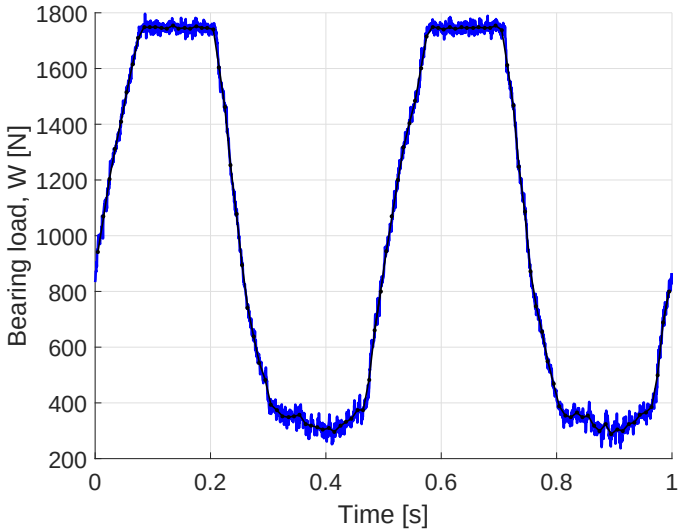

Figure 10.4: Load signal for Case 10.

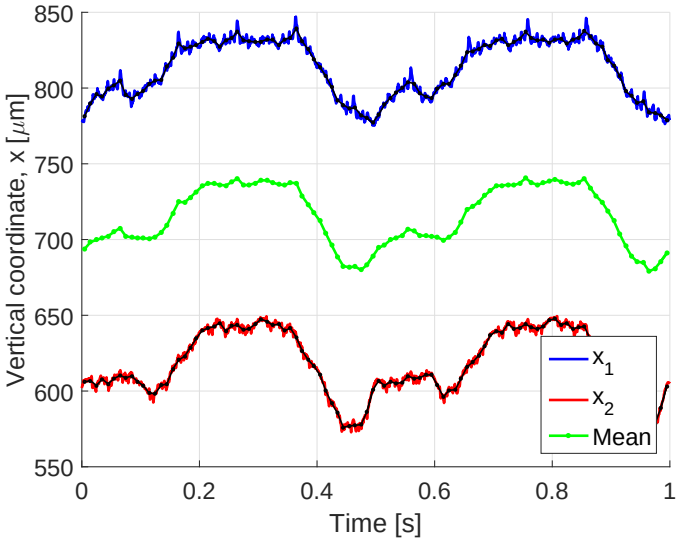

(a)

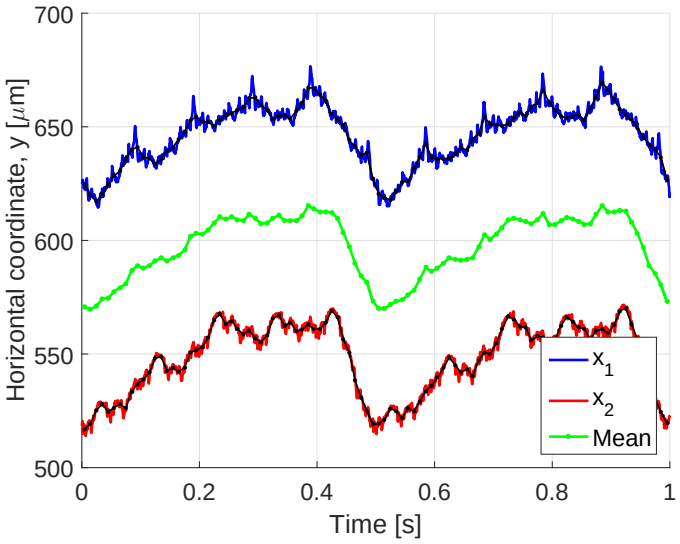

(b)

Figure 10.5: Displacement signals for Case 10.

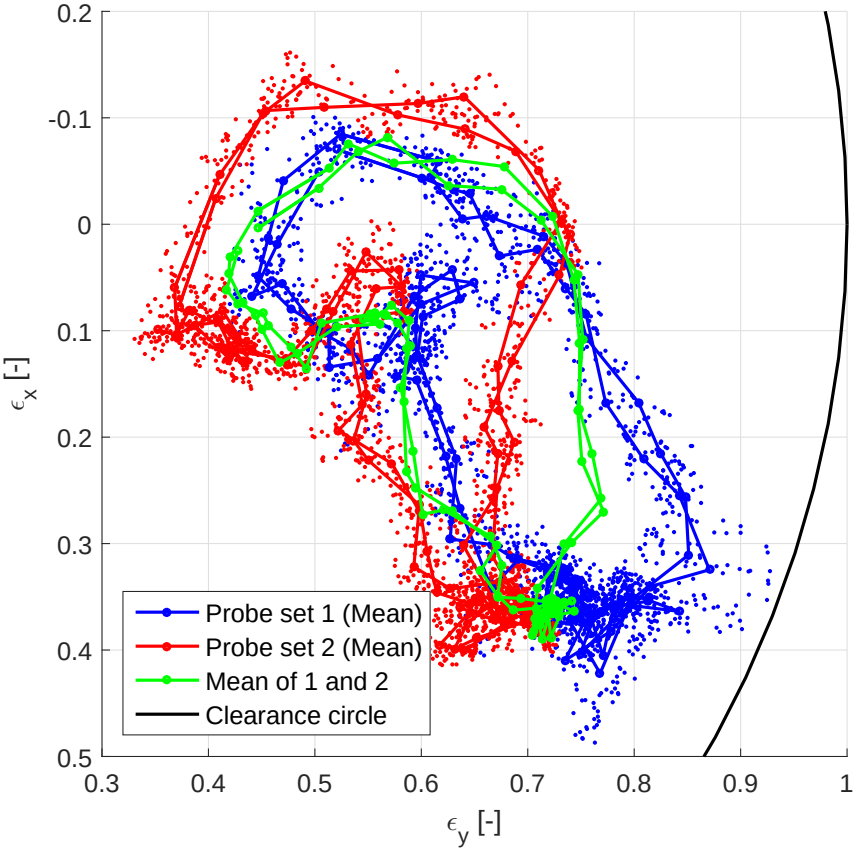

Figure 10.6: Journal orbit for Case 10. Dots represent all measurements and the points connected with lines represent the mean values.

Finite element simulation

The smoothed load function of Figure 10.4 has been applied to the FE code and a comparison with the experimental mean orbit is performed. Again, like explained for the locus curve, there is overall agreement with the general shape of the orbit, but at the same time a shift in the horizontal coordinate. To avoid the influence from Set 1, as explained on Page 94, Set 2 is included individually. As seen from Figure 10.6 the orbit is moving closer to the FE solution.

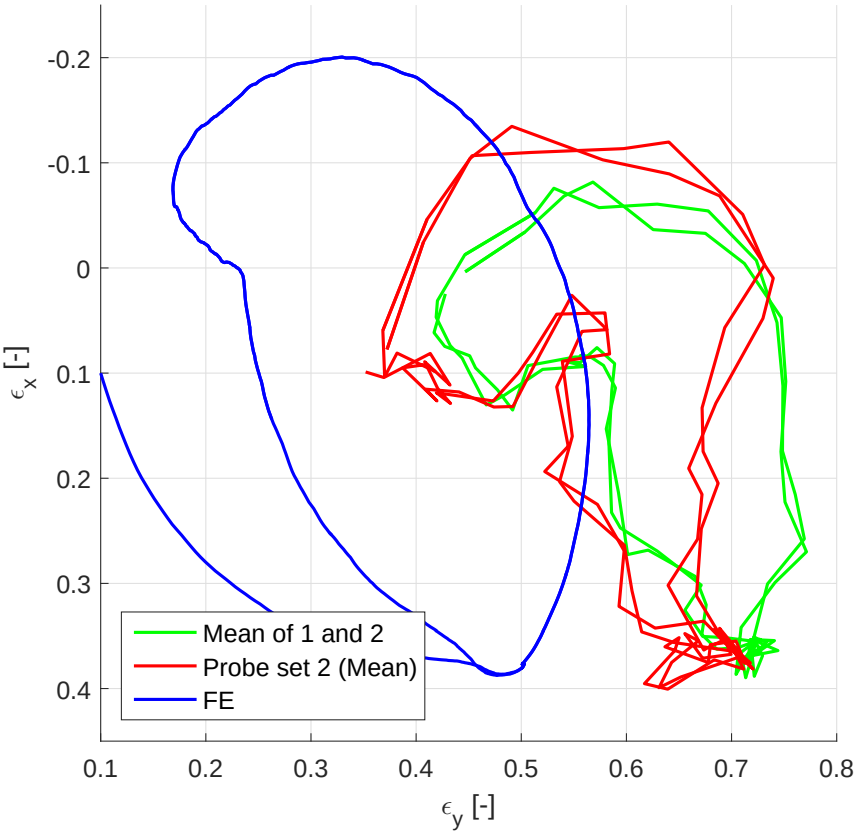

Figure 10.7: Journal orbit for Case 10, comparison of FE and experimental orbits.

Summary

Drawing on the experiences from Section 10.1.2 as well as the case example above, there is an acceptable agreement between the experimental results and

the FE code. Largest discrepancy is related with the y direction, indicating an issue with the calibration of the respective probes. Figure 10.6 reveals some slight misalignment, shown by the orientation of the orbits. Appendix F addresses the behaviour to be independent of the loading type. Also, due to the function of the polymer test bearing as an insulator, temperature is important.

Transition from alternating to fluctuating loads

Figure 10.8 shows the comparison between the experiments of Carl [19] and this thesis. The change in orbit is monitored as the loading changes from alternating ($\tau > 1$) to fluctuating ($\tau \leq 1$). Similar cases have been found with $\tau = 3.76$ and $\tau = 0.66$ versus $\tau = 4$ and $\tau = 1$ from [19]. Where Carl can apply a frequency ratio of $\sigma = 1$, the CTR rig is limited to $\sigma = 0.3$. Looking at the orbits, the major feature is the shrinking and 'collapse' of the orbit. This is even more prominent in [19], where a few more intermediate stages are shown. From the results of both [19] and [18] it is seen the orbit tends to be positioned normal to the steady locus curve and with the orbit centre on the curve.

For $\tau = 4$ the Sommerfeld number for [19] is $S_{\text{Carl}} = 0.039$, as given above, and for the CTR it is, using Equation (8.5) and Case 9 of Table 10.1, $S_{\text{CTR}} = 0.419$. Hence, the CTR bearing is loaded much lighter than that of [19]. Furthermore, the load signal frequency is three times slower (1/0.3) for the CTR.

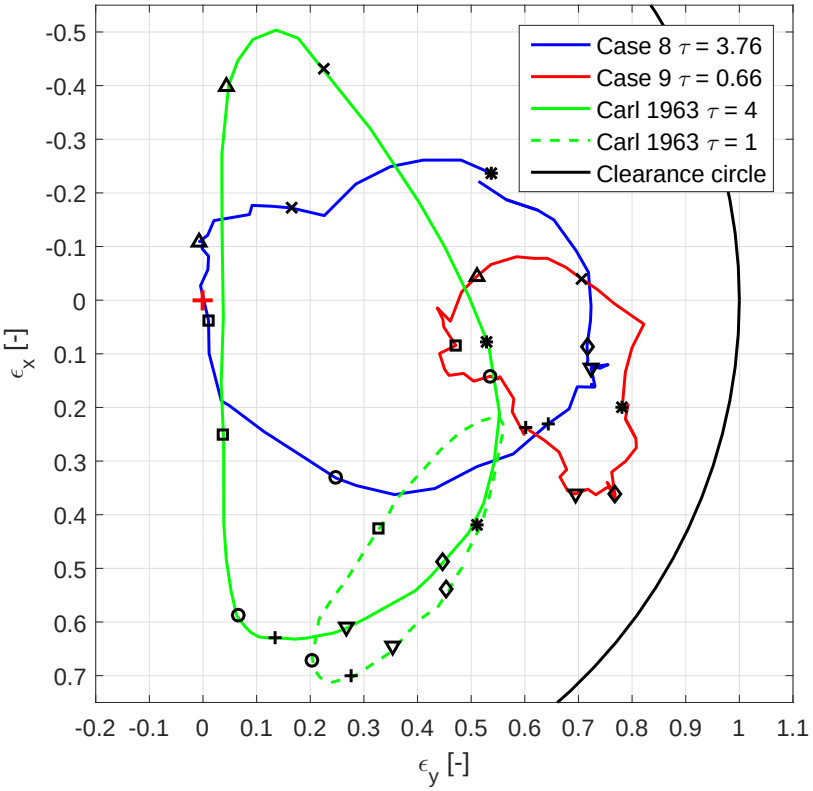

Figure 10.8: Journal orbit for Cases 8 and 9 and the comparable cases of Carl, 1963 [19]. Annotations represent an angular interval of $\omega_1 t = \frac{\pi}{4}$, with $* = 0, \times = \frac{\pi}{4}, \triangle = \frac{\pi}{2}, \square = \frac{3\pi}{4}, \bigcirc = \pi, + = \frac{5\pi}{4}, \triangledown = \frac{3\pi}{2}, \diamond = \frac{7\pi}{4}$.

10.2 Cavitation patterns

The ability to study the formation of striations during various load cases was one of the objectives with the cavitation test rig. However, this have proven rather tricky to document by photos. This is mainly related to the technical side of controlling lighting on the obviously curved surface of the journal, not creating shadows or otherwise dull areas.

Figures 10.9 and 10.10 contain examples for static and dynamic loading, respectively. The static loading generates clearly distinguishable striations and it is clear to the observer that the behaviour is static, with the only disturbances coming from a very minor misalignment of the journal. Contrary to this, the

dynamic loading leads to a periodic change in the number of striations as well as their angular location and extent.

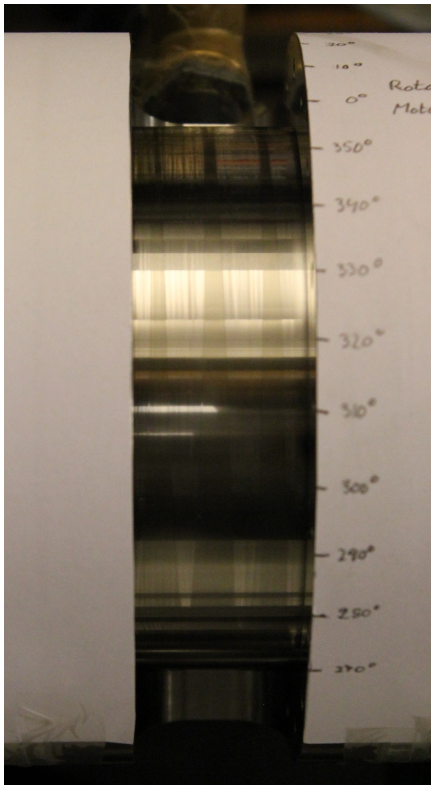

Figure 10.9: Static loading and its resulting steady film rupture. Operational conditions: 300 RPM, $W(t) = 1080$ N, CCW rotation (from bottom to top on figure).

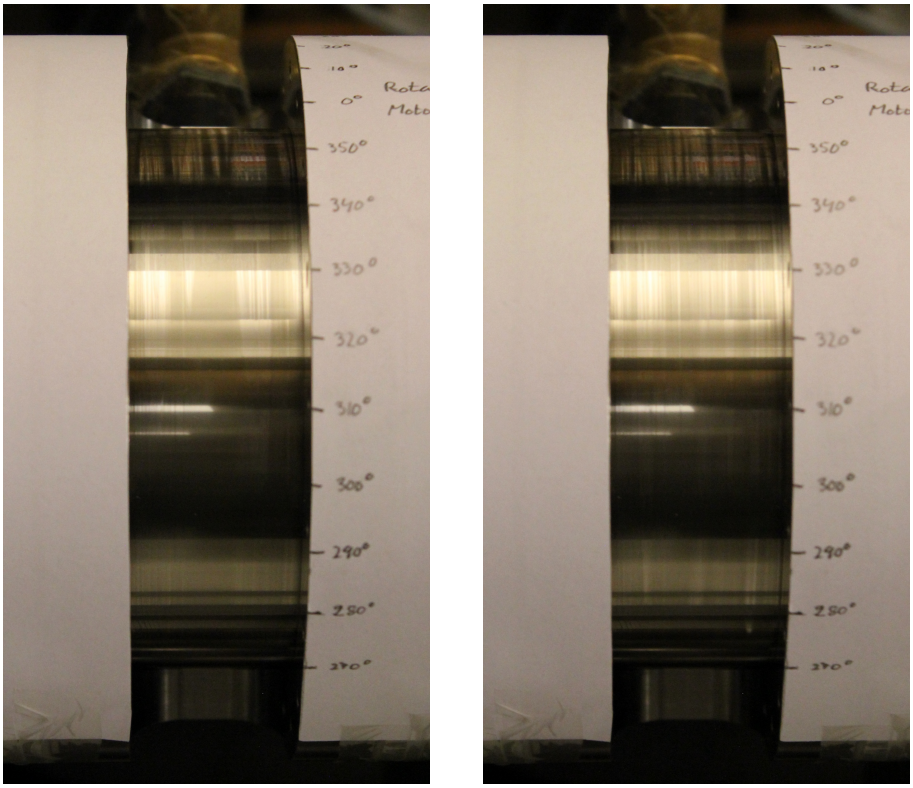

(a) (b)

Figure 10.10: Dynamic loading and its resulting unsteady film rupture. Operational conditions: 300 RPM, 320 N $\leq W(t) \leq$ 1320 N, $f = 2$ Hz, CCW rotation (from bottom to top on figure).

Chapter 11

Conclusions

The original onset of this project was to establish a tool for the design phase of new large, two-stroke engines with MAN Diesel & Turbo SE. A toolbox ensuring longevity as well as a reduction in friction loss. This was entitled as part of a work package for the EU project 'HERCULES-C'.

In order to come up with such tool, a basic understanding of the conditions under which a journal bearing situated in a large two-stroke engine is working, was desired. This mainly involved analysis of dynamic loading (combustion forces) and the practically unavoidable cavitation.

Gaining an understanding of the conditions required solving the governing equations. However, to be able to validate the theoretical findings, an experimental part consisting of a cavitation test rig was added to the project. The purpose of the rig was two-fold, namely visually monitoring the cavitation forming as well performing orbit measurements.

Computations on an 'arbitrary' groove design have been demonstrated, yielding overall agreement between the finite element version of Reynolds equation governing the thin film geometry of the bearing and the finite volume solution of the general Navier-Stokes equations obtained with the commercial code STAR-CCM+. The solutions make quantitative parameters as frictional torque (loss) and oil consumption readily available for further evaluation in a design process. Using a Navier-Stokes based program is a relatively new thing and hence having scientific relevance. During the project two papers have been published (Papers [P1] and [P2], with a third paper being prepared for publishing (Paper [P3]).

A fourth paper is planned on the experimental work conducted on the cavitation test rig. By means of sinusoidal loading engine-like conditions can be emulated. Despite operational limitations regarding load frequency and

proximity probes, the agreement between the experimentally obtained journal orbits and the corresponding numerical results are quite close. A comparison with previously published results also shows some agreement.

Combining the theoretical and experimental efforts, a capability to predict the behaviour of a dynamically loaded journal bearing emulating engine-like operational conditions has been obtained. Besides the overall behaviour an array of design-relevant quantities can be extracted.

11.1 Future work

With the ultimate goal of creating a bearing design tool still ahead, some obvious steps are also still left. Using the gained knowledge, both the experimental and theoretical aspects can be expanded.

Experimentally this is a two-sided affair. Firstly, by improving the data acquisition, better results are expected to be obtained for the current set-up, this means the test bearing with the point groove already mounted in the rig. Secondly, the circumferential grooved bearing awaits the same test course portrayed in this thesis for the point groove bearing. The comparison of those results with the numerical results already obtained for this thesis could form the basis for a journal paper.

For the theoretical work, two major areas to investigate are 1) contributions from elastic deformation of the bearing surface, i.e. upgrading the codes to solve the elasto-hydrodynamic lubrication (EHDL) problem and 2) improve the cavitation modelling. The EHDL is deemed necessary for the soft polymer test bearing according to the findings of a MSc thesis carried out in connection with this PhD project, but could just as well be relevant for a real engine bearing. All the papers read regarding the EHDL problem assumes a steel based bearing. The improvement in cavitation modelling has already been started, by looking into the formulation of dissolution in STAR-CCM+ and hence improving the gaseous cavitation modelling. In case of vaporous cavitation, STAR-CCM+ supports the Rayleigh-Plesset approach involving bubble dynamics.

Appendices

Appendix A

The Sommerfeld substitution

A closed-form solution of the Reynolds equation with long bearing theory was firs obtained by Sommerfeld in 1904. He used a substitution based on tangent to substitute θ into the variable ψ, and not the one that bears his name today. This method was first described a year later by Hardy [44]. Today, the variable ψ is known as the Sommerfeld variable.

Such peculiar situations occur from time to time in the scientific world and the present case is discussed more in depth by [45, 46].

The latter substitution, also shown as Equation (A.1), is of the form $a^2 - b^2 = (a + b\cos x)(a - b\cos y)$ [46] and has the property that for $\theta = 0, \pi, 2\pi$, also the substitution variable $\psi = 0, \pi, 2\pi$.

$$\bar{h} = 1 + \varepsilon\cos\theta = \frac{1 - \varepsilon^2}{1 - \varepsilon\cos\psi} \tag{A.1}$$

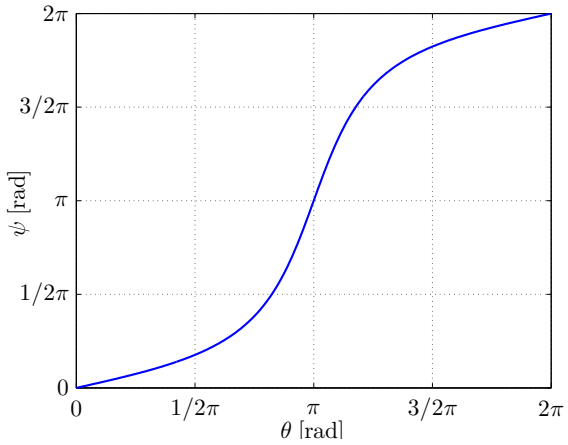

Figure A.1: Relationship between θ and ψ plotted from Equation (A.6) with $\varepsilon = 0.85$.

A.1 Expressions for θ and ψ

Expressions for θ is obtained with a little manipulation:

$$\cos\theta = \frac{\cos\psi - \varepsilon}{1 - \varepsilon\cos\psi} \tag{A.2}$$

$$\sin\theta = \frac{\sqrt{1-\varepsilon^2}\cdot\sin\psi}{1 - \varepsilon\cos\psi} \tag{A.3}$$

$$\mathrm{d}\theta = \frac{\sqrt{1-\varepsilon^2}\cdot\mathrm{d}\psi}{1 - \varepsilon\cos\psi} = \frac{\bar{h}\,\mathrm{d}\psi}{\sqrt{1-\varepsilon^2}} \tag{A.4}$$

The angular increment $\mathrm{d}\theta$ arises from the assumption of small angles, such that for $\theta \simeq 0$ is $\sin\theta \simeq \theta$ and with the film thickness given as (recall Equation (3.18)):

$$\bar{h} = 1 + \varepsilon\cos\theta = \frac{1-\varepsilon^2}{1 - \varepsilon\cos\psi} \tag{A.5}$$

From Equations (A.2) and (A.3) it can directly be found that:

$$\cos\psi = \frac{\varepsilon + \cos\theta}{1 + \varepsilon\cos\theta} \tag{A.6}$$

$$\sin\psi = \frac{\sqrt{1-\varepsilon^2}\cdot\sin\theta}{1 + \varepsilon\cos\theta} \tag{A.7}$$

A.2 Integrals

With the relations of Section A.1 the integrals required to solve the Equations (4.13) and (4.30) and their related equations, can be found as:

$$\int \frac{1}{\bar{h}^2}\,\mathrm{d}\theta = \frac{1}{(1-\varepsilon^2)^{3/2}}(\psi - \varepsilon\sin\psi) \tag{A.8}$$

$$\sin\theta = \frac{\sqrt{1-\varepsilon^2}\cdot\sin\psi}{1-\varepsilon\cos\psi} \tag{A.9}$$

$$\mathrm{d}\theta = \frac{\sqrt{1-\varepsilon^2}\cdot\mathrm{d}\psi}{1-\varepsilon\cos\psi} = \frac{\bar{h}\,\mathrm{d}\psi}{\sqrt{1-\varepsilon^2}} \tag{A.10}$$

Appendix B

Green-Gauss extensions

The expression occurring from the Galerkin method (Equation (6.7) can be rewritten, using the Green-Gauss theorem:

$$\int_A \beta \frac{\partial \mathbf{f}}{\partial \theta} \, \mathrm{d}A = \int_S \beta \mathbf{f} n_\theta \, \mathrm{d}S - \int_A \frac{\partial \beta}{\partial \theta} \mathbf{f} \, \mathrm{d}A \tag{B.1}$$

The three terms become:

$$\begin{aligned} \int_A \mathbf{N}^T \left[\frac{\partial}{\partial \theta} \left(\bar{h}^3 \frac{\partial \bar{\mathbf{p}}}{\partial \theta} \right) \right] \mathrm{d}A = & \int_S \mathbf{N}^T \bar{h}^3 \frac{\partial \bar{\mathbf{p}}}{\partial \theta} n_\theta \, \mathrm{d}S \\ & - \int_A \left(\frac{\partial \mathbf{N}}{\partial \theta} \right)^T \bar{h}^3 \frac{\partial \bar{\mathbf{p}}}{\partial \theta} \, \mathrm{d}A \end{aligned} \tag{B.2a}$$

$$\begin{aligned} \int_A \mathbf{N}^T \left[\frac{\partial}{\partial \zeta} \left(\bar{h}^3 \frac{\partial \bar{\mathbf{p}}}{\partial \zeta} \right) \right] \mathrm{d}A = & \int_S \mathbf{N}^T \bar{h}^3 \frac{\partial \bar{\mathbf{p}}}{\partial \zeta} n_\zeta \, \mathrm{d}S \\ & - \int_A \left(\frac{\partial \mathbf{N}}{\partial \zeta} \right)^T \bar{h}^3 \frac{\partial \bar{\mathbf{p}}}{\partial \zeta} \, \mathrm{d}A \end{aligned} \tag{B.2b}$$

$$\int_A \mathbf{N}^T \frac{\partial \bar{h}}{\partial \theta} \, \mathrm{d}A = \int_S \mathbf{N}^T \bar{h} \, n_\theta \, \mathrm{d}S - \int_A \left(\frac{\partial \mathbf{N}}{\partial \theta} \right)^T \bar{h} \, \mathrm{d}A \tag{B.2c}$$

Appendix C

Nodal and element numbering

Demonstration of nodal and element numbering and the resulting banded structure of the stiffness matrix. Figure C.1 shows the element numbering in blue squares, with the elements made up from the nodal points framed in red. Numbering in columns instead of rows reduces the bandwidth of the resulting stiffness matrix, see Figure C.2. Here node 1 has connectivity to nodes 2 and 6, contrary to nodes 2 and 15.

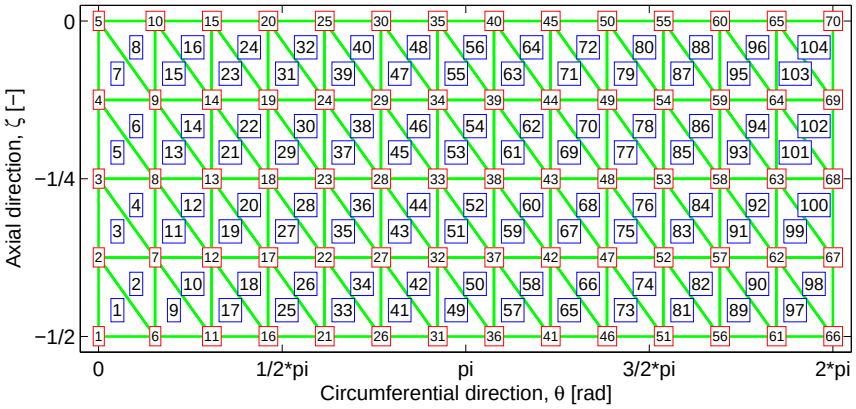

Figure C.1: Example on nodal and element numbering.

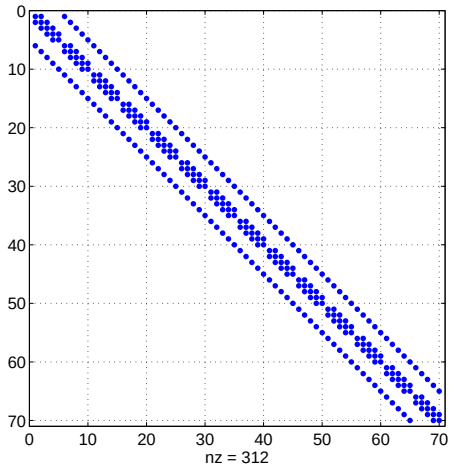

Figure C.2: Sparsity of the stiffness matrix.

Appendix D

Functional derivation

For a finite element discretisation a functional F is required, for discretising a given function f. The functional F should possess the property of yielding the original equation f, when inserted into the Euler-Lagrange equation. The Euler-Lagrange equation is given as [38]:

$$\frac{\partial F}{\partial g} - \frac{\partial}{\partial x_1}\left(\frac{\partial F}{\partial {}^{\partial g}/_{\partial x_1}}\right) - \frac{\partial}{\partial x_2}\left(\frac{\partial F}{\partial {}^{\partial g}/_{\partial x_2}}\right) = 0 \tag{D.1}$$

Using the Euler-Lagrange equation (Equation (D.1)) in the problem specific form (Equation (D.2)), thus gives the five functionals.

$$\frac{\partial F}{\partial \bar{p}_i} - \frac{\partial}{\partial \theta}\left(\frac{\partial F}{\partial {}^{\partial \bar{p}_i}/_{\partial \theta}}\right) - \frac{\partial}{\partial \zeta}\left(\frac{\partial F}{\partial {}^{\partial \bar{p}_i}/_{\partial \zeta}}\right) = 0, \quad i = 0, 1, \ldots, 4 \tag{D.2}$$

The derivation of the five functionals $F_i, i = 0, 1, \ldots, 4$ is given on the following pages.

D.1 Functional for $\bar{p}_0$

Proposed functional:

$$F_0 = -\left(-\frac{\bar{h}_0^3}{2}\left[\left(\frac{\partial \bar{p}_0}{\partial \theta}\right)^2 + \left(\frac{\partial \bar{p}_0}{\partial \zeta}\right)^2\right] + \bar{h}\,\frac{\partial \bar{p}_0}{\partial \theta} + \frac{2\nu}{\omega}\left(\dot{\bar{x}}_0 \sin\theta' - \dot{\bar{y}}_0 \cos\theta'\right)\frac{\partial \bar{p}_0}{\partial \theta}\right) \tag{D.3}$$

First term:

$$\frac{\partial F_0}{\partial \bar{p}_0} = 0 \tag{D.4}$$

Argument, second term:

$$\frac{\partial F_0}{\partial \,{}^{\partial \bar{p}_0}/_{\partial \theta}} = \bar{h}_0^3\,\frac{\partial \bar{p}_0}{\partial \theta} - \bar{h}_0 - \frac{2\nu}{\omega}\left(\dot{\bar{x}}_0 \sin\theta' - \dot{\bar{y}}_0 \cos\theta'\right) \tag{D.5}$$

Argument, third term:

$$\frac{\partial F_0}{\partial \,{}^{\partial \bar{p}_0}/_{\partial \zeta}} = \bar{h}_0^3\,\frac{\partial \bar{p}_0}{\partial \zeta} \tag{D.6}$$

Insertion of Equations (D.4)-(D.6) into Equation (D.2) leads back to Equation (5.12a):

$$\frac{\partial}{\partial \theta}\left(\bar{h}_0^3\,\frac{\partial \bar{p}_0}{\partial \theta}\right) + \frac{\partial}{\partial \zeta}\left(\bar{h}_0^3\,\frac{\partial \bar{p}_0}{\partial \zeta}\right) = \left(-\bar{x}_0 \sin\theta' + \bar{y}_0 \cos\theta'\right) + \frac{2\nu}{\omega}\left(\dot{\bar{x}}_0 \cos\theta' + \dot{\bar{y}}_0 \sin\theta'\right) \tag{D.7}$$

D.2 Functional for $\bar{p}_1$

Proposed functional:

$$F_1 = -\left(-\frac{\bar{h}_0^3}{2}\left[\left(\frac{\partial \bar{p}_1}{\partial \theta}\right)^2 + \left(\frac{\partial \bar{p}_1}{\partial \zeta}\right)^2\right] - 3\bar{h}_0^2 \cos\theta' \left(\frac{\partial \bar{p}_1}{\partial \theta}\frac{\partial \bar{p}_0}{\partial \theta} + \frac{\partial \bar{p}_1}{\partial \zeta}\frac{\partial \bar{p}_0}{\partial \zeta}\right) + \cos\theta' \frac{\partial \bar{p}_1}{\partial \theta}\right) \tag{D.8}$$

First term:

$$\frac{\partial F_1}{\partial \bar{p}_1} = 0 \tag{D.9}$$

Argument, second term:

$$\frac{\partial F_1}{\partial {}^{\partial \bar{p}_1}/_{\partial \theta}} = \bar{h}_0^3 \frac{\partial \bar{p}_1}{\partial \theta} + 3\bar{h}_0^2 \cos\theta' \frac{\partial \bar{p}_0}{\partial \theta} - \cos\theta' \tag{D.10}$$

Argument, third term:

$$\frac{\partial F_1}{\partial {}^{\partial \bar{p}_1}/_{\partial \zeta}} = \bar{h}_0^3 \frac{\partial \bar{p}_1}{\partial \zeta} + 3\bar{h}_0^2 \cos\theta' \frac{\partial \bar{p}_0}{\partial \zeta} \tag{D.11}$$

Insertion of Equations (D.9)-(D.11) into Equation (D.2) leads back to Equation (5.12b):

$$\frac{\partial}{\partial \theta}\left(\bar{h}_0^3 \frac{\partial \bar{p}_1}{\partial \theta}\right) + \frac{\partial}{\partial \zeta}\left(\bar{h}_0^3 \frac{\partial \bar{p}_1}{\partial \zeta}\right) = -\frac{\partial}{\partial \theta}\left(3\bar{h}_0^2 \cos\theta' \frac{\partial \bar{p}_0}{\partial \theta}\right) - \frac{\partial}{\partial \zeta}\left(3\bar{h}_0^2 \cos\theta' \frac{\partial \bar{p}_0}{\partial \zeta}\right) - \sin\theta' \tag{D.12}$$

D.3 Functional for $\bar{p}_2$

Proposed functional:

$$F_2 = -\Bigg(-\frac{\bar{h}_0^3}{2}\left[\left(\frac{\partial \bar{p}_2}{\partial \theta}\right)^2 + \left(\frac{\partial \bar{p}_2}{\partial \zeta}\right)^2\right] - 3\bar{h}_0^2 \sin\theta' \left(\frac{\partial \bar{p}_2}{\partial \theta}\frac{\partial \bar{p}_0}{\partial \theta} + \frac{\partial \bar{p}_2}{\partial \zeta}\frac{\partial \bar{p}_0}{\partial \zeta}\right) + \sin\theta' \frac{\partial \bar{p}_2}{\partial \theta}\Bigg) \tag{D.13}$$

First term:

$$\frac{\partial F_2}{\partial \bar{p}_2} = 0 \tag{D.14}$$

Argument, second term:

$$\frac{\partial F_2}{\partial {}^{\partial \bar{p}_2}/_{\partial \theta}} = \bar{h}_0^3 \frac{\partial \bar{p}_2}{\partial \theta} + 3\bar{h}_0^2 \sin\theta' \frac{\partial \bar{p}_0}{\partial \theta} - \sin\theta' \tag{D.15}$$

Argument, third term:

$$\frac{\partial F_2}{\partial {}^{\partial \bar{p}_2}/_{\partial \zeta}} = \bar{h}_0^3 \frac{\partial \bar{p}_2}{\partial \zeta} + 3\bar{h}_0^2 \sin\theta' \frac{\partial \bar{p}_0}{\partial \zeta} \tag{D.16}$$

Insertion of Equations (D.14)-(D.16) into Equation (D.2) leads back to Equation (5.12c):

$$\frac{\partial}{\partial \theta}\left(\bar{h}_0^3 \frac{\partial \bar{p}_2}{\partial \theta}\right) + \frac{\partial}{\partial \zeta}\left(\bar{h}_0^3 \frac{\partial \bar{p}_2}{\partial \zeta}\right) = -\frac{\partial}{\partial \theta}\left(3\bar{h}_0^2 \sin\theta' \frac{\partial \bar{p}_0}{\partial \theta}\right) - \frac{\partial}{\partial \zeta}\left(3\bar{h}_0^2 \sin\theta' \frac{\partial \bar{p}_0}{\partial \zeta}\right) + \cos\theta' \tag{D.17}$$

D.4 Functional for $\bar{p}_3$

Proposed functional:

$$F_3 = -\left(-\frac{\bar{h}_0^3}{2} \left[\left(\frac{\partial \bar{p}_3}{\partial \theta} \right)^2 + \left(\frac{\partial \bar{p}_3}{\partial \zeta} \right)^2 \right] + \frac{2\nu}{\omega} \sin\theta' \, \frac{\partial \bar{p}_3}{\partial \theta} \right) \tag{D.18}$$

First term:

$$\frac{\partial F_3}{\partial \bar{p}_3} = 0 \tag{D.19}$$

Argument, second term:

$$\frac{\partial F_3}{\partial \, {}^{\partial \bar{p}_3}/_{\partial \theta}} = \bar{h}_0^3 \, \frac{\partial \bar{p}_3}{\partial \theta} - \frac{2\nu}{\omega} \sin\theta' \tag{D.20}$$

Argument, third term:

$$\frac{\partial F_3}{\partial \, {}^{\partial \bar{p}_3}/_{\partial \zeta}} = \bar{h}_0^3 \, \frac{\partial \bar{p}_3}{\partial \zeta} \tag{D.21}$$

Insertion of Equations (D.19)-(D.21) into Equation (D.2) leads back to Equation (5.12d):

$$\frac{\partial}{\partial \theta} \left(\bar{h}_0^3 \, \frac{\partial \bar{p}_3}{\partial \theta} \right) + \frac{\partial}{\partial \zeta} \left(\bar{h}_0^3 \, \frac{\partial \bar{p}_3}{\partial \zeta} \right) = \frac{2\nu}{\omega} \cos\theta' \tag{D.22}$$

D.5 Functional for $\bar{p}_4$

Proposed functional:

$$F_4 = -\left(-\frac{\bar{h}_0^3}{2} \left[\left(\frac{\partial \bar{p}_4}{\partial \theta} \right)^2 + \left(\frac{\partial \bar{p}_4}{\partial \zeta} \right)^2 \right] - \frac{2\nu}{\omega} \cos\theta' \, \frac{\partial \bar{p}_4}{\partial \theta} \right) \tag{D.23}$$

First term:

$$\frac{\partial F_4}{\partial \bar{p}_4} = 0 \tag{D.24}$$

Argument, second term:

$$\frac{\partial F_4}{\partial \, {}^{\partial \bar{p}_4}/_{\partial \theta}} = \bar{h}_0^3 \, \frac{\partial \bar{p}_4}{\partial \theta} + \frac{2\nu}{\omega} \cos\theta' \tag{D.25}$$

Argument, third term:

$$\frac{\partial F_4}{\partial \, {}^{\partial \bar{p}_4}/_{\partial \zeta}} = \bar{h}_0^3 \, \frac{\partial \bar{p}_4}{\partial \zeta} \tag{D.26}$$

Insertion of Equations (D.24)-(D.26) into Equation (D.2) leads back to Equation (5.12e):

$$\frac{\partial}{\partial \theta} \left(\bar{h}_0^3 \, \frac{\partial \bar{p}_4}{\partial \theta} \right) + \frac{\partial}{\partial \zeta} \left(\bar{h}_0^3 \, \frac{\partial \bar{p}_4}{\partial \zeta} \right) = \frac{2\nu}{\omega} \sin\theta' \tag{D.27}$$

Appendix E

Technical drawings of polymer bearings for cavitation test rig

Technical drawings for the two bearings considered in Chapters 8 and 9.

- `CTR-1-1-2` Point groove (currently mounted in test rig).
- `CTR-1-1-2` Circumferential groove.

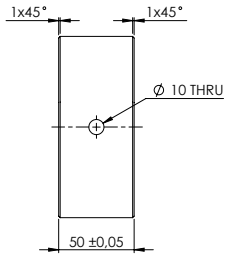

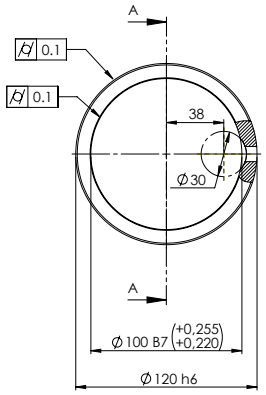

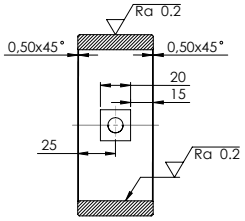

SECTION A-A

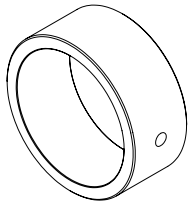

Skarpe kanter brydes

Ikke-tolerancesatte mål efter DS/ISO 2768-1 f og DS/ISO 2768-2 K

Indersiden og ydersiden poleres.

Laves i én opspænding

Undgå opspænding på partens geometri.
Brug f.eks. råemne på 150mm og afstik færdig part.

Antal: 1 stk.

Suzan Kurt tlf: [Removed]

UNLESS OTHERWISE SPECIFIED: DIMENSIONS ARE IN MILLIMETERS SURFACE FINISH: TOLERANCES: LINEAR: ANGULAR:	FINISH:				DEBUR AND BREAK SHARP EDGES	DO NOT SCALE DRAWING / REVISION
	NAME	SIGNATURE	DATE			Suzan Kurt
DRAWN	Suzan Kurt		15-12-14			TITLE: Leje type 2
CHK'D						
APPV'D						
MFG						
Q.A				MATERIAL: Plexiglas		DWG NO. CTR-1-1-2 / A3
				WEIGHT:		SCALE:1:2 / SHEET 1 OF 1

SolidWorks Student Edition.
For Academic Use Only.

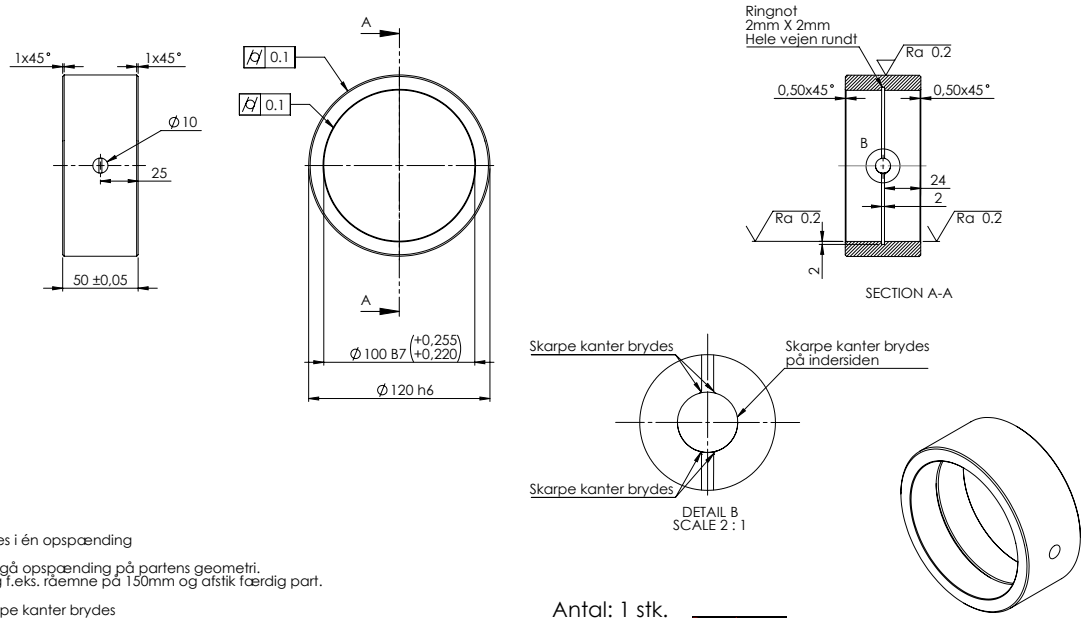

Laves i én opspænding

Undgå opspænding på partens geometri.
Brug f.eks. råemne på 150mm og afstik færdig part.

Skarpe kanter brydes

Ikke-tolerancesatte mål efter DS/ISO 2768-1 f og DS/ISO 2768-2 K

Indersiden og ydersiden poleres.

Antal: 1 stk.
Suzan Kurt tlf: Removed

UNLESS OTHERWISE SPECIFIED: DIMENSIONS ARE IN MILLIMETERS SURFACE FINISH: TOLERANCES: LINEAR: ANGULAR:	FINISH:		DEBUR AND BREAK SHARP EDGES	DO NOT SCALE DRAWING	REVISION
				Suzan Kurt	
	NAME	SIGNATURE	DATE	TITLE:	
DRAWN	Suzan Kurt		15-12-14	Leje type 3	
CHK'D					
APPV'D					
MFG					
Q.A			MATERIAL: Plexiglas	DWG NO. CTR-1-1-3	A3
			WEIGHT:	SCALE:1:2	SHEET 1 OF 1

SolidWorks Student Edition.
For Academic Use Only.

Appendix F

Locus curve additionals

As a demonstration of the inclinations of measurements of probe set 1 relative to probe set 2, Figure F.1 serves as a supplement to Figure 10.6 to verify the inclined trend is unaffected by the loading type, whether being static or dynamic. The data shown in Figure F.1 are those used to create Figure 10.2.

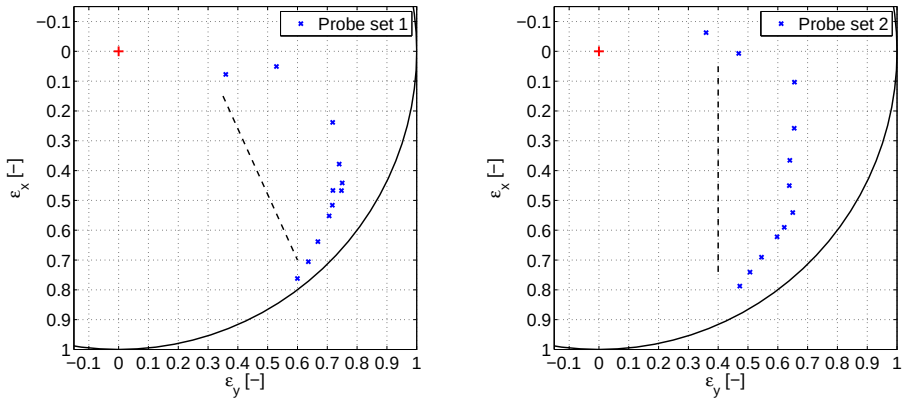

(a) (b)

Figure F.1: Locus curves by the two probe sets, demonstrating the trend in measurements by the dashed line.

Publications

Publication 1

Application of finite elements and computational fluid dynamics to predict and improve the filling ratio in journal bearings under dynamic loading

Published in *Proceedings of NSCM-27: the 27th Nordic Seminar on Computational Mechanics.*

Accepted for publishing on September 30, 2014.

27th Nordic Seminar on Computational Mechanics
NSCM-27
A. Eriksson, A. Kulachenko, M. Mihaescu and G. Tibert (Eds.)
©KTH, Stockholm, 2014

APPLICATION OF FINITE ELEMENTS AND COMPUTATIONAL FLUID DYNAMICS TO PREDICT AND IMPROVE THE FILLING RATIO IN JOURNAL BEARINGS UNDER DYNAMIC LOADING

CHRISTIAN K. CHRISTIANSEN[*], PEDER KLIT[*], JENS H. WALTHER[*,†] AND ANDERS VØLUND[‡]

[*]Department of Mechanical Engineering (DTU Mekanik)
Technical University of Denmark (DTU)
Nils Koppels Allé buildg. 404, DK-2800, Denmark
e-mail: chkch@mek.du.dk, web page: http://www.mek.dtu.dk

[†]Computational Science & Engineering Laboratory (CSElab)
Swiss Federal Institute of Technology (ETH)
ETH-Zentrum, CLT F 11, CH-8092 Zürich, Switzerland
e-mail: walther@mavt.ethz.ch - Web page: http://www.cse-lab.ethz.ch

[‡]MAN Diesel & Turbo SE
Teglholmsgade 41, DK-2450 Copenhagen SV, Denmark
e-mail: info-cph@mandieselturbo.com - Web page: http://www.mandieselturbo.com

Key words: Finite Element, Computational Fluid Dynamics, Cavitation, Journal Bearing.

Summary. Journal bearings have seen widespread use in combustion engines since the earliest engine types arose more than one hundred years ago. This is due to a high load carrying capacity relative to the costs of the bearing. The journal bearing is a simple hydrodynamic (velocity-driven) setup with a shaft (journal) carried on a lubricant film within a housing (bushing). From the geometry of the bearing, with its converging-diverging zone, it is prone to cavitation. The cavitation ensures a stable bearing, but can also be harmful by ruining the load carrying capacity. In the diverging zone, the volume increases and mass conservation then leads to cavitation and the filling ratio is simply a measure of how much of the volume is filled with lubricant. Cavitation and filling ratio is well-known for a statically loaded bearing, but not for dynamic cases and hence especially interesting with the combustion loads varying highly in time. Today's marine engine bearings are stressed significantly, as ship owners are required to meet increasingly stricter emission requirements. An improvement in engine efficiency is obtained by lowering engine RPM and increasing the engine's mean pressure. These worsened operating conditions require an improved understanding of the flow patterns within the bearing to avoid breakthrough of the oil film and the resulting, fatal metal-metal contact between journal and bushing.

The present work features a two-fold investigation; an in-house finite element (FE) code and use of the commercial package STAR-CCM+ for the computational fluid dynamics (CFD). In terms of pure computational speed, the governing Reynolds equation (2D) modelled with

FE is superior to the CFD where the 3D Navier-Stokes equations are solved. With the 2D FE, a perturbation method leads to an efficient prediction of the journal orbit for a given (combustion) load cycle with FE. For a known journal orbit the volume of cavitated zone(s) is easily determined. This result can be used for investigation of the effect from the number and position of oil supply grooves on the filling ratio. For more complex geometries the CFD code is useful as well as for validating the 2D assumptions used in the FE model.

1 THE JOURNAL BEARING

The journal bearing is a very simple setup as indicated in Figure 1a, consisting of a shaft (journal) inside a housing (bushing). A tiny gap between those two elements is filled with lubricant and once rotating, the shaft will hover on top of this thin lubricant film, very much similar to a car aquaplaning on a wet road. This gap, or clearance, is a small fraction of the diameter, i.e. $C \approx 1/1000D$.

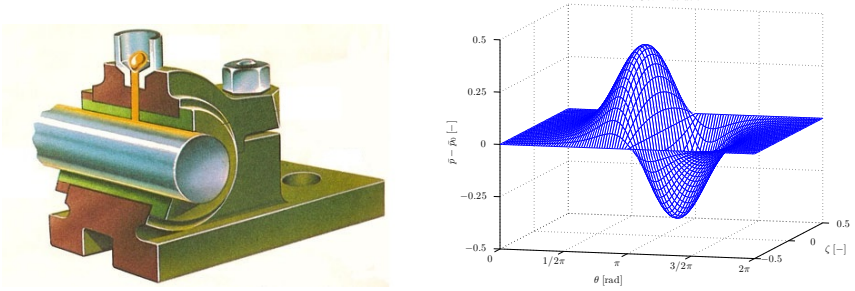

(a) (b)

Figure 1: (a) Sketch of journal bearing[1]. (b) The analytical solution to the pressure distribution for a short bearing[2], with θ being the circumferential and ζ the axial non-dimensional coordinate, respectively.

As an external load is applied to the journal, it will move away from the bushing centre. This offset or eccentricity will generate a converging-diverging zone with a pumping effect. Once the hydraulic forces of this 'pump' balances the external load, an equilibrium is obtained. This thin film lubrication is governed by Reynolds equation relating pressure p, viscosity μ, density ρ and film thickness h:

$$\frac{1}{R^2}\frac{\partial}{\partial\theta}\left(\frac{\rho h^3}{12\mu}\frac{\partial p}{\partial\theta}\right)+\frac{\partial}{\partial z}\left(\frac{\rho h^3}{12\mu}\frac{\partial p}{\partial z}\right)=\frac{U}{2R}\frac{\partial\rho h}{\partial\theta}+\frac{\mathrm{d}h}{\mathrm{d}t} \tag{1}$$

Where $R = D/2$ and θ, z denotes circumferential and axial coordinates, respectively. Figure 1b shows the analytical pressure distribution in the lubricant exhibiting negative pressure. As fluids cannot take up (large) negative pressures, the physical distribution has a left part with high load carrying capacity (converging part) and a right part with practically zero pressure and hence no load carrying capacity (diverging part).

The above is true for the statically loaded bearing and the behaviour is well understood. What is interesting is the behaviour under dynamic loading, as in combustion engines, when the time-varying load moves the journal in an orbit and the position of the area of load carrying capacity changes rapidly.

2 MODELLING

From the ratio between C and D a 2D justification as shown in Figure 2 is often applied, e.g. in the derivation of Equation (1). To investigate more complicated setups, not necessarily being valid as 2D assumptions, the commercial CFD code STAR-CCM+ is used. Being a 3D code the problem arises in meshing. As an initial test case, the simple geometry of an in-house cavitation test rig[3] is considered. The geometry and example of the mesh is shown in Figure 3.

Due to the thin film part of the geometry the built-in mesher has difficulties in obtaining a low cell number. Other authors[4,5] have investigated a very similar geometry and a radial cell count of 14-20 is mentioned[4]. For the static case this is not a problem, but for a dynamically loaded bearing the journal displacements follows a complicated orbit, which will require small time steps and a good spatial resolution. To obtain a suitable mesh, several methods have been tried out;

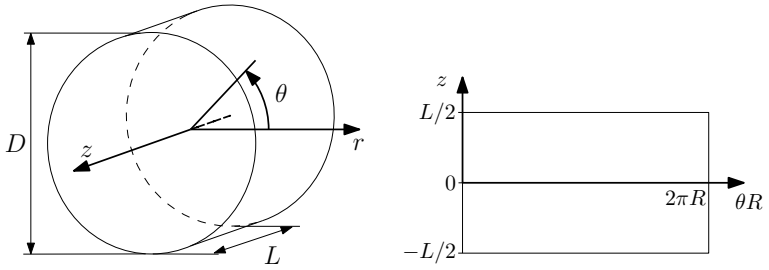

(a) Bearing with coordinate system. (b) Unfolded geometry.

Figure 2: (a) Orientation of the cylindrical coordinate system exploiting the symmetry. (b) Unfolded bearing geometry.

polyhedral, tetrahedral, trimmed (brick) and extruded meshes. Those are all unstructured in the sense they adapt to the geometry in an automatic way. Mathematically this has its limitations in a multiple of parameters trying to ensure a decent quality of the mesh. Another method that may be more cumbersome, but leaves the user in total control is the 'directed mesher'. The outcome is depicted in Figure 3b and consists of a sketched mesh, allowing for a very regular mesh, being extruded along an axial dimension. Where the requirement to a uniform, axial thickness for the domain can be circumvented by splitting the domain up into sub-domains, the mesher is sensitive to movements and requires regeneration of sketches and meshes.

The most promising approach is the overset ('chimera') mesher. A background mesh is generated constituting the bushing and externals, but also a (coarser) mesh at the location of the journal. An overlapping mesh is then imposed on top of the background, forming the journal and extending beyond the bushing. For the overset process the meshes are subtracted to obtain

the computational mesh in the overlapping areas of the two meshes. This type of mesh is also specifically designed for simulation incorporating large displacements.

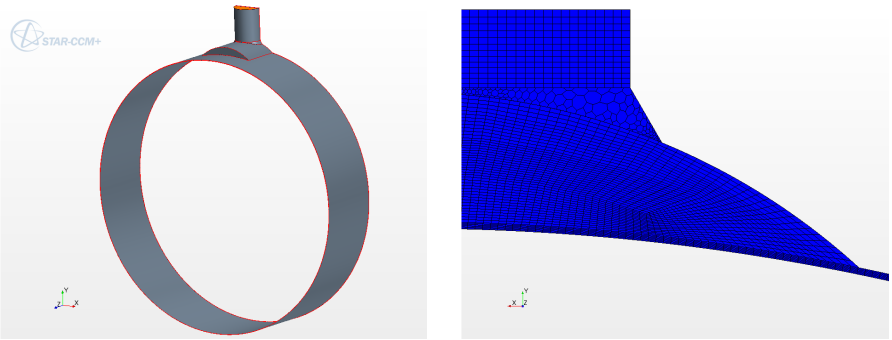

(a) Bearing geometry. (b) Detail of mesh.

Figure 3: (a) Test rig bearing. (b) Combination of directed and unstructured meshes.

3 CONCLUSIONS

1. Meshing the simple, but thin, journal bearing geometry is far from trivial.
2. Whereas ordinary methods generate meshes with large number of cells, the overset mesher seems promising both in terms of mesh quality as well as built-in translation of parts of the domain.

REFERENCES

[1] David Darling. Bearing. Retrieved from `http://www.daviddarling.info/encyclopedia/B/bearing.html` on October 19 2012.

[2] Ocvirk, F. W. Short-Bearing Approximation for Full Journal Bearings. Technical note 2808, Cornell University (1952).

[3] Christiansen, C., Klit, P., Walther, J. & Vølund, A. Orbit prediction of a journal bearing - Finite Element modelling and experimental studies (2014). Journal paper submitted.

[4] Schmidt, M., Stücke, P. & Nobis, M. Numerical meshing issues for three-dimensional flow simulation in journal bearings. 3rd Micro and Nano Flows Conference (2011). Thessaloniki, Greece, 22-24 August 2011.

[5] Riedel, M., Schmidt, M. & Stücke, P. Numerical investigation of cavitation flow in journal bearing geometry. vol. 45 of *EPJ Web of Conferences* (EDP Sciences, 2013). DOI: 10.1051/epjconf/20134501081.

Publication 2

Cavitation estimates by orbit prediction of a journal bearing - finite element modelling and experimental studies

Published in *TRIBOLOGIA - Finnish Journal of Tribology 1.*

Accepted for publishing on February 1, 2015.

CAVITATION ESTIMATES BY ORBIT PREDICTION OF A JOURNAL BEARING - FINITE ELEMENT MODELLING AND EXPERIMENTAL STUDIES

C.K. Christiansen[1]*, P. Klit[1], J.H. Walther[1,2], A. Vølund[3]

[1]Department of Mechanical Engineering, Technical University of Denmark, Nils Koppels Allé, bld. 404, 2800 Kgs. Lyngby, Denmark.
[2]Computational Science & Engineering Laboratory, ETH, Clausiusstrasse 33, Zürich, CH-8092, Switzerland.
[3]MAN Diesel & Turbo, Teglholmsgade 41, 2450 Copenhagen SV, Denmark.

ABSTRACT

The paper presents a two-sided approach to establish understanding of the cavitation phenomenon in dynamically loaded journal bearings, more specifically the engine bearings of large two-stroke marine diesel engines. One disadvantage of the journal bearing is the converging-diverging geometry making it prone to cavitation which again affects the load carrying capacity of the bearing. In combustion engines the journal bearing plays a vital role especially as main and crosshead bearings transmitting the combustion forces. Those forces vary highly during one combustion cycle which is further influencing the load carrying capacity and ultimately the chances of fatal shaft-sleeve contact. By solving Reynolds equation numerically using finite elements and incorporating a cavitation algorithm, the dynamic coefficients can be used to establish the journal orbit for a given bearing and load pattern. Validation of the results is done against the Ruston and Hornsby 6VEB-X Mk III engine. Besides the numerical investigations a cavitation test rig has been developed. With this rig it is possible to generate cavitation under controlled conditions in terms of load/eccentricity and rotational speed. The development of cavitation in time in terms of position and distribution can be visually recorded.

Keywords: Cavitation, journal bearing, Finite Element, journal orbit, test rig.

*Corresponding author: Christian Christiansen (chkch@mek.dtu.dk).

INTRODUCTION

Journal bearings are used in a wide range of applications due to their simplicity and derived low cost but also a reasonable load carrying capacity. On the other hand, one of the most often mentioned disadvantages of the journal bearing is the converging-diverging geometry making it prone to cavitation. The general concepts of bearing cavitation are outlined in the thorough review of Dowson and Taylor [1]. In short two types of cavitation exists; gaseous cavitation and vaporous cavitation. Gaseous cavitation occurs from the release of entrained air in the lubricant being released at pressures equal to, or below, the saturation pressure of the lubricant. Vaporous cavitation on the other hand, is governed by the vapour pressure such that the lubricant starts boiling even at low temperatures, when the pressure drops below the vapour pressure. This phenomenon is what is known from a very broad range of areas; ship propellers being eroded on the surface, medical care and cleaning applications by the formed shock waves etc. [2].

For typical lubricants the saturation pressure is just sub-atmospheric whereas the vapour pressure is much closer to zero. Hence, the gaseous cavitation will occur first and work as a limiter, such that vaporous cavitation is very unlikely to occur for statically loaded journal bearings. This is not the case for a dynamically loaded bearing [1]. Here bubbles are forming in the boiling lubricant and the vaporous cavitation is characterised by the bubbles collapsing violently, blasting the surface yielding pressures in the order of

$\mathbf{10^8}$ **Pa** [3]. While the gaseous cavitation process itself is rather harmless compared to the vaporous one, the formation and/or concentration of released bubbles reduces the load carrying capacity locally, due to a decreased filling ratio, i.e. ratio between lubricant and vapour.

For dynamically loaded bearings as found in reciprocating machinery this reduction of load carrying capacity is of great importance. The reduction might lead to fatal journal-bearing housing contact, which will be revealed in a journal orbit plot. Booker used the mobility method in 1965 and 1971 to predict the orbit [4,5]. Adapting the concepts from stability and vibration analysis, Lund and Thomsen found that the dynamic coefficients revealed the behaviour of a statically loaded bearing using finite differences [6]. Klit and Lund developed a finite element formulation in the 1980's for obtaining the dynamic coefficients at an instant in time for a statically loaded bearing [7]. With very little effort these coefficients could be integrated in time to predict an entire orbit as shown with analytical coefficients in an unpublished paper by Klit and Vølund [8]. For evaluating new methods, the Ruston and Hornsby 6VEB-X Mk III 4-stroke diesel engine has become a widespread benchmark case over the years [5,9,10].

Although the orbit has been available for a journal bearing for 50 years with the mobility method, this method is limited to ideal bearings without grooves and other irregularities. The present work will show the application of the finite element method to obtain the journal orbit for a dynamically loaded journal bearing, and hence allow for a complex bearing design including grooves and inlets of various geometries by using the adaptability of the finite element method. Within the finite element model various cavitation models can be applied. For this work the half-Sommerfeld model is used for simplicity.

THEORY

Due to the non-linear relations between forces and journal position in Reynolds equation an iterative procedure is required to obtain the journal orbit corresponding to a complete load cycle. Based on a sequence of local force equilibria, a time-integration scheme sums up the contributions, yielding the journal orbit.

The theory is to a large extent similar to the one used by Klit and Lund [8]. However, where they assumed no whirling, it is included in the present work to account for the dynamic effects. The final equations will enable the prediction of the journal orbit for a sequence of loads, given at e.g. 2° of crank rotation.

The pressure distribution in the bearing is described by Reynolds equation. This work uses the non-dimensional version indicated by the bar notation:

$$\frac{\partial}{\partial\theta}\left(\bar{h}^3\frac{\partial\bar{p}}{\partial\theta}\right)+\frac{\partial}{\partial\zeta}\left(\bar{h}^3\frac{\partial\bar{p}}{\partial\zeta}\right)=\frac{\partial\bar{h}}{\partial\theta}+\frac{2\nu}{\omega}\frac{\mathrm{d}\bar{h}}{\mathrm{d}\tau} \qquad (1)$$

With $\boldsymbol{\theta}$ being the circumferential coordinate (from zero film thickness), $\bar{\boldsymbol{h}}$ is film thickness, $\bar{\boldsymbol{p}}$ is pressure, $\boldsymbol{\zeta}$ is axial coordinate, $\boldsymbol{\nu}$ is a parameter of unit $\mathbf{rad/s}$, $\boldsymbol{\omega}$ is angular velocity (of crankshaft) and $\boldsymbol{\tau}$ is time. The film thickness can be expressed as:

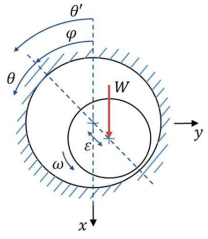

Figure 1. The journal bearing geometry in the global coordinate system $(\boldsymbol{x},\boldsymbol{y})$. $\boldsymbol{\theta'}$*is the global film coordinate,* $\boldsymbol{\theta}$ *the local film coordinate,* $\boldsymbol{\varphi}$ *is the attitude angle,* $\boldsymbol{W}$ *is imposed load,* $\boldsymbol{\varepsilon}$ *is eccentricity,* $\boldsymbol{\omega}$ *is angular velocity.*

$$\bar{h} = 1 + \varepsilon\cos\theta = 1 + \varepsilon\cos(\theta' - \varphi) = 1 + \bar{x}\cos\theta' + \bar{y}\sin\theta' \quad (2)$$

Where θ' is the film angle from the vertical axis and φ is the attitude angle and $\bar{x}, \bar{y}$ can be expressed on the form $\bar{x} = \bar{x}_0 + \Delta\bar{x}$, i.e. a stationary term and a perturbation.

Klit and Lund used the perturbation method to analyse the influence of shaft position $(\Delta\bar{x}, \Delta\bar{y})$ and velocity $(\Delta\dot{\bar{x}}, \Delta\dot{\bar{y}})$ on the dynamic properties of the shaft. Define a perturbed pressure:

$$\bar{p} = \bar{p}_0 + \Delta\bar{x}\bar{p}_1 + \Delta\bar{y}\bar{p}_2 + \Delta\dot{\bar{x}}\,\bar{p}_3 + \Delta\dot{\bar{y}}\,\bar{p}_4 \quad (3)$$

With Eq. (3) five functionals can be derived. These functionals serve as the basis for the finite element equations for solving $\bar{p}_i, i = 0, 1, \dots, 4$. Considering one element the equations become:

$$-\int_A \left(-\bar{h}_0^3\left[\left(\frac{\partial N}{\partial\theta}\right)^T\left(\frac{\partial N}{\partial\theta}\right) + \left(\frac{\partial N}{\partial\zeta}\right)^T\left(\frac{\partial N}{\partial\zeta}\right)\right]\bar{p}_i + RHS\right) dA = 0 \quad (4a)$$

$$RHS = \begin{cases} \left[\bar{h}_o + \frac{2\nu}{\omega}(\dot{\bar{x}}_0\sin\theta' - \dot{\bar{y}}_0\cos\theta')\right]\frac{\partial N^T}{\partial\theta} & \text{for } \bar{p}_0 \\ -3\bar{h}_o^2\cos\theta'\left[\left(\frac{\partial N}{\partial\theta}\right)^T\left(\frac{\partial N}{\partial\theta}\right) + \left(\frac{\partial N}{\partial\zeta}\right)^T\left(\frac{\partial N}{\partial\zeta}\right)\right]\bar{p}_0 & \\ \quad + \cos\theta'\left(\frac{\partial N}{\partial\theta}\right)^T & \text{for } \bar{p}_1 \\ -3\bar{h}_o^2\cos\theta'\left[\left(\frac{\partial N}{\partial\theta}\right)^T\left(\frac{\partial N}{\partial\theta}\right) + \left(\frac{\partial N}{\partial\zeta}\right)^T\left(\frac{\partial N}{\partial\zeta}\right)\right]\bar{p}_0 & \\ \quad + \sin\theta'\left(\frac{\partial N}{\partial\theta}\right)^T & \text{for } \bar{p}_2 \\ \frac{2\nu}{\omega}\sin\theta'\frac{\partial N^T}{\partial\theta} & \text{for } \bar{p}_3 \\ -\frac{2\nu}{\omega}\cos\theta'\frac{\partial N^T}{\partial\theta} & \text{for } \bar{p}_4 \end{cases} \quad (4b)$$

Where N is the vector containing the element shape functions. The resulting system of equations is fast to solve as the stiffness matrix on the left hand side only needs to be assembled once for each time step (Eq. 4a). The term RHS specifies the five different right hand sides in the equation system.

After obtaining $\bar{p}_i$ the load carrying capacity and dynamic coefficients can be found from:

$$\begin{Bmatrix} f_x \\ f_y \end{Bmatrix} = \frac{6\pi}{L/D}\int_0^{L/D}\int_0^{2\pi}\bar{p}_0\begin{Bmatrix} -\cos\theta' \\ -\sin\theta' \end{Bmatrix} d\theta d\zeta \quad (5a)$$

$$\begin{Bmatrix} \bar{K}_{xx} \\ \bar{K}_{yx} \end{Bmatrix} = \frac{6\pi}{L/D}\int_0^{L/D}\int_0^{2\pi}\bar{p}_1\begin{Bmatrix} -\cos\theta' \\ -\sin\theta' \end{Bmatrix} d\theta d\zeta \quad (5b)$$

$$\begin{Bmatrix} \bar{B}_{xx} \\ \bar{B}_{yx} \end{Bmatrix} = \frac{6\pi}{L/D}\int_0^{L/D}\int_0^{2\pi}\bar{p}_3\begin{Bmatrix} -\cos\theta' \\ -\sin\theta' \end{Bmatrix} d\theta d\zeta \quad (5c)$$

Here L/D is the length/diameter ratio of the bearing. Using $\bar{p}_2$ and $\bar{p}_4$, respectively, yields the stiffness $\bar{K}_{xy}$ and $\bar{K}_{yy}$ and damping $\bar{B}_{xy}$ and $\bar{B}_{yy}$. For the journal orbit, only the damping coefficients are required. For the imposed load W_x, W_y in step k, the journal velocity is found from solving Eq. (6) in iterations numerated by j.

$$\begin{bmatrix} \bar{B}_{xx_j} & \bar{B}_{xy_j} \\ \bar{B}_{yx_j} & \bar{B}_{yy_j} \end{bmatrix}\begin{Bmatrix} \Delta\dot{\bar{x}}_j \\ \Delta\dot{\bar{y}}_j \end{Bmatrix} = \begin{Bmatrix} \bar{W}_{x_k} - f_{x_j} \\ \bar{W}_{y_k} - f_{y_j} \end{Bmatrix} \quad (6)$$

Please, note that formally $f_{i_j} = f_{i_j}(\bar{x}_k, \bar{y}_k, \dot{\bar{x}}_{k_j}, \dot{\bar{y}}_{k_j})$. Now the new shaft velocity is:

$$\dot{\bar{x}}_{k_{j+1}} = \dot{\bar{x}}_{k_j} + \Delta\dot{\bar{x}}_j \quad (7a)$$
$$\dot{\bar{y}}_{k_{j+1}} = \dot{\bar{y}}_{k_j} + \Delta\dot{\bar{y}}_j \quad (7a)$$

The velocity is adjusted by solving Eqs. (4)-(7) iteratively. Let k designate the load step, the convergence criterion is then chosen as a norm of the type:

$$\frac{|W_{x_k} - f_{x_j}| + |W_{y_k} - f_{y_j}|}{|W_{x_k}| + |W_{y_k}|} < \text{tol} \simeq 10^{-5} \quad (8)$$

After convergence is obtained, a first-order forward Euler method is used to step forward in time to the imposition of load $k + 1$:

$$\bar{x}_{k+1} = \bar{x}_k + \Delta t\dot{\bar{x}}_k \quad (9a)$$
$$\bar{y}_{k+1} = \bar{y}_k + \Delta t\dot{\bar{y}}_k \quad (9b)$$

In this way the journal orbit after one load cycle is of course affected by the initial guess for the journal position and velocity. Going through the load cycle consecutively will lead to steady state, usually after a few cycles.

BENCHMARK CASE

As a validation case, the widely used Ruston and Hornsby 6VEB-X Mk III engine is used, see further [5,9]. Fig. 2 shows the setup adapted from [5]. The loads shown in Fig. 3 are given for one land of the connecting rod big end bearing (shown here with cubic interpolation from 10° crank rotation to 1°) which is having one circumferential groove. It is assumed the boundary conditions on this half-width bearing can be considered to be atmospheric pressure. The remaining used data are listed in Table 1.

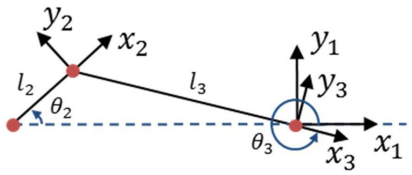

Figure 2. Geometry of crank rod-connecting rod assembly (redrawn from Booker, [5]).The coordinate systems 2 and 3 are following the crank and connecting rod, respectively, whereas the coordinate system 1 is aligned to the piston.

Table 1. Dimensions and properties of the Ruston and Hornsby 6VEB-X Mk III connecting rod bearing (from Booker, [5]).

Parameter	Value
l_2	0.1841 m
l_3	0.7823 m
D	0.2032 m
L	0.0572 m
C	$82.55 \cdot 10^{-6}$ m
μ	0.015 Pa · s
RPM	300

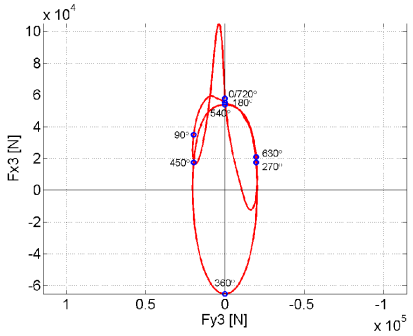

Figure 3. Load diagram obtained from data by Booker, [5]. Cubic interpolation is applied from 10° crank rotation to 1°.

RESULTS

The main result is the direct benchmark between literature and the present work with regards to the journal orbit. Fig. 4 is the solution by Campbell et al from their review [9, Fig. 9b], where it is one of a dozen solutions computed from graphical, mobility and finite difference methods by various institutions as well as experimental results. The minimum film thickness is a key parameter of interest and found to be 5.5 µm at 277° after top dead centre (TDC). Campbell et al reports this to be in the interval 2.3 µm-12.9 µm and 270°-290°. The arbitrary initial guess requires as expected in Section 2, a number of consecutive runs of the load cycle. Using the bearing centre as initial location $((\bar{x}, \bar{y}) = (0,0))$, a stable orbit is found within two runs.

Fig. 5 shows the present work and qualitatively agreement is obtained. It is noted that the position of the indicated angles and the sharp turn seen between

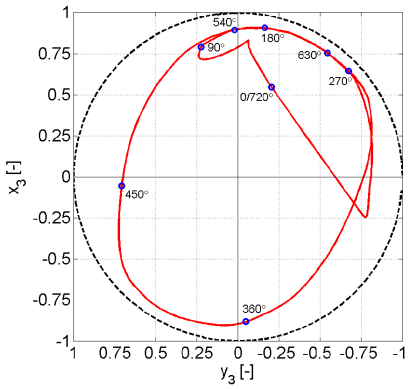

Figure 4. Journal orbit by Campbell et al (1967) made from the short bearing solution and the graphical method [9].

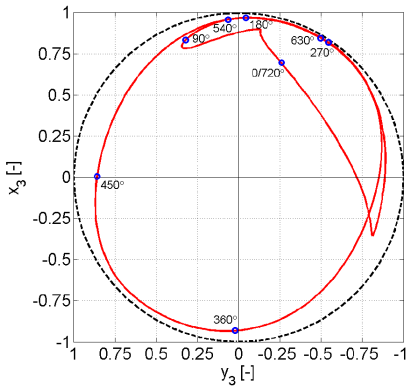

Figure 5. Journal orbit for present code with 60 x 16 elements.

630° and 720° is changing from computation to computation in the work of Campbell et al, such that the results contain some influence from the models used. The minimum film thickness of 0.8 µm is located at 275° after TDC. A mesh of 30 x 8 triangular elements is used and this seems to be sufficient to predict the nature of the orbit (very small changes occur with 45 x 12 or 60 x 16 elements). However, the minimum film thickness increases from 0.8 µm over 1.2 µm to 1.3 µm and changes location from 275° after TDC to 271° after TDC when increasing the resolution. Unsurprisingly, it appears that the low-order element mimics the nature of the solution with few elements, but accurate values require a high number of elements.

With the journal orbit found, it is easy to calculate the volume of the cavitated areas from the local film thickness and hence obtain knowledge useful for the specification of the flow rates required for an inlet nozzle. From Fig. 6 and the principle of mass conservation the following relation can be established:

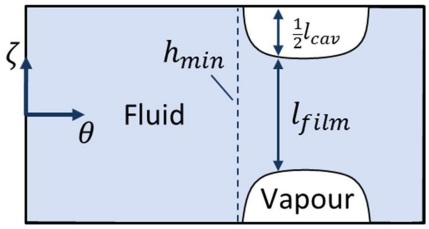

Figure 6. Sketch of two cavitated areas (symmetry around $\boldsymbol{\zeta = 0}$) and their size due to mass conservation.

$$\boldsymbol{l_{cav} = L\left(1 - \frac{\bar{h}_{min}}{\bar{h}_{film}}\right)} \qquad (10)$$

The cavitated volume is now simply the arc length times length times height, or in non-dimensional terms:

$$\boldsymbol{\bar{v}_{cav} = \Delta\theta\zeta\left(\bar{h}_{film} - \bar{h}_{min}\right)} \qquad (11)$$

The dimensional expression is thus:

$$\boldsymbol{v_{cav} = \bar{v}_{cav} \cdot R^2 C} \qquad (12)$$

The cavitated volumes are plotted as a function of the crank ankle degree (CAD) for one combustion cycle in Fig. 7. Here on the other hand, a higher resolution for the mesh is required to eliminate fluctuations in the volumes due to abrupt changes in what element, and thus film height, is seen as cavitated or not. Recall, that one element spans over 12° of the bearing circumference

for the coarse mesh and only 6° for the fine mesh. Fig. 7 will serve as tool for pinpointing the angular position(s) where improved filling might influence the dynamic properties and hence journal orbit significantly. Due to the application of the half-Sommerfeld model, the *full* film history is not known. Areas of full film are treated with 100% load carrying capacity, while cavitated areas have no load carrying capacity. Thus, the angular difference $\boldsymbol{\alpha}$ between the starting point of film rupture for half-Sommerfeld (180°) and a complete cavitation model - e.g. by applying Reynolds boundary conditions $\mathbf{d}p/\mathbf{d}\vec{n} = \mathbf{0}$, where $\vec{n}$ is the normal vector to the film front - (rupture at 180°+ $\boldsymbol{\alpha}$), is not accounted for with a weight between 0 and 1. In other words filling of cavitated areas occurs infinitely fast in this work and no intermediate stage exists.

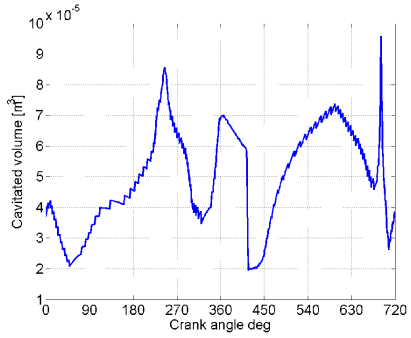

Figure 7. Cavitated volumes as function of CAD for present code with 60 x 16 elements.

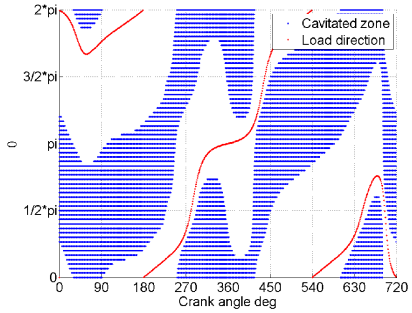

Figure 8. Map of cavitated area as function of CAD for present code with 60 x 16 elements.

Another way to interpret the journal orbit of Fig. 5 is given in Fig. 8. Here cavitated zone is plotted in blue and the direction of the imposed load of Fig. 3 is plotted in red. It is interesting to see the dynamics of the bearing coupled with the imposed load. Notice the first large change in load after a few degrees of crankshaft rotation is not shown as dramatic as the rapid change in magnitude and sign occurring around 270° and around 450°. The sharp turn between 630° and 720° is also recognised on the plot, showing how the rapid change in load direction dictates a very rapid change, such that e.g. $\boldsymbol{\theta = \pi/2}$ undergoes a transition from cavitated to non-cavitated and back to cavitated within a short period of time. This is also represented by the spike in Fig. 7.

CAVITATION TEST RIG

To validate the numerical findings a test rig has been developed and manufactured. Entitled Cavitation Test Rig (CTR) the idea is to monitor the formation of cavitation tongues, the so-called striations inside an acrylic bearing, see Fig. 9. The bearing is supported by a steel sleeve including an inspection slot. The 3 degrees of freedom necessary to follow a locus curve are ensured by mounting the shaft on a hinged table, whereas the bearing is stationary. The shaft is loaded with a hydraulic cylinder capable of both static and dynamic loads.

In Fig. 10 a photo of the preliminary operation is shown for a static load and the formation of three striations is clearly visible. This is meant as an example demonstration of the ability to generate cavitation in desired locations for visual studies. The numerical results demonstrated in Fig. 5 would only be reproducible with the data logging equipment illustrated in Fig. 9.

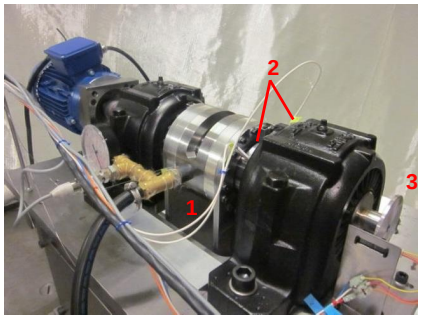

Figure 9. Cavitation test rig (CTR) shown with oil inlet (1), distance sensors (2) and tachometer (3). Load arrangement is hidden below the set-up. The inspecting slot is visible just above the inlet hose with the manometer.

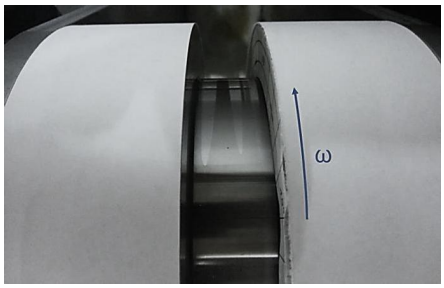

Figure 10. Example on cavitation taking the form of tongues or 'striations' seen in white.

CONCLUSIONS

The crude half-Sommerfeld model assumption proves sufficient to mimic the behaviour of a journal bearing exposed to a dynamic load cycle, when comparing to a classical benchmark case of the literature.

The used low-order finite element scheme captures the orbit in a qualitative way with few elements, but quantitatively results needs a fine mesh.

From the predicted journal orbit the volume (and location) of the cavitated areas can be calculated, improving the basis for decision in terms of inlet nozzle and groove design.

A test rig for monitoring cavitation in a journal bearing under controlled conditions has been developed. The preliminary results obtained during run-in seem promising.

ACKNOWLEDGEMENTS

Thanks to A. Jørgensen-Juul and K.F. Kristensen together with scientific engineer N.S. Jensen for the work on the test rig, especially the pictures of cavitation.

The project is financially supported by the EU project HERCULES-C.

REFERENCES

1. D. Dowson, C.M. Taylor, Cavitation in Bearings. Ann. Rev. Fluid Mech. (11) (1979), pp. 35-66.
2. D. Lohse, Bubble Puzzles, Physics Today, February 2003, pp.36-41.
3. M.S. Plesset, R.B. Chapman, Collapse of an initially spherical vapour cavity in the neighbourhood of a solid boundary, J. Fluid Mech. (47), part 2, 1971, pp. 283-290.
4. J.F. Booker, Dynamically-Loaded Journal Bearings: Mobility Method of Solution, Transactions of the ASME, 1965, pp.537-546.
5. J.F. Booker, Dynamically-Loaded Journal Bearings: Numerical Application of the Mobility Method, Transactions of the ASME, 1971, pp.168-174.
6. J.W. Lund, K.K. Thomsen, A Calculation Method and Data for the Dynamic Coefficients of Oil-lubricated Journal Bearings, Topics in Fluid Film Bearing and Rotor Bearing System Design and Optimization, ASME publ., 1978, pp. 1-28.

7. P. Klit, J.W. Lund, Calculation of the Dynamic Coefficients of a Journal Bearing, Using a Variational Approach, Journal of Tribology, (108) 1986, pp.421-424.
8. P. Klit, A. Vølund, Shaft Center Orbit for Dynamically Loaded Journal Bearings, DTU Mechanical Engineering, 2000, (unpublished).
9. J. Campbell, P.P Love, F.A. Martin, S.O. Rafique, Bearings for Reciprocating Machinery: A Review of the Present State of Theoretical, Experimental and Service Knowledge, Proc Instn Mech Engrs 1967-68, (182), Part 3A, pp. 51-70.
10. J.D.C. McIvor, The Analysis of Dynamically Loaded Flexible Journal Bearings Using Higher-Order Finite Elements, PhD thesis, Kings College London, 1988.

The paper was partially presented at NORDTRIB2014, Aarhus, Denmark.

Publication 3

Investigation of journal orbit and flow pattern in a dynamically loaded journal bearing

Draft intended for Tribology International.

Investigation of journal orbit and flow pattern in a dynamically loaded journal bearing

Christian Kim Christiansen[a,d,*], Jens Honore Walther[a,b], Peder Klit[a], Anders Vølund[c]

[a] *Department of Mechanical Engineering, Technical University of Denmark, Nils Koppels Allé, bld. 404, 2800 Kgs. Lyngby, Denmark*
[b] *Computational Science & Engineering Laboratory, ETH, Clausiusstrasse 33, Zürich, CH-8092, Switzerland*
[c] *MAN Diesel & Turbo, Teglholmsgade 41, 2450 Copenhagen SV, Denmark*
[d] *Center for Bachelor of Engineering Studies, Technical University of Denmark, Lautrupvang 15, 2750 Ballerup, Denmark*

Abstract

Traditionally, the hydrodynamic journal bearing has been investigated using Reynolds equation; a simplified 2D approach demonstrated to yield good results in the bearing region by numerous works. Over the last decades, the advent of more computational power has made a full 3D Navier-Stokes solution feasible. This enables a better modelling of details like inlet and supply grooves.

A comparison of the two approaches is performed by investigation of two groove designs (point and circumferential groove) on a bearing with length/diameter ratio of 0.5 exposed to a sinusoidal load pattern. Comparing pressure distributions, journal orbit and frictional losses it is clear that on an overall basis good agreement is obtained, but the 2D solution possess problems modelling the circumferential groove. Furthermore, advantage of the 3D solution is taken to study the influence of the groove design on the flow field.

Keywords:
hydrodynamic, cavitation, journal, simulation

*Corresponding author
Email address: chkch@dtu.dk (Christian Kim Christiansen)

1. Introduction

Ever since Reynolds described the governing equation of hydrodynamic lubrication in 1886 [1], computing the solution to what has become known as the Reynolds equation has occupied the scientific branch with roots in the fields of engineering and mathematics.

Being a partial differential equation, no analytical solution exists. For his paper, Reynolds applied assumptions on an infinitely long bearing and a series expansion to perform the integration. This would only work for low eccentricity ratios (< 0.5). With the advent of a particular substitution in 1904 Sommerfeld was able to obtain a closed form solution to the case Reynolds had tried [2]. In 1952 Ocvirk used the opposite approach and assumed the bearing to be infinitely narrow [3]. These two approaches have one major drawback, despite softening the requirements to what is considered infinitely long and short, that is most bearings fall between those definitions. For such bearings only a numerical solution is possible.

With the appearance of computers occurring after World War II, the numerical methods became more and more feasible, especially for solving 1- and 2D problems like Reynolds equation. Simultaneously, with the continuously improving computational power being available, focus turned onto improved modelling of the film rupture boundaries independently started by Swift and Stieber in the 1930's [4, 5]. As the extent of the film has proven important in terms of the bearing's dynamic properties, a lot of attention has been put into the development of theoretical models and their numerical implementation [6, 7]

During the last decades the ever-increasing trend in computing power have made three dimensional analysis possible. Obvious analysis would include the pressure distribution, but due to the computational heavy task of solving the full Navier-Stokes, more advanced problems like thermal distribution in lubricant [8] and modeling of Bingham lubricants [9].

Recently, a group of German researchers have have used the open source CFD code OpenFOAM for investigations on journal bearings [10, 11, 12].

In this paper, a comparison between a simple and traditional, but fast, finite element code solving Reynolds equation and a slower, but physically more correct Navier-Stokes based finite volume code is performed. The latter will become of importance when investigating more complex designs for bearing feed grooves violating the typical assumptions leading to Reynolds equation.

2. Methodology

Being a problem of fluid dynamics, the Navier-Stokes and continuity equations are the governing relations for the case of hydrodynamic lubrication (assuming no body forces):

$$\rho\left(\frac{\partial \mathbf{u}}{\partial t} + \mathbf{u}\cdot\nabla\mathbf{u}\right) = -\nabla p + \nabla\cdot\mathbf{T} \tag{1}$$

$$\frac{\partial \rho}{\partial t} + \nabla\cdot(\rho\mathbf{u}) = 0 \tag{2}$$

Here ρ is density, $\mathbf{u}$ is the velocity vector, p is pressure, $\mathbf{T}$ is the deviatoric stress tensor ($\mathbf{T} = \nabla\cdot(\mu(\nabla\mathbf{u} + (\nabla\mathbf{u})^T)) + \nabla(-2/3\mu\nabla\cdot\mathbf{u})$ with μ being the dynamic viscosity).

The traditional approach for solving the hydronamic lubrication problem is a simplification to the Navier-Stokes equations. Applying the assumptions of a thin lubricant film and isothermal conditions to the Navier-Stokes equations, Reynolds equation is found [1]. Here, it is shown in its non-dimensional form as applied to the numerical implementation:

$$\frac{\partial}{\partial\theta}\left(\bar{h}^3\frac{\partial\bar{p}}{\partial\theta}\right) + \frac{\partial}{\partial\zeta}\left(\bar{h}^3\frac{\partial\bar{p}}{\partial\zeta}\right) = \frac{\partial\bar{h}}{\partial\theta} + \frac{2\omega^*}{\omega}\frac{\mathrm{d}}{\mathrm{d}\bar{t}}\bar{h} \tag{3}$$

Here θ and ζ is circumferential and axial directions, respectively, $\bar{h}$ is film thickness, ω is angular (relative) velocity, ω^* is a characteristic angular velocity and $\bar{t}$ is time. Please, note that this version of Reynolds equation is incompressible. The non-dimensionalisation is shown in Appendix A.

Both approaches (Equations (1)-(2) and Equation (3)) predict an increase in pressure, followed by a decrease to the same pressure magnitude, but with negative sign, due to the converging-diverging geometry. Besides for submerged and/or very lightly loaded bearings, this anti-symmetry is destroyed due to dissolution and cavitation effects. The cavitation modelling in this paper, is basically what is known as the half-Sommerfeld treatment, but instead of neglecting all negative pressures, only pressures below the saturation pressure p_{sat} is modified. It is a very simplified consideration to cavitation and does not preserve the continuity through the cavitated zone.

To solve the dynamic lubrication problem, the two approaches deviates as follows:

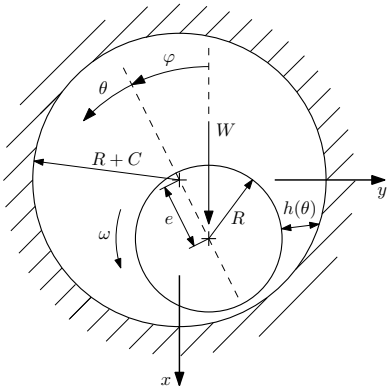

Figure 1: Bearing geometry and imposed boundary conditions. Axial coordinates z and ζ, with ζ from Equation (3), is pointing out of the plane.

2.1. Discretisation

2.1.1. Finite volume

Equations (1)-(2) are discretised by a finite volume scheme and then solved with the commercial code STAR-CCM+ version 10.02. A full 3D solution is obtained. The dynamic squeeze term $\mathrm{d}h/\mathrm{d}t$ is modelled with a build-in 6-DOF solver applying Newton's second law to relate surface forces (lift) and external forces (imposed loads) with translations and rotations [13].

2.1.2. Finite element

Equation (3) is solved with a purpose written, MATLAB based finite element code using triangular first order elements. This solution is only 2D (no variation in thickness direction). The dynamic squeeze term $\mathrm{d}h/\mathrm{d}t$ is modelled with Lund's perturbation method [14] and the time integration is a simple Euler method. Further details on the implementation and a verification are given in [15].

3. Numerical setup

3.1. The journal bearing

The bearing chosen for the simulations are described by Table 1 and illustrated in Figures 2 and 3. Figure 2 shows the point groove designated 'Case 1' and Figure 3 shows the circumferential groove named 'Case 2'. In

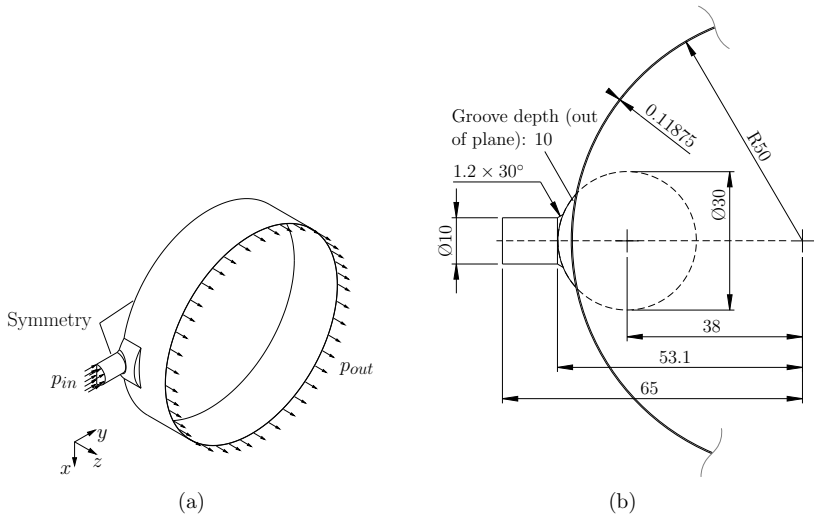

Figure 2: Simple inlet groove. (a) Bearing geometry and imposed boundary conditions. Refer to Table 1 for values. (b) Specification of point groove (Case 1) - dimensions in mm.

either case, symmetry is exploited in the radial plane and it is assumed the bearing housing is infinitely stiff. Lubricant is fed in at the inlet and exiting the bearing at the free edge of the bearing. The pressure conditions are listed in Table 1 as well as the rotational velocity of the journal. All walls are modelled with no-slip condition.

As imposed load ($W_x(t)$) on the bearing, a sine function is chosen, see Equation (4).

$$W_x(t) = \frac{1}{2}\left[\sin\left(10\pi \cdot t - \frac{\pi}{2}\right) + 1\right] \cdot 3 \times 10^3\,\mathrm{N} \tag{4}$$

To simplify the computations, a shift is applied such that $W_x(0) = 0$ and $W_x(t) \geq 0$. These choices have two advantages; *i)* it eliminates the need for ramping up the load as this is built into the function itself and *ii)* the positive load only forces the journal downwards, simplifying the requirements to the computations as the orbit will be restricted compared to an sign-alternating function. Item *ii)* also simplifies the loading arrangement in case

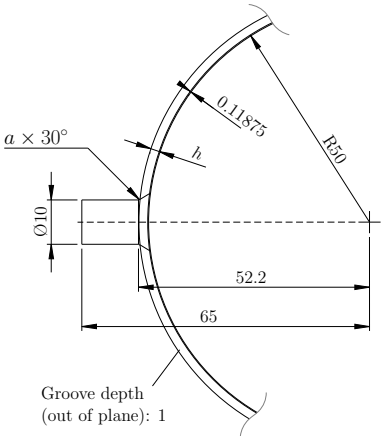

Figure 3: Specification of circumferential groove (Case 2) - dimensions in mm. The groove height is varied as $h = \{2, 0.5, 0.1\}$ mm, hence the variable a for the chamfer.

of an experimental setup, as only tensional *or* compressional loading will be required.

The excitation frequency is chosen to be half the rotational frequency to have a time-varying force not being too aggressive with regards to computational stability, but still allow for some revolutions of the bearing within a manageable time frame. Total simulated time (t_{end}) is chosen, by setting $t_{end} = 0.4\,\mathrm{s}$, such that two periods of the load function is imposed on the bearing during four revolutions. In this way a periodic solution for the journal orbit should be obtained, even from an arbitrary starting position.

The lubricant is considered to be Newtonian and with the properties given in Table 2.

3.2. Finite volume

The two main advantages for the application of a commercial code like CCM+ is the ability to choose between several approaches to a numerical representation of the physical problem. Particularly, this relates to the cavitation modelling where two methods have been investigated. Also the mesh generation in the thin film is non-trivial.

For the simulations both first and second order upwind schemes have been used for the discretisation of the convection term. Likewise, the grid fluxes

Table 1: Dimensional and operational parameters for the journal bearing.

Parameter	Symbol	Value	Unit
Length	L	50	mm
Diameter	D	100	mm
Clearance (radial)	C	118.75	µm
Mass moment of inertia	I_{zz}	2×10^{-3}	$\mathrm{kg\,m^2}$
Rotational speed	ω	600	RPM
Load (vertical)	W_x	$W_x(t)$[a]	N
Inlet pressure	p_{in}	2×10^5	Pa
Outlet pressure	p_{out}	1×10^5	Pa

[a] See Equation (4).

Table 2: Lubricant properties.

Parameter	Symbol	Value	Unit
Dynamic viscosity	μ	0.071	$\mathrm{Pa\,s}$
Saturation pressure	p_{sat}	90×10^3	Pa
Density	ρ_0	885	$\mathrm{kg/m^3}$
Speed of sound	v_s	1300	m/s

are integrated in time using both first and second order methods.

3.2.1. Time stepping

Due to the constantly varying mesh, a varying time step is preferred over a constant time step. With numerical stability in mind the desired Courant number $\mathrm{CFL} = U\Delta t/\Delta x$ is specified as $\mathrm{CFL} = 1$. Further stability is sought introduced by defining an interval for the admissible time step $t \in [1 \times 10^{-6}\,\mathrm{s}, 5 \times 10^{-5}\,\mathrm{s}]$ and averaging between the calculated (new) step and the current one, $t_{new} = \alpha t_{old} + (1 - \alpha)t_{new}$. The time range is chosen as to limit the Courant number to $\mathrm{CFL} \approx 1$ for the grid sizes and expected velocities during the simulation, and the averaging weight $\alpha = 0.5$.

3.2.2. Motion

As explained in Section 2, the motion is computed in a dynamic fluid body interaction (DFBI) fashion. With six degrees of freedom available (translation and rotation in all three directions), a set of limitations have to be

applied. Therefore, to mimic the bearing, only in-plane translation (x, y) is allowed, cf. Figure 2a. The rotation around z is specified as a velocity boundary condition on the journal wall.

3.2.3. Mesh

Despite a relatively simple geometry, the mesh generation is far from trivial. Constituted of a thin and a bulky part, in which, from theoretical expectations, various flow phenomena might occur, the bearing presents some difficulties.

Due to the non-linear problem, and hence iterative solution method, together with integration in time making the problem very computational demanding, much effort has been put into the optimisation of the mesh.

For better control of the meshing process, the bearing as seen in Figure 2a (Case 1), is split up into two groups; one for the film and one for the inlet groove (Case 2 is split into three; inlet pipe, groove and film). This makes it possible to obtain a suitable mesh taking advantage of the geometry.

Film. With the geometry being pre-dominantly thin, advantage of CCM+'s build-in thin mesher can be taken. It is an unstructured mesher that allows for a larger surface/thickness aspect ratio to minimise the cell count in circumferential and axial directions, and just as important, is the radial mesh being structured (layered). A total of 10 cells is used to resolve the radial direction. The total cell count is approximately 564,000 cells.

To reflect the calculated motions, the mesh is morphed. Specific cell quality parameters are monitored and works as stopping criteria to the simulation, if the mesh becomes too distorted. The applied mesh have proved quite robust and able to maintain an acceptable quality even with eccentricity ratios of $\varepsilon = e/C \approx 0.7 - 0.8$.

Groove. The inlet groove and pipe is meshed with an unstructured polyhedral due to the geometry, see Figure 4. Whereas the inlet pipe is expected to be dominated by a pipeflow, the groove is meshed to resolve a more complicated flow. Two prism layers are used to improve the accuracy near walls. The total cell count is approximately 55,000 cells.

3.2.4. Compressibility

To avoid numerical instabilities in STAR-CCM+ in connection with the 6-DOF solver, the lubricant is considered compressible. It appears that violent fluctuations in the coupled terms pressure field and journal translation

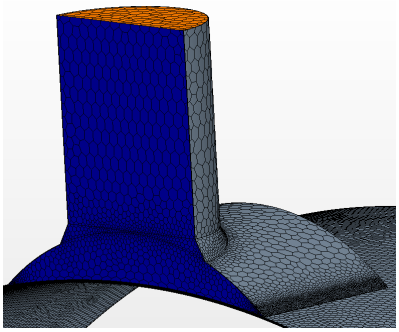

Figure 4: Finite volume mesh.

velocity is smoothed out by the damping influence of a compressible density. From the general equation of state, the density is a function of (local) relative pressure as follows:

$$\rho(p) = \rho_0 + \frac{p_{rel}}{v_s^2} \tag{5}$$

The relative pressure is defined as the difference between absolute and atmospheric pressure, $p_{rel} = p_{abs} - p_{atm}$ and v_s is the sonic speed of the lubricant. Studying the fraction p_{rel}/v_s^2 it is clear that for pressure values typical for journal bearings (50 MPa is high in this context), the fraction is $p/v_s^2 \approx 3\,\mathrm{kg/m^3}$, such that the lubricant is only weakly compressible ($\rho_0 = 885\,\mathrm{kg/m^3}$).

3.2.5. Cavitation

The modified half-Sommerfeld treatment is applied. Please, note this is not a standard model in CCM+, but the pressure solver allows a user specified value for the allowed minimum pressure. If the computed pressure in any cell drops below this threshold during the simulation, then the defined minimum values is assigned. The minimum value is changed from the default $1 \times 10^3\,\mathrm{Pa}$ (absolute pressure) to p_{sat}, see Table 2.

3.3. Finite element

Contrary to the finite volume scheme solving Navier-Stokes equation (Equation (1)), the finite element is a much simpler set-up due to Equation (3). The imposed load of Equation (4) is discretised for every 1° of

crank shaft rotation (CAD) to ensure a stable scheme due to the simple time integration. Thus, the time step is constant at $\Delta t = 2.78 \times 10^{-4}$ s.

The effect from the inlet is modelled onto the 2D domain by imposing inlet pressure on the affected nodes ($\pm 11.66^\circ$ from vertical center plane). This is done since the groove is much thicker than the surrounding film and hence not influenced by the pressure build-up suggested by Reynolds equation.

3.3.1. Motion

The motion of the journal is found from perturbations to a damper model of the journal. The damping coefficients relates to the forces and velocities in the manner:

$$\begin{Bmatrix} W_x - F_x \\ W_y - F_y \end{Bmatrix} = \begin{bmatrix} D_{xx} & D_{xy} \\ D_{yx} & D_{yy} \end{bmatrix} \begin{Bmatrix} \dot{x} \\ \dot{y} \end{Bmatrix} \tag{6}$$

Where W is the imposed load, F is the hydrodynamic load, D is the damping coefficients and $\dot{x}, \dot{y}$ is the journal velocities. As F is a function of the velocities $\dot{x}, \dot{y}$ this is done iteratively. For the next load step a first-order Euler method is applied: $x_{i+1} = x_i + \Delta t \cdot \dot{x}_i$. Please, refer to [15, 14] for further information.

3.3.2. Mesh

The mesh used in the finite element code is $\theta \times \zeta = n(30 \times 8)$ triangular and uniform elements, with $n = \{1, 1.5, 2\}$.

3.3.3. Cavitation

The simple cavitation model (SC) described above is also implemented in the finite element code.

4. Results

In all the portrayed cases, the journal is rotating with 600 RPM at the initial position $\varepsilon_x = \varepsilon_y = 0.1$. To distinguish between the finite element and finite volume discretisations and their subsets, the finite element is referred to by the resolution and for the finite volume the case number is used.

For Case 1 a mesh refinement study is carried out, together with general visualisation of the flow field in and around the point groove. Case 2 investigates the influence from a circumferential groove being roughly 1, 5 and 20 times the film height.

4.1. Pressure distribution

The pressure distribution of the four groove designs are shown in Figure 5 after one and a half load cycle ($t = 0.3\,\mathrm{s}$). Despite the differences in groove design, the pressure distributions are very similar. Most interesting is the fact that due to the load having its maximum value at this point, even the tallest of the circumferential grooves are experiencing high pressure and thus contributing to the load carrying capacity unlike ones initial expectations.

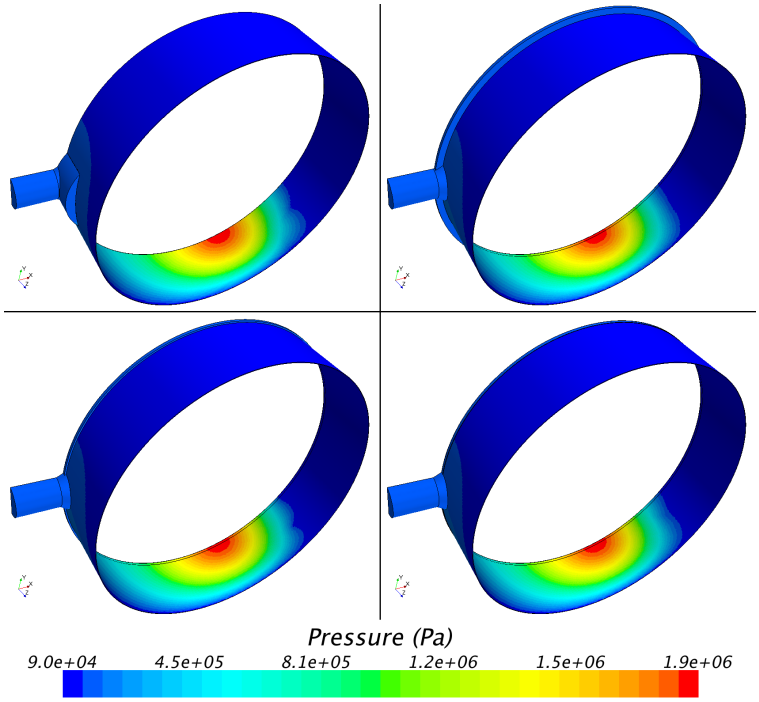

Figure 5: Pressure distribution of the four different groove designs; top row is Case 1.3 and Case 2.1 and bottom row is Case 2.2 and Case 2.3. Time $t = 0.3\,\mathrm{s}$ (maximum value of imposed load).

4.2. Journal orbits

The journal orbits for the two groove layouts are shown in Figure 6. In terms of convergence studies, subfigures (a) and (c) show very subtle

differences between the medium and fine mesh solutions represented by the red (medium) and green (fine) lines, whereas the coarse mesh represented in blue is slightly off. Also, the two discretisation methods predict very similar orbits, both in terms of magnitude and orbit shape.

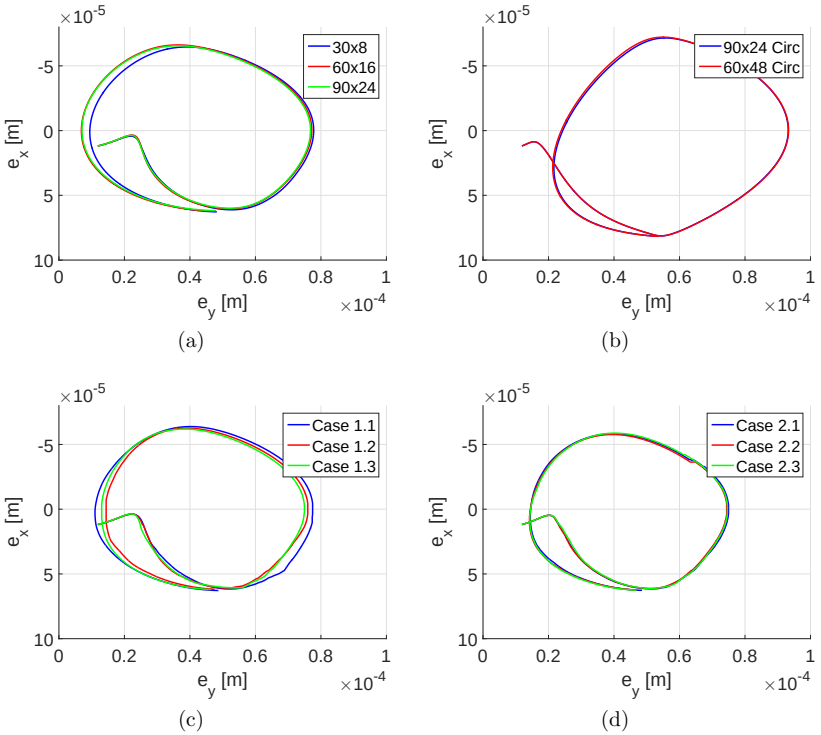

Figure 6: Journal orbits, left column is point groove (Case 1) and right column circumferential is groove (Case 2).

Based on the convergence of the orbit prediction, the medium case of 10 radial layers are used for the varying groove height of Case 2 in the finite volume discretisation. With the modelling of groove extent by assuming a uniform, practically hydrostatic, pressure boundary condition in the finite element discretisation, the three values of groove height are not 'seen' by the

finite element discretisation.

The consequences of the simplified approach taken to model the groove is clearly seen in Figures 6b and 6d. The general shape of the orbit is the same, but the position and magnitude of the orbit has moved relative to the initial position $\varepsilon_x = \varepsilon_y = 0.1$. As those results are very different from the previous findings, an axial refinement has been introduced to the finite element model to make sure only nodes being coincident with the groove position are included in the pressure boundary. However, it is clear from Figure 6b that the effect of the refinement is very little.

With the same overall settings to the mesh, the variable groove height orbit is predicted in Figure 6d. The orbit is very much identical to the mesh-wise corresponding Case 1.2 in Figure 6c. Both this behaviour as well as the general pressure distributions of Figure 5 indicates that the grooves possess some load carrying capacity, irrespective of their height. For both cases, the initial discrepancy described previously results in an upwards movement of the journal, until load equilibrium is met.

4.3. Friction loss

To quantify the suitability of the proposed bearing designs, friction loss is an obvious parameter.

$$\bar{M}_f = \frac{\pi}{L/D} \int_0^{L/D} \int_{\theta_1}^{\theta_2} \left(\frac{1}{\bar{h}} + 3\bar{h} \frac{\partial \bar{p}}{\partial \theta} \right) \mathrm{d}\theta \, \mathrm{d}\zeta \tag{7}$$

For the overall friction loss per revolution, the average frictional moment is used. In this work it is approximated with the trapezoidal rule. With the similar appearance of the various pressure distributions and journal orbits, only small deviations in the frictional moments are expected. Recall that Equation (7) relies on the film thichness $\bar{h}$ and pressure gradient $\partial\bar{p}/\partial\theta$. Hence, only a characteristic set of data are plotted in Figure 7.

The trend of the four cases are similar, but it is clear the deviation is caused in the first half of the intervals with increasing load and reaching its maximum very close to the midpoint of the interval. With the load curve being a sinusoidal function, this relates to areas with accelerating load increase (positive time derivative). Similarly, the second half of the interval with a decelerating load increment minimises the discrepancy and brings it to a low level for the entire interval of decreasing load. During the next load increase, the pattern repeats. The frictional losses for the first one and a

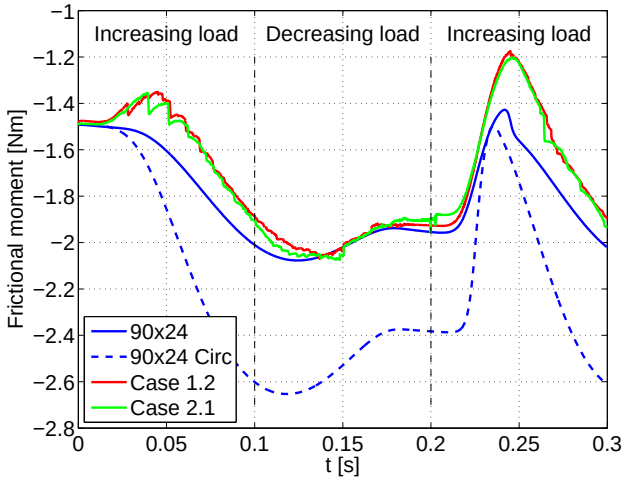

Figure 7: Frictional moment for the finite element and finite volume discretisations.

half load cycle; Case 1: $\bar{M}_{f,FE} = -1.811\,\mathrm{Nm}$ and $\bar{M}_{f,FV} = -1.706\,\mathrm{Nm}$ and Case 2: $\bar{M}_{f,FE} = -2.187\,\mathrm{Nm}$, $\bar{M}_{f,2.1} = -1.713\,\mathrm{Nm}$, $\bar{M}_{f,2.2} = -1.706\,\mathrm{Nm}$, $\bar{M}_{f,2.3} = -1.708\,\mathrm{Nm}$.

Though similarities are to be expected from the orbits and pressure distributions, some conclusions can be drawn. Assuming the full 3D solution represented by the finite volume scheme to be the most correct approximation, the friction loss is overestimated by 6% for Case 1 and 28% for Case 2 by the finite element discretisation. With reference to the above results, the fine grid has resolved the problem sufficiently, such that the difference is more related to the choice of 2D (Reynolds equation) versus 3D (Navier-Stokes equations). Within Case 2 with the varying groove height, there is practically no difference ($< 0.5\%$) of the three heights. Interestingly, the point groove generates virtually the same friction loss.

4.4. Flow fields

Figure 8 illustrates the velocity fields of the two cases in the symmetry plane. Contrary to an ordinary vector plot, the so-called line integral convolution technique is used here. This allows for a simple representation of the velocity field at the expense of flow directions. For this set-up this has not

been found to be an issue, but supporting vector plots have been made.

Analysing Case 1 in Figure 8a it is clearly seen that one major vortex is formed at the top of the groove, just after the inlet pipe. Its clockwise rotation helps the inlet flow mixing with that of the rotational flow attached to the journal. This is also seen from the thin film section where the journal surface velocity driving the system is extending into the groove.

On the other hand, Case 2 in Figure 8b reveals three vortices located at the left, center and right parts of the groove. The extent of the journal velocity into the groove is also less distinct, with areas of very slow moving lubricant.

5. Conclusion

Comparing the two ways of solving the bearing problem and two different boundary conditions yields:

- Very little influence from inlet type on pressure distribution for finite volume discretisation.
- Similar journal orbits for all four combinations, except for the finite element solution with circumferential groove.
- Friction loss prediction being based on journal orbit is showing good agreement, except for finite element solution with circumferential groove.
- Circumferential groove features more vertices in groove area.

Acknowledgements

The work is partly financed through the EU project HERCULES-C, grant agreement no. SCP1-GA-2011-284354.

Appendix A. Non-dimensionalisation

The below relations are used for the non-dimensionalisation of the variables in Equation (3):

$$\theta = \frac{x}{R} \tag{A.1}$$

$$\zeta = \frac{z}{R} \tag{A.2}$$

$$\bar{p} = \frac{p}{6\mu\omega\left(\frac{R}{C}\right)^2} \tag{A.3}$$

$$\bar{h} = \frac{h}{C} \tag{A.4}$$

$$\bar{t} = \frac{t}{1/\omega^*} \tag{A.5}$$

Where x is circumferential coordinate, R is journal radius, z is axial coordinate, p is pressure, μ is dynamic viscosity, ω is angular velocity of journal, C is radial clearance in bearing, h is film thickness, t is time and $\omega^* = \omega$ is a characteristic angular velocity which is chosen as the angular velocity of journal.

References

[1] O. Reynolds, On the Theory of Lubrication and Its Application to Mr. Beauchamp Tower's Experiments, Including an Experimental Determination of the Viscosity of Olive Oil, Philosophical Transactions of the Royal Society of London 177 (1886) 157–234, DOI: 10.1098/rspl.1886.0021.

[2] A. Sommerfeld, Zur hydrodynamischen Theorie der Schmiermittelreibung, Zeit. angew. Math. u. Physik 50 (1904) 97–155.

[3] F. W. Ocvirk, Short-bearing approximation for full journal bearings, Technical note 2808, Cornell University (1952).

[4] H. W. Swift, The stability of lubricating films in journal bearings, in: Proceedings Institute Civil Engineers, Vol. 233, Thomas Telford, 1932, pp. 267–288.

[5] W. Stieber, Das Schwimmlager: Hydrodynamische Theorie des Gleitlagers, VDI-Verlag, GmbH., 1933.

[6] H. Elrod, M. Adams, A computer program for cavitation and starvation problems, Cavitation and related phenomena in lubrication (1974) 37–41.

[7] D. Brewe, Theoretical modeling of the vapor cavitation in dynamically loaded journal bearings, Journal of tribology 108 (4) (1986) 628–637, DOI: 10.1115/1.3261288.

[8] P. Tucker, P. Keogh, A generalized computational fluid dynamics approach for journal bearing performance prediction, Proceedings of the Institution of Mechanical Engineers, Part J: Journal of Engineering Tribology 209 (2) (1995) 99–108, DOI: 10.1243/PIME_PROC_1995_209_412_02.

[9] K. Gertzos, P. Nikolakopoulos, C. Papadopoulos, Cfd analysis of journal bearing hydrodynamic lubrication by bingham lubricant, Tribology International 41 (12) (2008) 1190–1204, DOI: 10.1016/j.triboint.2008.03.002.

[10] M. Schmidt, P. Stücke, M. Nobis, Numerical meshing issues for three-dimensional flow simulations in journal bearings, in: 3rd Micro and Nano Flows Conference, 2011, Thessaloniki, Greece, 22-24 August 2011.

[11] M. Riedel, M. Schmidt, P. Stücke, Numerical investigation of cavitation flow in journal bearing geometry, in: EPJ Web of Conferences 45, 01081 (2013), 2013, DOI: 10.1051/epjconf/20134501081.

[12] M. Riedel, M. Schmidt, P. Reinke, M. Nobis, M. Redlich, Application of computational fluid dynamics on cavitations in journal bearings, in: EPJ Web of Conferences 67, 02099 (2014), 2014, DOI: 10.1051/epjconf/20146702099.

[13] CD-Adapco, User Guide STAR-CCM+ Version 10.02 (2015).

[14] J. W. Lund, K. K. Thomsen, A Calculation Method and Data for the Dynamic Coefficients of Oil-Lubricated Journal Bearings, in: Topics in Fluid Film Bearing and Rotor Bearing System Design and Optimization, ASME publ., 1978, pp. 1–28.

[15] C. Christiansen, P. Klit, J. Walther, A. Vølund, Orbit prediction of a journal bearing - Finite Element modelling and experimental studies, Finnish Journal of Tribology 33 (2015) 28–35.

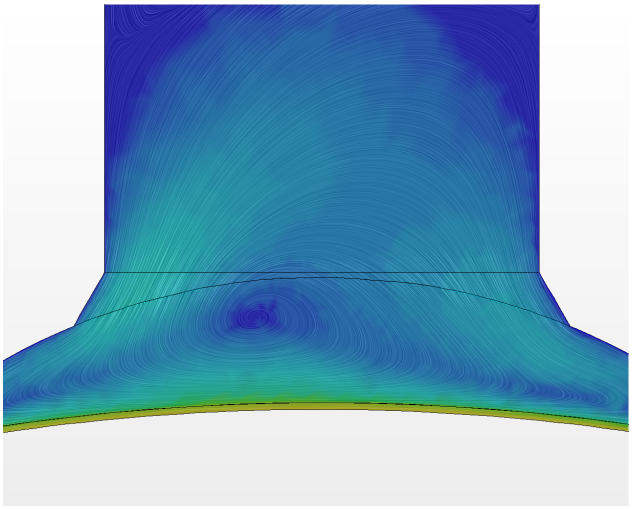

(a)

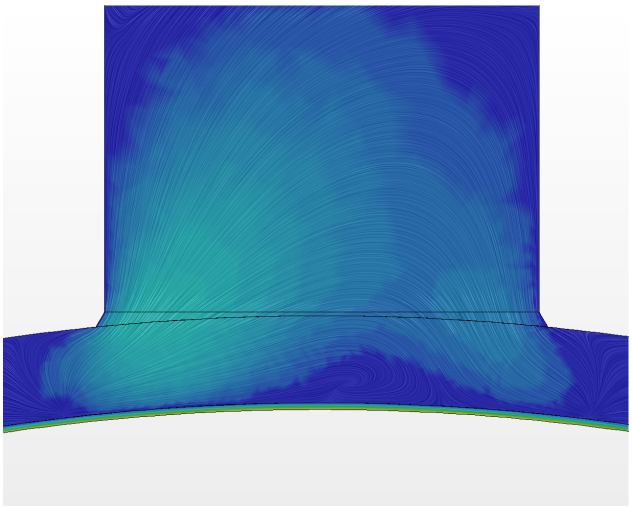

(b)

Figure 8: Velocity field in the symmetry plane at $t = 0.075\,\mathrm{s}$ for the two bearing geometries: (a) Point groove (Case 1). (b) Circumferential groove (Case 2.1). Main journal rotation is CCW. Colour represents velocity magnitude with blue = $0\,\mathrm{m/s}$ and khaki = $3.14\,\mathrm{m/s}$.

References

General references

[1] Peter Dan Petersen, ed. *Diesel Facts*. MAN Diesel & Turbo. 2007. URL: http://www.mandieselturbo.de/files/news/filesof11474/Diesel facts_2007_1.pdf (visited on Aug. 6, 2015) (cit. on p. 2).

[2] *Blended Edge Main Bearings*. MAN Diesel & Turbo. 2014. URL: http://marine.man.eu/docs/librariesprovider6/technical-papers/blended-edge-main-bearings.pdf?sfvrsn=24 (visited on Aug. 6, 2015) (cit. on p. 3).

[3] Jerome Adamstein. *The Week in Pictures. Aug. 6-15, 2010*. Los Angeles Times. 2010. URL: http://framework.latimes.com/2010/08/13/the-week-in-pictures-2/#/63 (visited on Aug. 6, 2015) (cit. on p. 3).

[4] Osborne Reynolds. "On the Theory of Lubrication and Its Application to Mr. Beauchamp Tower's Experiments, Including an Experimental Determination of the Viscosity of Olive Oil". In: *Philosophical Transactions of the Royal Society of London* 177 (1886), pp. 157–234. DOI: 10.1098/rspl.1886.0021 (cit. on pp. 3, 4, 6, 13, 24, 25).

[5] D. Dowson and C. M. Taylor. "Cavitation in bearings". In: *Annual Review of Fluid Mechanics* 11.1 (1979), pp. 35–65. DOI: 10.1146/annurev.fl.11.010179.000343 (cit. on pp. 3, 5).

[6] M. J. Braun and W. M. Hannon. "Cavitation formation and modelling for fluid film bearings: a review". In: *Proceedings of the Institution of Mechanical Engineers, Part J: Journal of Engineering Tribology* 224.9 (2010), pp. 839–863. DOI: 10.1243/13506501JET772 (cit. on pp. 3–5).

[7] Leif Floberg. *On journal bearing lubrication considering the tensile strength of the liquid lubricant*. Lund Technical University, 1973 (cit. on pp. 4, 5).

[8] Herbert Walker Swift. "THE STABILITY OF LUBRICATING FILMS IN JOURNAL BEARINGS". In: *Proceedings Institute Civil Engineers*. Vol. 233. 1932. Thomas Telford. 1932, pp. 267–288 (cit. on p. 4).

[9] Wilhelm Stieber. *Das Schwimmlager: Hydrodynamische Theorie des Gleitlagers*. VDI-Verlag, GmbH., 1933 (cit. on p. 4).

[10] Bengt Jakobsson and Leif Floberg. *The Finite Journal Bearing Considering Vaporization*. Transactions of Chalmers University of Technology 190. Gothenburg, Sweden, 1957 (cit. on pp. 5, 6).

[11] L. Floberg. "Cavitation boundary conditions with regard to the number of streamers and tensile strength of the liquid". In: *Cavitation and related phenomena in lubrication* (1974), pp. 31–36 (cit. on p. 5).

[12] K.-O. Olsson. *Cavitation in Dynamically Loaded Bearings*. Transactions of Chalmers University of Technology. Gothenburg, Sweden, 1965 (cit. on p. 5).

[13] G. Bauer. *Ölhydraulik*. 2nd ed. Teubner, 1978 (cit. on p. 5).

[14] H.G. Elrod and M.L. Adams. "A computer program for cavitation and starvation problems". In: *Cavitation and related phenomena in lubrication* (1974), pp. 37–41 (cit. on p. 6).

[15] P.G. Tucker and P.S. Keogh. "A generalized computational fluid dynamics approach for journal bearing performance prediction". In: *Proceedings of the Institution of Mechanical Engineers, Part J: Journal of Engineering Tribology* 209.2 (1995), pp. 99–108. DOI: 10.1243/PIME_PROC_1995_209_412_02 (cit. on p. 6).

[16] Zenglin Guo, Toshio Hirano, and R. Gordon Kirk. "Application of CFD analysis for rotating machinery–Part I: Hydrodynamic, hydrostatic bearings and squeeze film damper". In: *Journal of Engineering for Gas Turbines and Power* 127.2 (2005), pp. 445–451. DOI: 10.1115/1.1807415 (cit. on p. 6).

[17] M. Riedel, M. Schmidt, and P. Stücke. "Numerical investigation of cavitation flow in journal bearing geometry". In: *EPJ Web of Conferences*. Vol. 45. EDP Sciences. 2013, p. 01081. DOI: 10.1051/epjconf/20134501081 (cit. on p. 6).

[18] G. S. A. Shawki and P. Freeman. "Journal Bearing Performance under Sinusoidally Alternating and Fluctuating Loads". In: *Proceedings of the Institution of Mechanical Engineers* 169.1 (1955), pp. 689–698. DOI: 10.1243/PIME_PROC_1955_169_072_02 (cit. on pp. 6, 61, 66, 91–93, 99).

[19] Theodor E. Carl. "Paper 19: An Experimental Investigation of a Cylindrical Journal Bearing under Constant and Sinusoidal Loading". In: *Proceedings of the Institution of Mechanical Engineers, Conference Proceedings*. Vol. 178. 14. SAGE Publications. 1963, pp. 100–119. DOI: 10.1243/PIME_CONF_1963_178_381_02 (cit. on pp. 6, 61, 66, 91–93, 99, 100).

[20] B. O. Jacobson and B. J. Hamrock. "High-speed motion picture camera experiments of cavitation in dynamically loaded journal bearings". In: *Journal of Lubrication Technology* 105.3 (1983), pp. 446–452. DOI: 10.1115/1.3254639 (cit. on pp. 6, 66).

[21] David Darling. *Bearing*. 2012. URL: http://www.daviddarling.info/encyclopedia/B/bearing.html (visited on Oct. 19, 2012) (cit. on p. 9).

[22] R. Gohar and H. Rahnejat. In: *Fundamentals of Tribology*. 1st ed. Imperial College Press, 2008, pp. 94–99 (cit. on pp. 13, 16).

[23] James David Colin McIvor. "The Analysis of Dynamically Loaded Flexible Journal Bearings Using Higher-Order Finite Elements". PhD thesis. University of London, 1988 (cit. on pp. 13, 14, 51).

[24] Jørgen Lund and Peder Klit. *Hydrodynamic Lubrication*. Lecture notes (draft). 2012 (cit. on p. 13).

[25] Wolfram MathWorld. *Elliptic Partial Differential Equation*. 2012. URL: http://mathworld.wolfram.com/EllipticPartialDifferentialEquation.html (visited on Nov. 6, 2012) (cit. on p. 17).

[26] A. Sommerfeld. "Zur hydrodynamischen Theorie der Schmiermittelreibung". In: *Zeit. angew. Math. u. Physik* 50 (1904), pp. 97–155. DOI: 10.1007/BF01657589 (cit. on pp. 21, 24, 109).

[27] F. W. Ocvirk. *Short-Bearing Approximation for Full Journal Bearings*. Technical note 2808. Cornell University, 1952 (cit. on pp. 21, 28, 29).

[28] J. W. Lund. *Notater til forelæsninger i smøringsmekanik*. Lecture notes. approx. 1970 (cit. on pp. 21, 22, 24, 36).

[29] Bernard J. Hamrock, Steven R. Schmid, and Bo O. Jacobson. *Fundamentals of Fluid Film Lubrication*. 2nd ed. Marcel Dekker, Inc., 2004 (cit. on pp. 25, 68).

[30] J. W. Lund and K. K. Thomsen. "A Calculation Method and Data for the Dynamic Coefficients of Oil-Lubricated Journal Bearings". In: *Topics in Fluid Film Bearing and Rotor Bearing System Design and Optimization*. ASME publ., 1978 (cit. on pp. 33, 36).

[31] Zissimos P. Mourelatos. "An efficient journal bearing lubrication analysis for engine crankshafts". In: *Tribology Transactions* 44.3 (2001), pp. 351–358. DOI: 10.1080/10402000108982467 (cit. on p. 39).

[32] A. Kumar and J. F. Booker. "A finite element cavitation algorithm". In: *Journal of Tribology* 113.2 (1991), pp. 276–284. DOI: 10.1115/1.2920617 (cit. on p. 39).

[33] Robert D. Cook, David S. Malkus, Michael E. Plesha, and Robert J. Witt. *Concepts and Applications of Finite Element Analysis*. 4th ed. John Wiley & Sons, Inc., 2002 (cit. on pp. 40, 42, 48).

[34] Carlos A. Felippa. *Introduction to Finite Element Methods*. Lecture notes from course 'Introduction to Finite Elements Methods' (ASEN 5007). University of Colorado - Department of Aerospace Engineering Sciences and Center for Aerospace Structures. 2004. URL: http://www.colorado.edu/engineering/CAS/courses.d/IFEM.d/ (visited on July 29, 2015) (cit. on p. 44).

[35] A. P. Engsig-Karup. *The Spectral/hp-Finite Element Method for Partial Differential Equations*. 1st ed. Scientific Computing Section, DTU Informatics, Technical University of Denmark, 2012 (cit. on p. 44).

[36] P. Klit and J. W. Lund. "Calculation of the dynamic coefficients of a journal bearing, using a variational approach". In: *Journal of Tribology* 108.3 (1986), pp. 421–424. DOI: 10.1115/1.3261223 (cit. on p. 47).

[37] J. Campbell, P. P. Love, F. A. Martin, and S. O. Rafique. "Paper 4: Bearings for Reciprocating Machinery: A Review of the Present State of Theoretical, Experimental and Service Knowledge". In: *Proceedings of the Institution of Mechanical Engineers, Conference Proceedings*. Vol. 182. 1. SAGE Publications. 1967, pp. 51–74. DOI: 10.1243/PIME_CONF_1967_182_008_02 (cit. on pp. 47, 53, 54).

[38] Wolfram MathWorld. *Euler-Lagrange Differential Equation*. URL: http://mathworld.wolfram.com/Euler-LagrangeDifferentialEquation.html (visited on May 23, 2014) (cit. on pp. 47, 117).

[39] *STAR-CCM+ User Guide*. Version 10.02. CD-adapco, 2015 (cit. on p. 57).

[40] Marcus Schmidt, Peter Stücke, and Matthias Nobis. "Numerical meshing issues for three-dimensional flow simulation in journal bearings". In: *3rd Micro and Nano Flows Conference*. (Thessaloniki, Greece, Aug. 22–24, 2011). Brunel University, 2011. ISBN: 978-1-902316-98-7 (cit. on p. 59).

[41] Peder Klit and Niels L. Pedersen. *Machine Elements. Analysis and Design*. 2nd ed. Polyteknisk Forlag, 2014 (cit. on p. 64).

[42] William D. Callister Jr. *Materials Science and Engineering. An Introduction*. 7th ed. John Wiley & Sons, Inc., 2007. ISBN: 0-471-73696-1 (cit. on pp. 65, 89).

[43] F. A. Martin. "Developments in engine bearing design". In: *Tribology International* 16.3 (1983), pp. 147–164. DOI: 10.1016/0301-679X(83)90058-0 (cit. on p. 85).

[44] G. Hardy. *The Integration of Functions of a Single Variable*. Cambridge Tracts in Mathematics and Mathematical Physics 2. Cambridge University Press, 1905 (cit. on p. 109).

[45] J. F. Booker. "A Table of the Journal-Bearing Integral". In: *Journal of Basic Engineering* 87 (1965). Issue 3, pp. 533–535. DOI: 10.1115/1.3650600 (cit. on p. 109).

[46] In: *Fluid Film Lubrication - Osborne Reynolds Centenary*. Ed. by D. Dowson, C. M. Taylor, M. Godet, and D. Berthe. Vol. 11. Tribology Series. Elsevier, 1987, pp. 666–667 (cit. on p. 109).

Papers forming part of the thesis

[P1] Christian K. Christiansen, Peder Klit, Jens H. Walther, and Anders Vølund. "Application of finite elements and computational fluid dynamics to predict and improve the filling ratio in journal bearings under dynamic loading". In: *Proceedings of NSCM-27: the 27th Nordic Seminar on Computational Mechanics*. (Stockholm). Ed. by A. Eriksson, A. Kulachenko, M. Mihaescu, and G. Tibert. TRITA-MEK Technical report. ISSN: 0348-467X. 2014, pp. 50–53 (cit. on pp. i, iii, 7, 56, 105).

[P2] C. K. Christiansen, P. Klit, J. H. Walther, and A. Vølund. "Cavitation Estimates by Orbit Prediction of a Journal Bearing - Finite Element Modelling and Experimental Studies". In: *TRIBOLOGIA - Finnish Journal of Tribology 1* 33.1 (2015), pp. 28–35. ISSN: 0780-2285 (cit. on pp. ii, iii, 7, 47, 53, 54, 85, 105).

[P3] Christian Kim Christiansen, Jens Honore Walther, Peder Klit, and Anders Vølund. "Investigation of journal orbit and flow pattern in a dynamically loaded journal bearing". Intended for publishing in Tribology International. Mar. 2016. Draft (cit. on pp. ii, iv, 7, 55, 73, 105).

DTU Mechanical Engineering
Section of Solid Mechanics
Technical University of Denmark

Nils Koppels Allé, Bld. 404
DK-2800 Kgs. Lyngby
Denmark
Phone (+45) 4525 4250
Fax (+45) 4593 1475
www.mek.dtu.dk
ISBN: 978-87-7475-439-8

DCAMM
Danish Center for Applied Mathematics and Mechanics

Nils Koppels Allé, Bld. 404
DK-2800 Kgs. Lyngby
Denmark
Phone (+45) 4525 4250
Fax (+45) 4593 1475
www.dcamm.dk
ISSN: 0903-1685